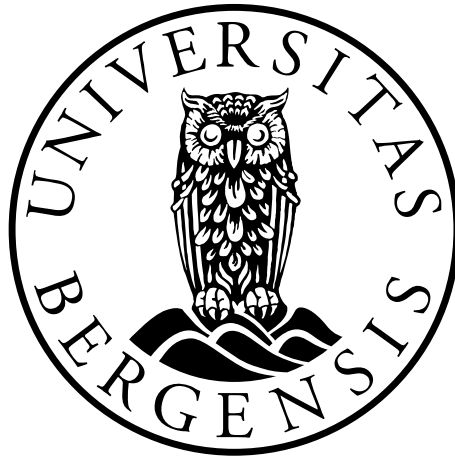


*In vitro* and *in vivo* studies of a novel blood  
brain barrier permeabilizing peptide

**K16ApoE**

And novel *in vivo* treatment of melanoma brain metastases

**Christopher Florian Holte**



This thesis is submitted in partial fulfilment of the requirements for the degree of Master in  
Medical Biology – Biomedical Image Sciences

Department of Biomedicine

University of Bergen

2016

# Table of Contents

Acknowledgements.....	4
Abbreviations.....	5
Table of figures.....	7
Abstract.....	9
1 Introduction.....	12
1.1 Skin cancer and melanoma.....	12
1.2 Incidence and causes of melanoma.....	13
1.3 Mutations in melanoma development.....	15
1.4 Grading and staging of melanoma.....	15
1.5 Treatment of melanoma.....	17
1.6 The metastatic process.....	18
1.7 Treatment of brain metastases.....	21
1.8 The Blood Brain Barrier.....	22
1.9 Permeabilizing the BBB.....	23
1.10 K16ApoE.....	25
1.11 Models to Study Melanoma Progression.....	26
1.11.1 <i>In Vitro</i> Models.....	26
1.11.2 <i>In Vivo</i> Models (Xenografts).....	26
<i>In Vivo</i> Cancer Metastasis Models.....	26
Animal brain metastasis models.....	27
1.12 Imaging.....	27
1.12.1 Fluorescent microscopy & time-lapse microscopy.....	27
1.12.2 Electron Microscopy.....	29
Scanning Electron Microscopy (SEM).....	29
Transmission Electron Microscopy (TEM).....	30
1.12.3 Magnetic Resonance Imaging (MRI).....	30
The NMR signal.....	30
Magnetic Resonance Imaging (MRI).....	32
Contrast enhancement and DCE-MRI.....	34
1.12.4 Bioluminescence Imaging (BLI).....	36
2 Aims of this Study.....	37
3 Materials and Methods.....	38
3.1 <i>In Vitro</i> .....	38
Cell lines used:.....	38
Medium and solutions:.....	39
3.1.1 General Cell Culture Work.....	40

3.1.2 Resazurin-resorfin Cell Viability Assay .....	43
3.1.3 Morphological light microscopy .....	43
3.1.4 Time-lapse fluorescence microscopy .....	44
3.1.5 Electron Microscopy .....	44
Scanning Electron Microscopy (SEM).....	45
Transmission Electron Microscopy (TEM).....	45
3.2 In Vivo.....	46
Mice and Housing Conditions .....	46
3.2.1 K16ApoE kinetics studies, DCE-MRI .....	47
3.2.2 Mouse Xenograft Model .....	48
3.2.3 Pilot Treatment Experiment.....	49
3.2.3.1 BLI.....	49
3.2.3.2 MRI (T1, T2, T1-contrast – anatomical sans).....	50
3.2.3.3 Endpoints .....	50
3.2.3.4 Histology .....	50
3.3 Software.....	51
4 Results.....	52
4.1 <i>In vitro</i> .....	52
4.1.1 Vemurafenib cell culture experiments.....	52
4.1.1.1 Cell Viability assay .....	52
4.1.1.2 Light microscopy .....	53
4.1.2 K16ApoE cell culture experiments.....	53
4.1.2.1 Survival assay .....	53
4.1.2.2 Time-lapse Fluorescence Microscopy .....	55
4.1.2.3 Electron Microscopy.....	58
Scanning Electron Microscopy .....	58
Transmission Electron Microscopy .....	60
4.2 <i>In Vivo</i> .....	61
4.2.1 K16ApoE Kinetics: DCE-MRI .....	61
4.2.1.1 K16ApoE effect on BBB 10 minutes post administration .....	61
4.2.1.2 Evaluation of duration of BBB opening after injection of K16ApoE.....	62
4.2.1.3 Half-dose (100 µg K16ApoE) experiments .....	64
4.2.1.4 Intra peritoneal administration of K16ApoE .....	66
4.2.2 Pilot Study: Combinatorial Treatment of xenografted melanoma with vemurafenib and K16ApoE.....	66
4.2.2.1 Animal weight over time .....	66
4.2.2.2 BLI.....	67
4.2.2.3 Anatomical MRI .....	69

4.2.2.4 Histology .....	71
5 Discussion.....	73
References .....	81

## Acknowledgements

First and foremost I would like to thank my supervisor professor Frits Thorsen, for help and support given throughout the entirety of my project. I would also like to give my recommendation to future prospective master and project students, to have professor Thorsen as their mentor.

I would like to thank Synnøve Aasen, for help during MRI, amongst other things.

I would also like to confer my gratitude to the personnel at the Molecular Imaging Centre, Anne Nyhaug, Endy Spriet, Hege Dale, Heidi Espedal, and Tina Pavlin all of whom were of tremendous help to me on many occasions.

I would further like to thank for their contributions and help; Kai Brandt, Lars Prestegarden, Halala Saed, Olivier Keunen, Tove Johansen, Anne Døskeland, Habib Baghirov and professor Reidar Myklebust.

A further note of gratitude goes to my friends and family for their patience, confidence and support over the last two years.

Christopher Florian Holte

## Abbreviations

<b>AMP</b>	Adenosine monophosphate
<b>ApoE</b>	ApolipoproteinE
<b>ATP</b>	Adenosine triphosphate
<b>B<sub>0</sub></b>	Field strength
<b>BBB</b>	Blood brain barrier
<b>BCC</b>	Basal cell carcinoma
<b>BLI</b>	Bioluminescence imaging
<b>C<sub>e</sub></b>	Concentration of contrast agent in EES
<b>CO<sub>2</sub></b>	Carbon dioxide
<b>CTL / CTLA</b>	Cytotoxic T-lymphocyte / cytotoxic T-lymphocyte associated antigen
<b>DCE-MRI</b>	Dynamic contrast enhanced MRI
<b>DMEM</b>	Dulbecco's modified Eagles medium
<b>DMSO</b>	Dimethyl sulphoxide
<b>DNA</b>	Deoxyribonucleic acid
<b>EB</b>	Evans blue dye
<b>ECM</b>	Extracellular matrix
<b>EDTA</b>	Ethylenediaminetetraacetic acid
<b>EES</b>	Extracellular extravascular space
<b>EMT</b>	Epithelial to mesenchymal transition
<b>FA</b>	Flip angle
<b>FBS</b>	Fetal bovine serum
<b>FOV</b>	Field of view
<b>GFP</b>	Green fluorescent protein
<b>IC<sub>50</sub></b>	Half-maximal inhibitory concentration
<b>K<sub>1,2</sub></b>	Transfer coefficient from V <sub>p</sub> to EES
<b>K<sub>2,1</sub></b>	Transfer coefficient from EES to V <sub>p</sub>
<b>LDL / LDLR</b>	Low density lipoprotein / low density lipoprotein receptor
<b>Melanoma</b>	Malignant melanoma
<b>MRI</b>	Magnetic resonance imaging
<b>M<sub>xy</sub></b>	Transverse magnetization
<b>M<sub>z</sub></b>	Longitudinal magnetization
<b>ms</b>	Millisecond

<b>NaCl</b>	Sodium chloride
<b>NEX</b>	Number of excitations
<b>NOD/SCID</b>	Non-obese diabetic/severe combined immune deficient mice
<b>NMR</b>	Nuclear magnetic resonance
<b>n.s.</b>	Not significant
<b>O<sub>2</sub></b>	Oxygen
<b>PBS</b>	Dulbecco's phosphate buffered saline
<b>r<sub>1</sub> / r<sub>2</sub></b>	Longitudinal / transverse relaxation
<b>RF</b>	Radio frequency
<b>ROI</b>	Region of interest
<b>RPM</b>	Rotations per minute
<b>SD</b>	Standard deviation
<b>SRS</b>	Stereotactic radiosurgery
<b>T</b>	Tesla
<b>T<sub>1</sub></b>	Time constant of 63 % recovery of longitudinal magnetization
<b>T<sub>2</sub></b>	Time constant of transverse magnetization decay to 37 %
<b>TE</b>	Echo time
<b>TNF / TNFR</b>	Tumor necrosis factor / Tumor necrosis factor receptor
<b>TR</b>	Repetition time
<b>UV</b>	Ultra violet
<b>V600E</b>	Valine to glutamine substitution at position 600
<b>V600K</b>	Valine to lysine substitution at position 600
<b>Vem.</b>	Vemurafenib
<b>V<sub>p</sub></b>	Vascular plasma space
<b>WBRT</b>	Whole brain radiotherapy

## Table of figures

<b>Figure 1.1</b>	Schematic illustration of the skin
<b>Figure 1.2</b>	Age distribution of melanoma cases in the United States
<b>Figure 1.3</b>	Worldwide incidence rates of melanoma of the skin
<b>Figure 1.4</b>	The 5-year survival of melanoma patients by staging
<b>Figure 1.5</b>	The epithelial to mesenchymal transition
<b>Figure 1.6</b>	The brain metastatic process
<b>Figure 1.7</b>	Primary sites of brain metastatic cancers by prevalence
<b>Figure 1.8</b>	A schematic overview of the blood brain barrier
<b>Figure 1.9</b>	Opening the BBB through application of focused and directed ultrasound
<b>Figure 1.10</b>	Hypertonic osmotic BBB permeabilization
<b>Figure 1.11</b>	Opening of the BBB after intravenous treatment with K16ApoE
<b>Figure 1.12</b>	The physical process of fluorescence
<b>Figure 1.13</b>	The two modes of electron microscopy
<b>Figure 1.14</b>	The proton spin analogized as a bar magnet and the orientation of proton spins within a magnetic field
<b>Figure 1.15</b>	A free induction decay signal
<b>Figure 1.16</b>	Illustration showing principles of the slice selecting gradient, phase encoding gradient and frequency encoding gradient
<b>Figure 1.17</b>	Tofts two compartment model
<b>Figure 1.18</b>	A typical setup of an optical imager used in bioluminescence imaging
<b>Figure 3.1</b>	pGreenFire HIV based lentiviral vector
<b>Figure 3.2</b>	The electron microscopes used in this study
<b>Figure 3.3</b>	The Bruker Pharmascan® 7T small animal MRI used in this study
<b>Figure 3.4</b>	Tail vein injection setup and anesthesia vaporizer
<b>Figure 3.5</b>	Timeline of pilot treatment study
<b>Figure 4.1</b>	Cell viability assay. Resazurin cell survival assay of H1_DL2 melanoma cell line cells treated with varying concentrations of vemurafenib
<b>Figure 4.2</b>	Cell viability assay. Resazurin cell survival assay of SV80 human fibroblast cells treated with varying concentrations of vemurafenib
<b>Figure 4.3</b>	Cell morphology of H1_DL2 cells treated with 50 $\mu$ M vemurafenib
<b>Figure 4.4</b>	Relative survival of MDCKII cells treated with varying concentrations of K16ApoE
<b>Figure 4.5</b>	Relative survival of RBE4 cells treated with varying concentrations of K16ApoE
<b>Figure 4.6</b>	Relative survival of H1_DL2 cells treated with varying concentrations of K16ApoE

<b>Figure 4.7</b>	Frames from time-lapse fluorescence microscopy of MDCKII cells transduced with mcherry and treated with varying concentrations of K16ApoE
<b>Figure 4.8</b>	Binary images created from fluorescence images of MDCKII-mcherry cells treated with varying concentrations of K16ApoE
<b>Figure 4.9</b>	Time-lapse microscopy curves of mcherry intensities MDCKII cells treated with varying concentrations of K16ApoE
<b>Figure 4.10</b>	Scanning electron microscopy images of MDCKII cell line monolayer cells treated with varying concentrations of K16ApoE
<b>Figure 4.11</b>	Number of aberrant and dying cells counted on SEM images of MDCKII cells treated with 0, 20, 40, or 80 $\mu\text{g}/\text{mL}$ K16ApoE
<b>Figure 4.12</b>	Transmission electron microscopy images of MDCKII cells treated with 0 and 80 $\mu\text{g}/\text{mL}$ K16ApoE
<b>Figure 4.13</b>	DCE-MRI 200 $\mu\text{g}$ 10 minutes
<b>Figure 4.14</b>	DCE-MRI 200 $\mu\text{g}$ 10 minutes – 4 hours
<b>Figure 4.15</b>	Area under curve values for animals injected with 200 $\mu\text{g}$ K16ApoE at varying time points post injection
<b>Figure 4.16</b>	$K_{1,2}$ values for animals injected with 200 $\mu\text{g}$ K16ApoE at varying time points post injection
<b>Figure 4.17</b>	DCE-MRI 100 $\mu\text{g}$ 10 minutes
<b>Figure 4.18</b>	Area under curve values for 200 $\mu\text{g}$ , 100 $\mu\text{g}$ K16ApoE and control.
<b>Figure 4.19</b>	$K_{1,2}$ values for 200 $\mu\text{g}$ , 100 $\mu\text{g}$ K16ApoE and control.
<b>Figure 4.20</b>	Weight of mice in pilot treatment study compared to days post intracardial injection of tumor cells
<b>Figure 4.21</b>	BLI images of two mice from pilot study
<b>Figure 4.22</b>	Integrated ROI intensities from BLI
<b>Figure 4.23</b>	Anatomical MRI images taken at week five post injection of tumor cells
<b>Figure 4.24</b>	Tumor count and volumes
<b>Figure 4.25</b>	Tumors identified in histological slides
<b>Figure 4.26</b>	Histological sections of the brains of mice from pilot study

## Abstract

Brain metastasis is a common and severe complication arising in up to 40 % of cancer patients. The prognoses for patients with brain metastases are dismal, with a median treated survival of around 10 months. Treatment of brain metastases is mostly limited to surgery and radiotherapy, as an intact blood brain barrier (BBB) effectively protects smaller tumors from chemotherapeutic agents. This means that even if there would be effective chemotherapy treatment regimens for metastases elsewhere in the body, brain metastases would not be affected by such strategies until late stages of cancer development, when the BBB is disrupted.

The prevalence of metastatic melanoma has been increasing steadily the last years accounting for 10 % of all brain metastatic cancers. Advanced stage melanoma patients are commonly treated with targeted inhibitors, such as vemurafenib (a small molecule inhibitor, tailored to have a higher affinity to the mutated BRAF kinase). However an intact BBB then prevents the brain metastases from being affected by vemurafenib as well as most chemotherapeutic agents.

Based on this a novel BBB permeabilizing peptide was of great interest for the work done in this thesis. The peptide is a combination of the low density lipoprotein receptor binding domain of ApolipoproteinE, and a 16 Lysine tail, which was named K16ApoE.

In this study the *in vitro* mechanisms of K16ApoE was studied. Thereafter the ability of opening the BBB by the peptide was investigated, followed by a pilot study combining vemurafenib and K16ApoE in a small animal tumor model.

Cell lines exposed to K16ApoE showed a high degree of cytotoxicity at prolonged exposures of high doses, by affecting cell viability and causing lytic cell death. However lower doses were in general tolerated by the cells. Scanning electron microscopy showed that the peptide caused damages to confluent endothelial cell monolayers likely by inducing lytic cell death. In contrast transmission electron microscopy showed the peptide did not affect cell-cell junctions.

DCE-MRI on mice after intravenous administration of 200 µg of K16ApoE showed that the BBB was opened at already 10 minutes after injection, and was permeable at least 2 hours after injection. In animals given 100 µg of peptide the BBB was also permeabilized 10 minutes after injection of the peptide.

The pilot treatment study using the xenograft mouse model for brain-metastatic melanoma, indicated a treatment effect when co-administering the peptide and a chemotherapeutic agent.

The promising results of this study indicate the potential value of K16ApoE as a therapeutic strategy in brain metastatic cancers. Following this study full scale pre-clinical studies will follow, and based upon those the peptide may move forward towards clinical safety studies, and clinical studies in turn.



# 1 Introduction

## 1.1 Skin cancer and melanoma

The three types of skin cancers are squamous cell carcinomas (SCC) derived from the squamous cells of the epidermis, basal cell carcinomas (BCC) derived from the basal cell layer of the epidermis and malignant melanomas (hereafter called melanoma) derived from the melanocytes of the epidermis (Figure 1.1) [1].

Melanomas are caused by uncontrolled proliferation of melanocytes (Figure 1.1), the pigment producing cells of the skin. Melanomas tend to be heavily pigmented, but may also come in amelanotic (unpigmented) versions [2].

Melanomas most commonly arise in the skin (epidermis), but may also arise in oral or anogenital mucosal surfaces as well as the eyes, and anywhere melanocytes are found [3].

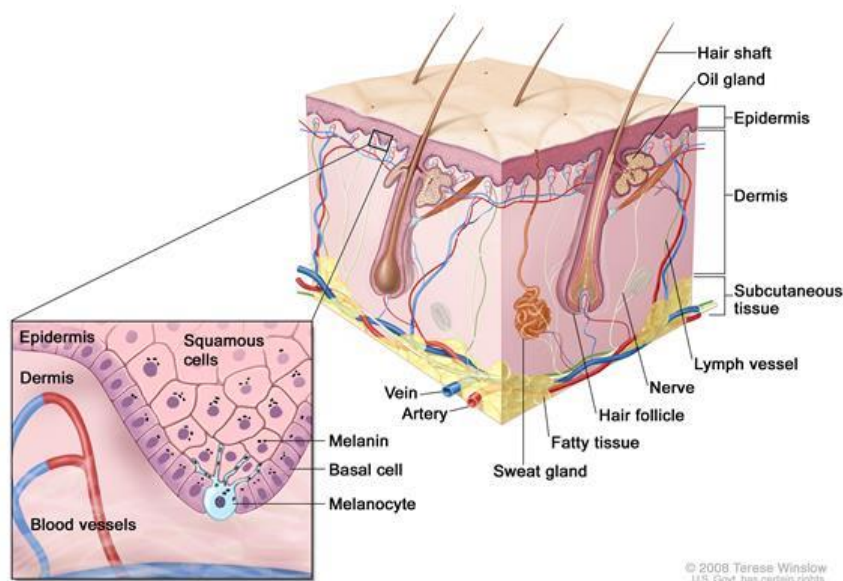


**Figure 1.1:** Schematic illustration of the skin, showing the position of melanocytes, where they are most commonly found, at the bottom of the epidermal layer of the skin. Figure by Terese Winslow from the National Cancer Institute (cancer.gov) [4].

Although they constitute no more than 5 % of skin-derived cancers (US-statistics), cutaneous melanomas are by a wide margin the most lethal skin -cancers, making up 90 % of all skin cancer derived deaths [2, 5].

The classical 4 main subtypes of melanomas are based on clinical and histopathological findings.

*Superficially spreading melanomas* are characterized by radial growth, *Nodular melanomas* are primarily nodular with aggressive vertical growth, and short or absent horizontal growth. *Lentigo maligna melanoma* is characterized by lentiginous (pigment spot) proliferation, most often seen in sun-damaged areas in elder individuals. *Acral lentiginous melanomas* are typically found in the palms of hands, foot-soles or under nails, and commonly display poorly circumscribed pigmentation pattern.

Additional rarer subtypes include *desmoplastic* characterized by vertical scar-tissue like growth [6], *amelanotic* characterized by unpigmented melanocytic lesions and *polypoid melanoma* an outward growing variation of the nodular subtype [7]. Combined these constitute less than 5 % of all melanomas [2].

Melanomas show a high degree of heritability with 5-10 % of melanomas occurring within predisposed families [2].

### 1.2 Incidence and causes of melanoma

The incidence of melanoma is correlated with increasing age, (Figure 1.2), which is believed to be due to accumulated mutations from a longer lifespan [8].

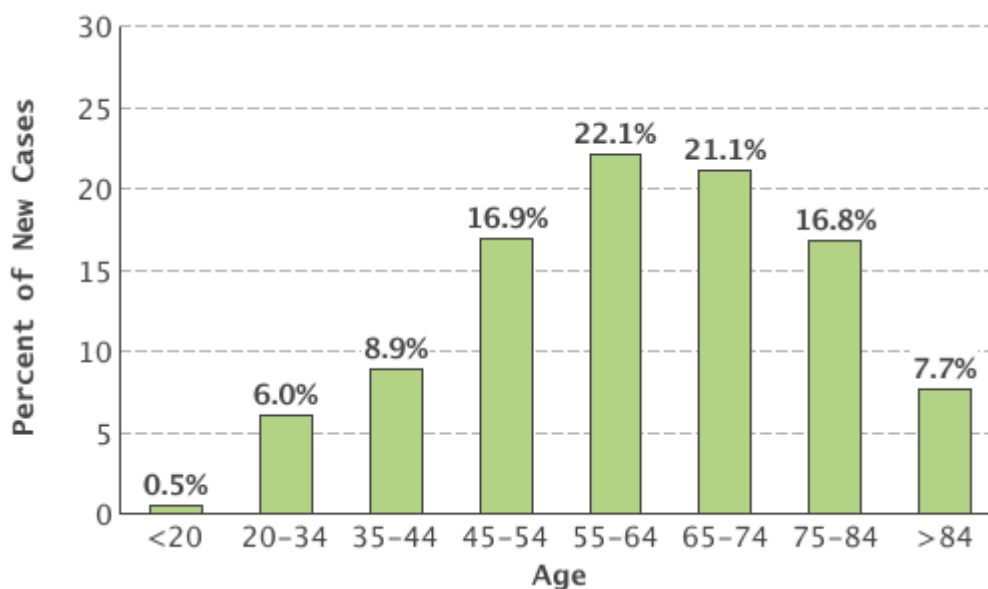


**Figure 1.2:** Age distribution of new melanoma cases in the United States. The median age at diagnosis of melanoma in the U.S. was found to be 63 years [8]. Figure adapted from National Cancer Institute: SEER Cancer Fact Sheets (cancer.gov).

The incidence rates of melanomas are highest in nations with traditionally paler complexions, (Figure 1.3). Countries with predominantly Caucasian populations show high incidence rates

[9]. A correlation with exposure to sun-light has led to UV-radiation being widely accepted as one of the major causes of skin-cancers world-wide [2].

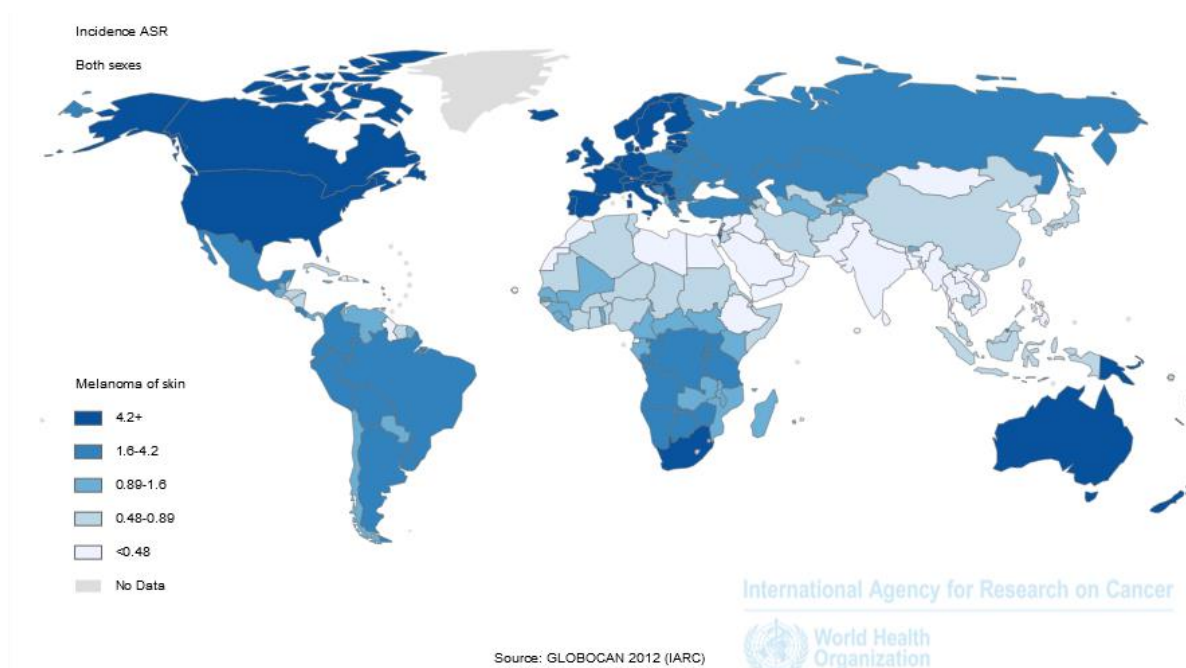


**Figure 1.3:** Worldwide incidence rates of melanoma of the skin, by country. Australia, USA, Canada, Western Europe (including Norway), and South Africa being at the top of melanoma prevalence [10]. Figure adapted from World Health Organization; GLOBOCAN2012.

Epidemiological surveys have also shown that the rate of melanoma incidences has risen over the course of the past years [2, 8, 11]. This is commonly attributed to an increased prevalence of sun-tanning (increased UV-light exposure), as well as an increase in more specific classification of tumors by site of origin (not reflecting an actual increase) and increased lifespans which in turn correspond to an observed increase in overall cancer-incidence.

In the United States, where it is the 5<sup>th</sup> most common cancer [12], the incidence of melanoma increased significantly in the years 1975-2012, though with hardly any increase in mortality (7.9 and 2.1 per 100 000 in 1975, compared to 22.9 and 2.7 per 100 000 in 2012) [8].

Norway has one of the highest occurrences of malignant melanomas in the world, and the incidence rate is currently rising, with approximately 1500 new cases being diagnosed per year (approximate incidence rate 30 per 100 000). There has been noted a steady annual

increase of the rate since first measured in 1953 (one year after the national cancer registry's establishment (1952)) which was 1.9 per 100 000 for men and 2.2 per 100 000 for women [11].

### 1.3 Mutations in melanoma development

Cancer cells escape apoptosis and proliferate through the effects of acquired mutations, with regulatory pathways in some way altered. Desensitization to death-signals and apoptosis pathways, constitutive activation of growth signal pathways enables this aberrant behavior.

There are several mutations that are known to be integral to melanoma progression, with certain mutations occurring in most melanomas. Mutations in BRAF, NRAS, PTEN, TP53, p16INK4A, MAPK1, PPP6C, RAC1, SNX31, TACC1, STK19 have been statistically linked to melanoma development through cancer cell genome analysis, exemplifying the heterogeneity of melanoma mutations. There are however certain mutations with significantly elevated frequencies in melanomas, such as mutations in the BRAF-kinase [13]. The BRAF-kinase is a member of the Raf-kinase family, a growth signal transducing kinase of the MAPK/ERK pathway. Approximately 42 % of melanomas harbor an activating mutation in the BRAF-kinase, making it the most frequently mutated gene in in this form of cancer[14]. The most common such mutation is the substitution of Valine to Glutamic acid at position 600 (V600E), accounting for between 70 & 90 % of activating mutations in BRAF. The second most common mutation is the V600K substitution. Both of these mutations render the kinase constitutively active, leading to increased growth and proliferation [14, 15]. This has led to the targeting of mutated BRAF in novel a treatment regimen, using a mutation specific inhibitor vemurafenib, designed to have higher affinity towards BRAF with a (V600) mutation, acting on both (V600E) and (V600K) mutations [16].

### 1.4 Grading and staging of melanoma

Grading and staging of cancer are the classifications of neoplasms according to their probable clinical aggressiveness, extent and spread, used for making prognosis and assigning treatments. Grading of cancers seek to estimate their aggressiveness and their malignancy, based on cytology of cells within a tumor, and is determined by studying the cytological appearance of the tumor cells [3]. Staging of cancers is based upon exploring the primary size of the lesions, the potential spread to regional lymph nodes and the presence or absence of

metastases. Staging is determined by imaging or exploratory surgery [3]. Different staging systems are used for different cancers, to specifically suit the characteristic behaviors of the different types of cancers.

There are two main methods of staging melanomas in use; the TNM-method (T, primary tumor, N; regional lymph node involvement, M; presence of metastases) and the AJC method (Stages 0-IV, by size of primary lesion, regional lymph node involvement, and presence of metastases). Both staging methods are essentially the same, the differences lie in notation convention only.

Staging of melanoma consists of melanoma-specific versions of the TNM and AJC staging systems which are general cancer staging systems [17].

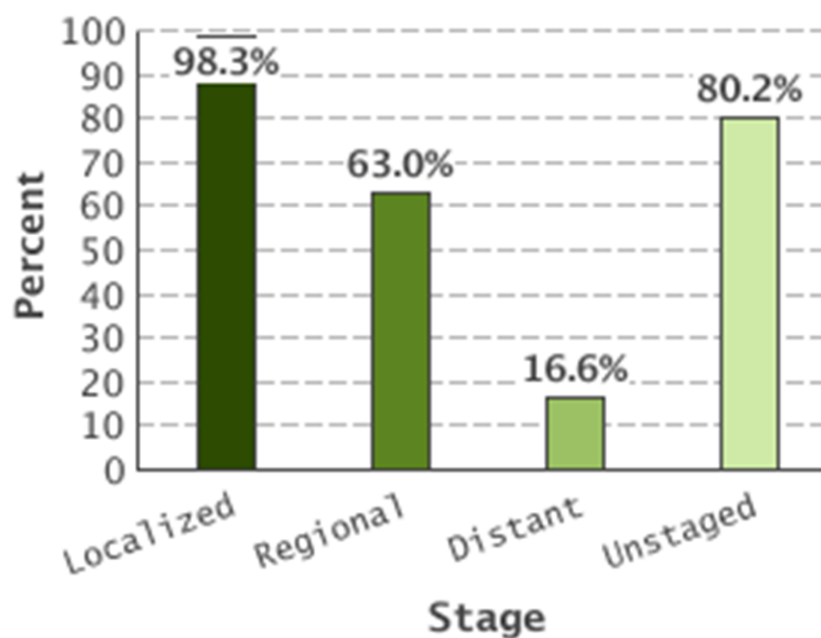


**Figure 1.4:** The 5-year survival of melanoma patients by staging. “Localized” are tumors confined to the site of origin, “Regional” are melanomas that have spread to regional lymph nodes, but not further, and “Distant” are metastatic melanomas (spread beyond the lymph nodes). “Unstaged” are melanomas of unknown staging, i.e. were not staged [8]. Figure adapted from National Cancer Institute: SEER Cancer Fact Sheets (cancer.gov).

Survival from melanoma drastically decreases with metastasis. The initial 5 year survival of melanoma, discovered in its earliest stages, (localized tumors) is high, over 90 %, but drops off significantly with regional spread, to approximately 60 % (regional lymph node involvement) and becomes very poor, less than 20 %, with distal spread (metastasis; distant metastasis, i.e. metastasis to organ other than primary site) (Figure 1.4) [8].

### 1.5 Treatment of melanoma

The general treatment of melanomas is surgery with excision of the primary lesion and surrounding healthy tissues in a margin of conventionally 2 centimeters [2].

Primary surgical treatment is known to be effective in 80-90 % of cases, when discovered in its early stages, i.e. prior to metastasizing, with only 10-20 % experiencing remission following surgery.

Systemic chemotherapy has been the standard form of treatment for distal metastatic melanomas with limited success [11], with it commonly being considered chemotherapy-resistant. General or systemic chemotherapies are the use of various cytotoxic chemicals for cancer therapeutic purposes. Largely these are substances that affect cells during cell-division, as cancer cells are characterized by abnormal proliferation, causing cell death through interfering with processes such as DNA-synthesis and repair or cytoskeletal rearrangement during mitosis [18]. However novel targeted therapies introduced in recent years have shown greater effect than systemic chemotherapy, by extending life expectancies measurably [11].

Radiotherapy has been used in the treatment of metastatic melanoma with limited success, in skin and lymph node metastases, demonstrating that melanomas are responsive only to high doses of radiation [19]. Whilst melanomas are less sensitive to ionizing radiation than other cutaneous tumors, radiotherapy has been used to curative effect on skin lesions [20].

The use of target treatments such as the V600E mutated BRAF-kinase specific inhibitor vemurafenib (also known as zelnorm, or PLX4032) has proven to be effective [21], also against V600K mutated BRAF melanoma [14]. This kinase inhibitor was specifically tailored to have an increased affinity toward the V600E mutated form of the BRAF-kinase, and has been shown to induce growth arrest and apoptosis in melanoma cell cultures [22]. However resistance to the drug is known to develop after prolonged treatment, with 20 % of tumors in xenografted mice developing resistance after 56 days in one model. Intermittent treatment regimens have been proposed as a way to circumvent resistance development [14, 21, 23].

Recently developed treatments using monoclonal antibodies including Nivolumab, Pembrolizumab and Ipilimumab, have been approved for clinical use treating metastatic melanoma.

Nivolumab acts through blocking ligand activation of the PD1 cell surface death-receptor on activated T-cells, a receptor which when activated is known to inhibit T-cell activity [24].

Pembrolizumab also acts upon the PD1 death receptor in much the same way as Nivolumab [25].

Ipilimumab acts through immune response potentiation. This is achieved by blocking the immune-inhibitory- Cytotoxic T-lymphocyte associated Antigen 4 (CTLA-4), which is often up-regulated in cancer cells; allowing them to escape immune system mediated responses, enabling cytotoxic T-lymphocytes (CTLs) to act upon the cancer cells [26].

### 1.6 The metastatic process

Metastases may be defined as secondary occurrences of tumor cells, distant from the primary neoplasm. The presence of metastases characterizes more than anything else a neoplasm as being malignant. The dissemination of malignant tumor cells happens by one (or more) of three routes; seeding of a cavity: when neoplasms invade a natural body cavity such as the ovaries, lymphatic spread or hematogenous spread [3]. Vascular spread gives metastases in more distal organs, hematogenous spread being thought the only way for brain metastases to occur [27].

The steps of the metastatic process are migration, intravasation (entering vessels), transport, extravasation (leaving vessels) and metastatic colonization. The first and last of these steps are considered the rate limiting steps in the metastatic process. In order to migrate cells must break free from cell-cell adhesion (mediated by cadherin and integrins). The tumor cells penetrate the extracellular matrix (ECM) and stroma, by releasing various proteases (serine proteases and matrix metalloproteases predominantly). Intravasation, infiltration of the blood or lymphatic vessels, requires several steps, beginning with the attachment of cancer cells to the stromal face of the vessel followed by degradation of basement membrane in the case of blood vessel infiltration and lastly trans-endothelial migration to pass between the endothelial cells of the vessel wall. Transport through the blood stream follows, with subsequent arrest and extravasation. The site of extravasation is determined by both the proximity of the organ to the primary site (first-pass organ) and the propensities of the cancer, cancer cells preferentially metastasize to different organs depending on primary site. During extravasation the cells must first arrest in the capillary bed of the secondary organ and then cross the endothelium of the vessel wall and into the parenchyma. Selectin-family adhesion molecules

(especially E-selectin), amongst others (e.g. integrins), are implied in the adhesion to vessel-endothelium. Notably selectins are differentially expressed in different organ-vasculatures, this probably leading to the preferences of metastasis by cancer origin. E-selectin is also implicated in the signaling cascade involved in trans epithelial migration. After crossing into the surrounding stroma, the cancer cells may establish and proliferate, giving rise to a novel tumor at the site. When grown past a certain size, the tumors will commonly also begin blood-vessel formation (by angiogenesis, vasculogenic mimicry or vasculogenesis) to maintain its nutrient supply [28].

The epithelial to mesenchymal transition is of great importance in the metastatic process (specifically migration and intravasation) for epithelial derived cancers. The epithelial to mesenchymal transition (EMT), is the process wherein an epithelial cell (or cells) loses its epithelial like characteristics and assumes the characteristics of a mesenchymal cell, giving enhanced invasive and migratory properties as well as reduced susceptibility to apoptotic signals. The process normally occurs within embryonic development and organogenesis but is subverted during chronic inflammation and neoplasia [29].

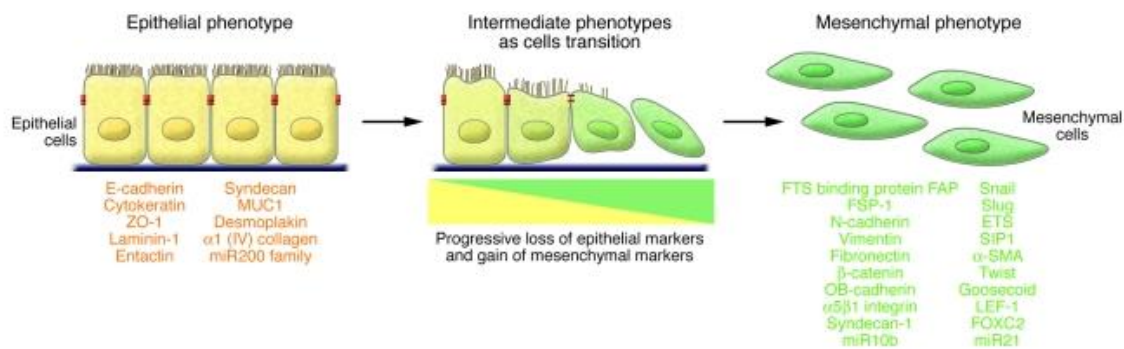


**Figure 1.5:** The epithelial to mesenchymal transition (EMT), with (left to right) progressive loss of epithelial characteristics (phenotype, reorganization of cytoskeleton degradation of cell-cell adhesion proteins and changes in protein expression) and gain of mesenchymal characteristics. Figure adapted from Kalluri & Weinberg 2009 [29].

Brain metastasis is governed by predominantly two factors: the high blood flow of the brain, constituting 15-20% of total blood volume in the body in a resting state, and the propensity of certain cancers toward brain invasion, where cancers of certain origins are much more inclined toward brain metastasis. Whilst brain metastases may spread to any region of the brain in principle, size of areas and vasculature circumference places limits to where cancer cells most typically spread, with 85% of metastatic spread occurring in the cerebral hemispheres [27]. Following the formation of brain metastases, after cells have come to arrest

in the brain capillary bed and extravasated across the blood brain barrier (BBB), mediated mainly by genes HBEGF, COX2 and ST6GALNAC5 as well as integrin activation, into the brain parenchyma, the novel secondary tumor may either grow along the preexisting vasculature (called vascular co-option) or initiate angiogenesis to recruit its own vasculature (Figure 1.6) [28, 30].

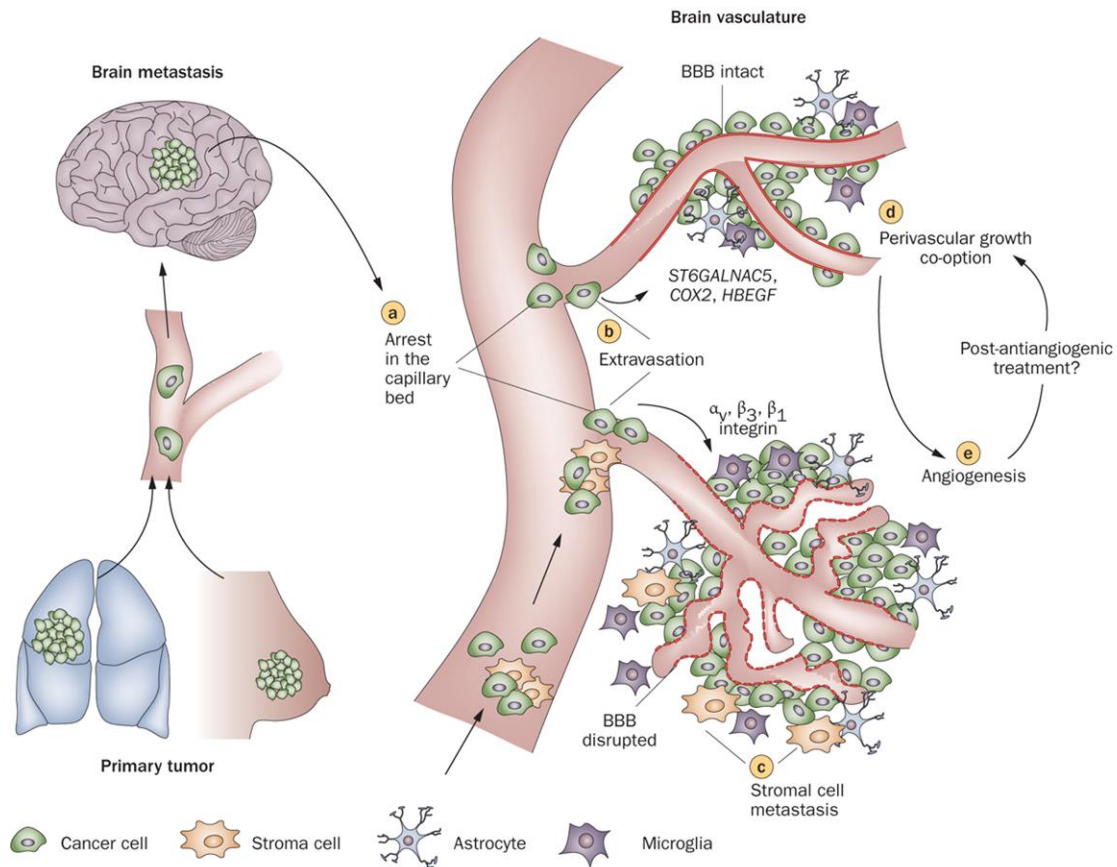


**Figure 1.6:** The brain metastatic process. Cells once disseminated from their primary tumor move along the vasculature until coming to arrest in the brain capillary bed, before extravasating through the BBB and forming secondary tumors within the brain. Following extravasation the tumor cells may either grow along the existing vasculature, or begin angiogenesis to form their own vasculature [30]. Figure adapted from A.F. Eichler 2011.

In the United States there are recorded approximately 200 000 new cases of brain metastatic cancers every year, 10 times the number of primary malignant brain tumors.

Out of all systemic primary cancers it is estimated that up to 40 % of cancer patients will progress to have brain metastases [31].

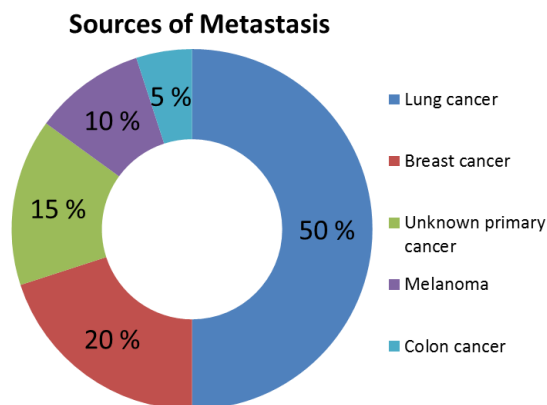


**Figure 1.7:** Primary sites of brain metastatic cancers by prevalence. The most common sites of origin are from lung cancer, breast cancer, melanoma and colon cancer.(Adapted from Bollig-Fisher et al. 2013) [31].

Varying estimates distribute brain metastatic cancers by the most common primary sites; 50-60% from lung primary tumors, 20-30% from breast and 5-10% from melanoma (Figure 1.7). The prognosis for patients with brain metastatic cancers are dismal with median treated survival with microresection and radiotherapy at 9-10 months [31].

### 1.7 Treatment of brain metastases

Administration of cortico-steroids is commonly done when patients have been found to harbour brain metastases. The mechanism of action whilst unclear is thought to be stabilizing the BBB to avoid vasogenic edema at sites of tumors. Anti-convulsants and anti-coagulants are also commonly administered to reduce the burden of symptoms, but without curative effect [32].

Whole brain radio-therapy (WBRT) is used with some success, extending median survival by 3-6 months, surgical excision in addition to WBRT extends median survival up to 10 months. Stereotactic radiosurgery also improves upon survival, increasing median survival up to 10 months, though the damage done by high radiation doses limits the application to low numbers of metastases, and radiation induced necrosis is difficult to distinguish from tumor derived necrosis in clinical MRI. Chemotherapeutics are not commonly used against brain metastases until radiotherapy and surgery have been exhausted as possibilities [32], as the intact BBB effectively protects small-size tumors from most drugs [33]. Few

chemotherapeutics can cross an intact BBB, e.g. nitrosureas and high dose methotrexate, and these have been of limited efficacy. SRS in multiple instances, salvage SRS, with recurrence of cancer, have as of yet the most prolonged median survival, giving an average extension of 7 months to survival. Combinations of WBRT and SRS were not found to be significantly better than WBRT alone, for patients with more than one metastasis, in a 2012 meta-analysis [32-34]. Stereotactic radiosurgery, where a high dose of radiation is administered to a targeted volume, have shown some improvement in localized control of tumors and overall survival in patients with melanoma brain metastases [35].

### 1.8 The Blood Brain Barrier

The Blood Brain Barrier (BBB) is a term used to describe the selective nature of the capillary vasculature in the brain towards diffusion. The constituents and structure of the BBB can be seen in Figure 1.7. This diffusion barrier excludes most substances from entering the brain parenchyma. The cellular components of the BBB are the endothelial cells of the vasculature, pericytes over these and astrocyte foot processes [36].

Tight junctions, and Adherence junctions between the endothelial cells of the brain vasculature limit the permeability of the brain parenchyma to water-soluble compounds from the blood-stream. Gap junctions are also thought to play a part among the BBB forming junctions, though evidence is not yet conclusive on the matter. Tight junctions are formed of trans-membrane proteins (e.g. occludins, claudins), and cytoplasmic proteins (e.g. zona occludens-1&2, cingulin) forming complexes linked to the actin cytoskeleton. Adherence junctions, responsible for cell-cell adherence of endothelial cells, constitute of (among others) cadherins (adherence points), catenins and actinin binding to the actin cytoskeleton. The brain microenvironment has been shown to induce BBB vascular characteristics in epithelial cells [37, 38].

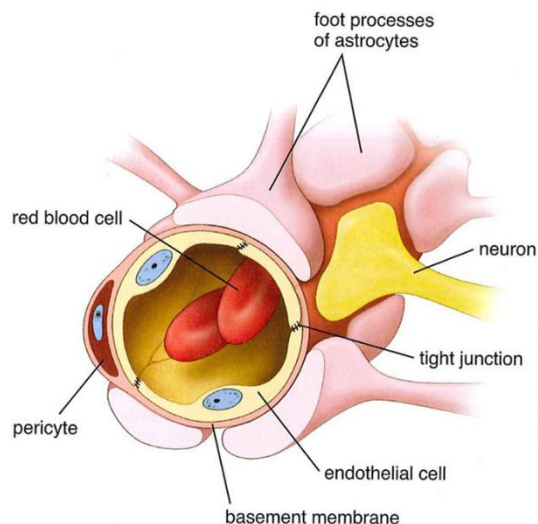


**Figure 1.8:** A Schematic overview of The Blood Brain Barrier (BBB). The BBB consists of endothelial cells with tight junctions, and pericytes around the endothelial cells, with the foot processes of astrocytes and neurons latching on over. (Figure provided by Frits Alan Thorsen).

The BBB demonstrates size, shape and charge exclusion of compounds, effectively excluding any compounds that are above 400Da in size or form more than 8 hydrogen bonds [39]. Of molecules smaller than the commonly assumed limit of 400Da, most are also found to be excluded, by the BBB, from entering the brain [40].

The selective nature of the BBB ensures that a large number of therapeutic compounds do not cross it, and are ineffective in treating conditions of the brain. For example brain metastases are notoriously difficult to treat clinically, as the BBB is disrupted late in brain metastatic development.

### 1.9 Permeabilizing the BBB

The selectiveness of the BBB severely inhibits delivery of larger treatment molecules (MW>400 Da) to brain tumors. Thus it has been a subject of some interest to identify strategies that would allow treatment agents to cross the BBB, either throughout the whole brain, or specifically at sites of disease. Several substances or procedures that permeabilize the BBB have been discovered, and in the following a few are mentioned:

Receptor expressions applicable as a target for selective treatment regimens were found for breast carcinomas. In a murine model, localized expression of the receptor Tumor Necrosis Factor Receptor 1 (TNFR1) was found to be inducible through administration of Tumor

Necrosis Factor 1 (TNF1) at sites of brain metastases, which in turn allowed for localized permeabilization of the BBB [41].

Increases in serum bile acid concentrations have also been shown to increase BBB permeability in rats, through either bile duct ligation, or intravenous administration [42].

The venom of the *Phoneutria nigriventer* spider has been shown to cause acute BBB permeabilization and vasogenic edema in rats. The venom consists of several distinct toxins, and possibly one in isolation could prove to modulate BBB permeabilization [43].

Certain solvents such as DMSO, ethanol and glycerol, have been shown to permeabilize the BBB at g/kg levels in animal studies, though these have been found of limited use in a clinical setting [40].

Mechanical permeabilization through focused ultrasound has been under development for some time. This technique has applicability at local identified sites of disease, for example metastases grown to a detectable size by clinical imaging. Clinical trials using doxorubicin administered in conjugation with ultrasound contrast agents, by MRI guided focused ultrasound (ExAblate system) are ongoing. The safety of this treatment strategy is currently being evaluated prior to clinical efficacy studies [44-46]. Sonic methods also offer strategies to targeted release, by bursting microbubbles at a targeted site. In this way higher concentrations of a drug, e.g. chemotherapeutic agents, may be administered locally, with less systemic toxicity due a lesser overall dose [47].

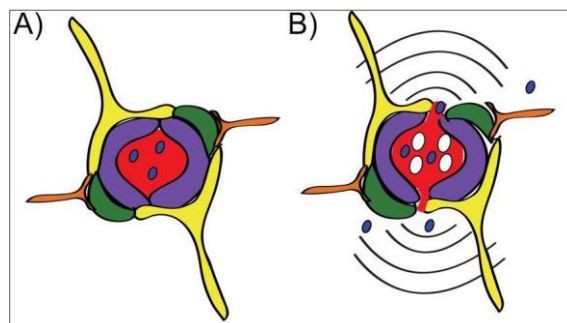


**Figure 1.9:** Opening the BBB through application of focused, directed ultrasound to targeted site. A) The normal state of the BBB, with tight association of capillary endothelium preventing exchange with brain parenchyma. B) Energy released by focused ultrasound forces cell junctions apart, allowing for exchange between brain parenchyma and vasculature. Figure adapted from Hynynen et al. 2013 [48].

Hypertonic solutions of various substances (e.g. Urea, arabinose, lactamide, NaCl, and mannitol) have been shown to open the BBB through a mechanism presumed to be osmotic, causing cell shrinkage opening up the BBB allowing plasma soluble agents access to the brain

parenchyma. BBB-permeabilization using mannitol in a hypertonic fashion was successfully implemented as a part of a combinatorial treatment regimen against brain metastatic adenocarcinoma in humans [49].

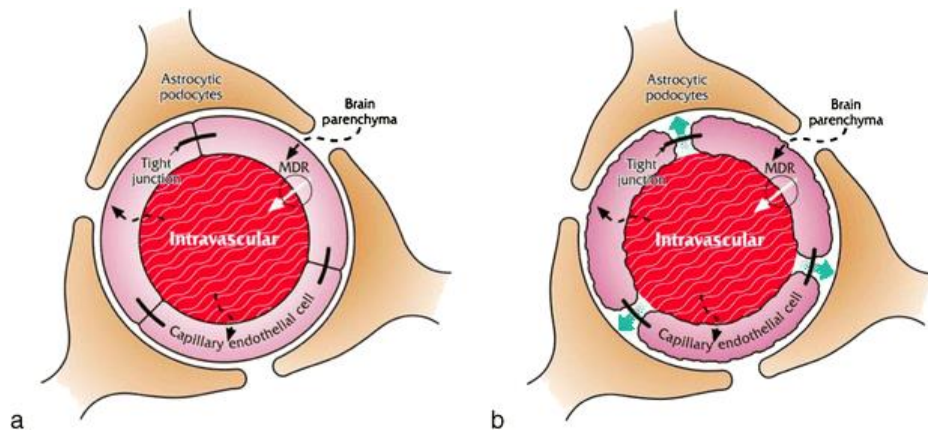


**Figure 1.10:** Hypertonic osmotic BBB permeabilization, a: depicts normal closed configuration of BBB, where most large molecules may not cross over to the brain parenchyma, b: depicts BBB as opened, due to cell shrinkage. Figure adapted from Bellavance et al. 2008 [49].

### 1.10 K16ApoE

The Low Density Lipoprotein Receptor (LDLR) has earlier been shown to be involved in substances crossing over the BBB. Transcytosis was postulated to be the mechanism by which the LDLR moved substances over the BBB [50].

A synthetic peptide constructed of the receptor binding domain of ApolipoproteinE (ApoE) with a 16 lysine tail (K16) for nonspecific protein binding, was constructed by Sarkar et al, which showed BBB permeabilizing abilities. The peptide was originally tested with Evans blue dye and various therapeutic agents, where the original study noted passage into the brain parenchyma of these substances [51].



**Figure 1.11:** Opening of the BBB after intravenous treatment with K16ApoE. **A)** The top row shows effects of administration of K16, ApoE compared to K16ApoE and difference between administering mixed with EB or immediately prior. **B)** The bottom row shows degree of leakage of EB into the brain parenchyma at different concentrations of K16ApoE. K16: 16 Lysine peptide, ApoE: ApolipoproteinE receptor binding domain, EB: Evan's Blue dye. Figure adapted from Sarkar et al. 2011 [52].

## 1.11 Models to Study Melanoma Progression

### 1.11.1 *In Vitro* Models

Culturing cells *in vitro* offers an ideal way for rapidly screening compounds for possible clinical efficacy as well as making naive observations about expression and growth of a specific cell type. The drawbacks of the approach includes a lack of interactions between microenvironment and cells, as well as immune mediated responses and other physiological parameters being mostly/completely absent.

There are various strategies to culture cells, ranging from simplistic monolayer growth, to more complex 3 dimensional approaches.

### 1.11.2 *In Vivo* Models (Xenografts)

#### *In Vivo* Cancer Metastasis Models

Of the animal models used to study the development and progression of cancers, two main categories exist: syngeneic models; where animal cancer cells are implanted into the same

type of animal (usually rats or mice), and xenograft models; where immune-compromised animals (mice or rats) are implanted with human cancer cells. Genetically engineered animal models where inserted somatic mutations lead to cancer predisposition, are commonly counted as variants of the syngeneic models. Models where tumor cells are injected into the blood stream are counted as ectopic, and models where cancer cells are implanted in the organ of origin as orthotopic [53, 54].

The discovery and selective breeding of B-cell and T-cell deficient animals have resulted in the development of numerous xenograft models. Mouse models are the most commonly used, exemplified in the Non Obese Diabetic Severely Combined Immunodeficiency (NOD/SCID) mice. Xenografts are developed from cultured biopsies that are introduced into the animals, where the take rate is usually high. The benefit of these models are the ability to specifically select the human cancer one wishes to study, and that these cells can be expected to behave similarly to as what they would in humans. The xenografts may be easily treated with drugs in for instance screening experiments and the results are more transferable to a clinical setting, e.g. when developing treatment regimens, compared to syngeneic models

There are several limitations to the use of immunodeficient and mice models in general. This is due to the fact that the animals have a weakened immune system, interactions with which are foregone in these models, and most immune mediated treatments are thus inapplicable as well. The fact that mice whilst being mammals are evolutionarily quite removed from humans, also limits the direct applicability of results [53-55].

### [Animal brain metastasis models](#)

The need for models to study brain metastasis in vivo is obvious, and several animal models using mostly immunocompromised animals and human xenografts, have been established. The progression of tumor growth in the animals were found to be closely similar to what had been observed clinically in patients, which was taken as a sign of their applicability and value [53].

## [1.12 Imaging](#)

### [1.12.1 Fluorescent microscopy & time-lapse microscopy](#)

Light microscopy is a method of using elemental concepts of optics to focus light beams from samples in order to view the samples at greater magnification.

Fluorescence microscopy, is based on the physical phenomena called fluorescence. Fluorescence being the reemission of light of longer wavelengths after absorption of light with a characteristic wavelength(Figure 1.12) [56].

The discovery of biological fluorochromes, initially Green Fluorescent Protein (GFP), has found wide usage in biochemical and medical research [57, 58].

The application of fluorochromes in what is called fluorescent microscopy has yielded a large variation on techniques exploiting the effect. The ability to attach visibly detectable tags to proteins or other cellular components allows for the study of intracellular positions as well as expression levels.

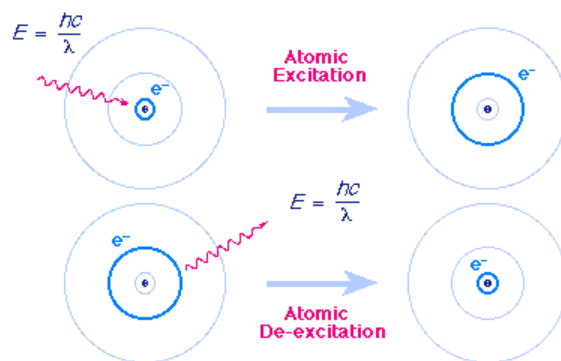


**Figure 1.12:** The physical process of fluorescence. Excitation of electron to higher energy level (shell) by photon of certain wavelength and subsequent emission, or de-excitation, wherein the electron returns to its original energy level with characteristic wavelengths of light corresponding to the energy difference being released. Figure adapted from University of Tennessee, Astrophysics Lecture notes [59].

Modern light microscopes are commonly conjugated with mercury lamps and light filtering systems. This allows them to expose a sample to specific wavelengths of light, as well as observing specific wavelengths alone, by also applying filters to detectors. As the wavelengths needed for excitations are different from those emitted by the subsequent emissions, only emitted light from fluorochromes will be visible in such a setup [56].

Time-lapse microscopy is merely the application of automated image acquisition to an existing microscopy/imaging technique, yielding a series of acquisitions from the same location(s) at several time points.

### 1.12.2 Electron Microscopy

Electron microscopy are the techniques of using accelerated electrons as the source of illumination in microscopy, made favorable by the smaller wavelengths of electron beams, comparative to the photon wavelengths of light. This allows for far greater resolution compared to light-microscopy. The electron microscope consists of an electron gun (filament to which a high voltage is applied), a cathode directing electrons toward and through the sample, magnetic coils acting as lenses (focusing and narrowing the electron beam) and a detector system, all encapsulated in a vacuum (needed to avoid the electrons interacting with anything other than the sample). The two basic types of electron microscopes are the Transmission Electron Microscope (TEM) and the Scanning Electron Microscope (SEM) (Figure 1.13) [60].

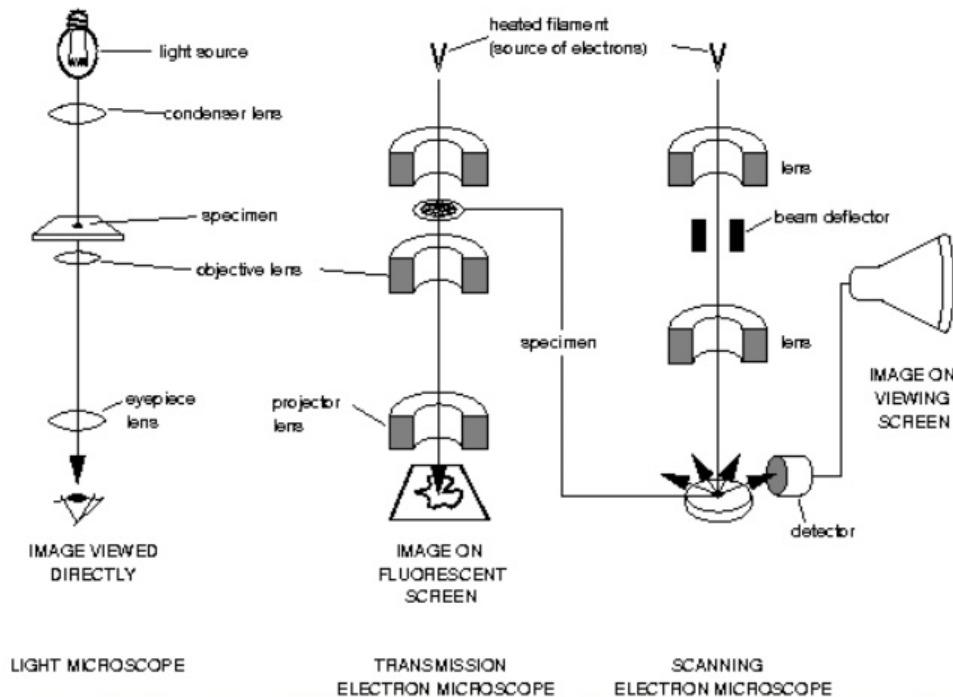


**Figure 1.13:** The two modes of electron microscopy; Transmission Electron Microscopy (TEM) and Scanning Electron Microscopy (SEM) compared to their predecessor light microscopy. TEM is based upon the attenuation of the electron beam through the sample, whilst SEM is based on secondary electrons from the surface of the sample. Figure adapted from Dr. Huvin Ganga [61].

### Scanning Electron Microscopy (SEM)

The Scanning Electron Microscope generates images of the (3D) surfaces of samples, by scanning a focused electron beam over the surface of an electrically conductive specimen (this is achieved by coating the specimen, typically with Gold or Palladium). This mode is not

homologous to conventional optical microscopy, but images are reconstructed from signals generated from secondary electrons, with brightness of a pixel corresponding to the number of secondary electrons generated from the surface of the sample [60].

### Transmission Electron Microscopy (TEM)

The transmission electron microscope was the first electron microscope developed and is homologous to the light microscope in its mode of operation. The electron beam behaves much the same way as light would due to the wave nature of particles. In TEM focused electron beams are directed through the sample, with brighter regions in the image corresponding to less obstruction of the electron beam by the sample. The use of TEM requires the samples to be finely sliced, dyed with metals, and only allows one to view small areas at a time, but at much greater resolution than SEM [60].

### 1.12.3 Magnetic Resonance Imaging (MRI)

#### The NMR signal

Nuclear Magnetic Resonance, the physical phenomena upon which NMR-spectroscopy and MRI are based, is the absorption and reemission of electromagnetic radiation by nuclei in a magnetic field. This is due to the fact that all isotopes with uneven proton and or neutron numbers have, due to the unpaired spin, a net magnetic moment. When in a strong magnetic field, the isotope has a resonance frequency ( $\omega_0$ ) called the *Larmor* frequency, proportional to the magnetic field strength ( $B_0$ ) and its gyromagnetic ratio ( $\gamma$ : a physical constant).

$$\omega_0 = \gamma B_0$$

Out of all the isotopes in a voxel (volume unit) a few more will align with the magnetic field (parallel) than against (anti-parallel), due to this being energetically slightly more favorable.

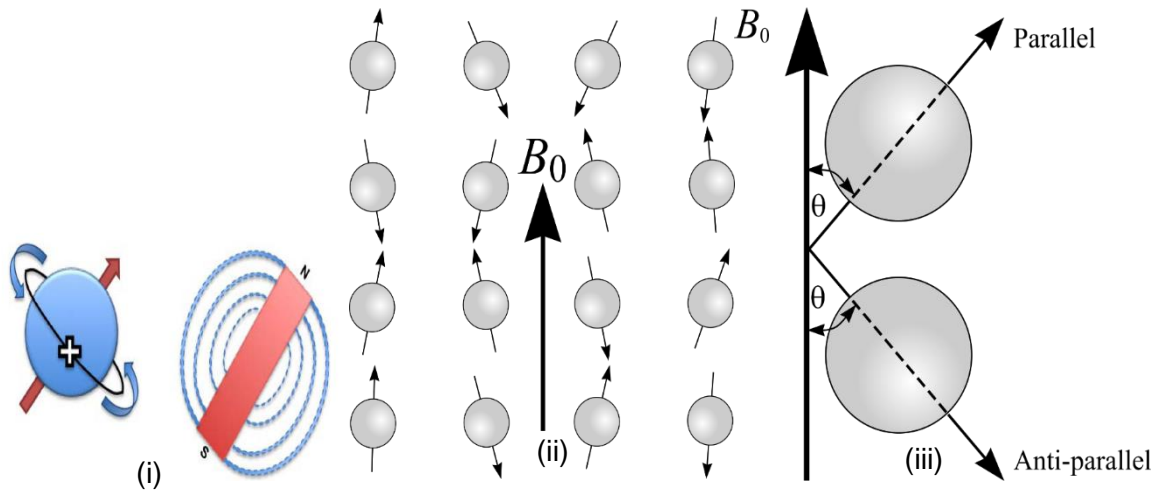


**Figure 1.14:** The proton spin analogized as a bar magnet and the orientation of proton spins within a magnetic field  $B_0$ , assuming parallel and anti-parallel states exemplified. (Figure adapted from (i) Frits Thorsen, (ii & iii) M. Puddephat [62]).

This small inequality of distribution, which is also proportional to field strength, is what gives an observable signal. The energy difference can be summarized as (where  $\Delta E$  is the energy difference,  $\hbar$  is Planck's constant/ $2\pi$ ,  $\gamma$  the gyromagnetic ratio, and  $B_0$  the magnetic field strength):

$$\Delta E = \gamma \hbar B_0$$

The resonance effects can be viewed as the spins being flipped out of alignment with the magnetic field. Having been disaligned the isotopes move in a rotating manner, called precession, back towards equilibrium, i.e. in alignment with the magnetic field.

The signal in NMR and MRI is generated by the induced magnetic flux resulting from the precessing spins re-aligning with the magnetic field, and takes the form of a free-induction decay signal.

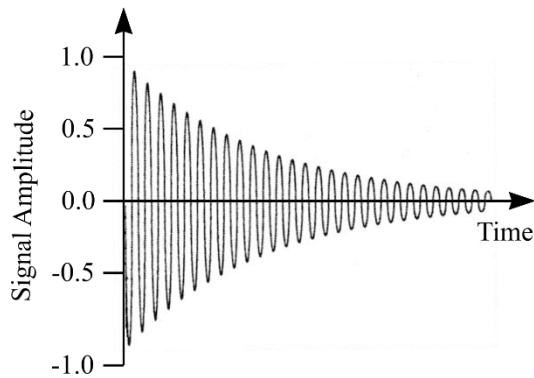


**Figure 1.15:** A free induction decay signal, where the amplitude, decreases in an exponential manner with time. [62] (Figure adapted from M. Puddephat).

The NMR-signal is constituted by two exponentially decaying processes,  $T_1$  and  $T_2$  relaxation. These are: The loss of magnetization in the longitudinal direction, or spin-lattice relaxation which is the return of the net magnetization to the direction of the magnetic field. The loss of magnetization in the transverse plane, or spin-spin relaxation (orthogonal to the magnetic field) which is the dephasing of spins, which had aligned at the time of excitation. These are commonly denominated as  $M_z$  and  $M_{xy}$ .  $T_1$  is the time constant where net magnetization has recovered to 63 % of its initial value in the longitudinal direction and  $T_2$  the time constant at which magnetization in the transverse direction has decayed to 37 %.

Spin-lattice relaxation is caused by the return of the net magnetization vector to the equilibrium position, whilst spin-spin relaxation is the dephasing of the spins which had aligned in-phase at time of excitation by microscopic effects and inhomogeneities.

The  $T_2$  relaxation is always shorter than the  $T_1$  relaxation, significantly so in vivo.

The most commonly used elemental isotope for clinical scanning is the Hydrogen  $^1\text{H}$  isotope (the most common isotope of hydrogen), which has benefits in both ubiquitous presence in tissues as well as having the strongest NMR signal of all known isotopes [63-66].

### Magnetic Resonance Imaging (MRI)

Due to uneven distribution of protons and differing magnetic microenvironments around them, a spatially encoded  $^1\text{H}$  NMR signal allows for differentiation of structures and tissue types. This is called Magnetic Resonance Imaging (MRI) [67].

MRI systems have additional magnets, inducing field gradients in z (parallel to magnetic field) and x,y directions (transverse plane), this is used to allow for spatial encoding of the resulting signal.

The application of a gradient in the z-direction, alters the resonance frequencies along the gradient, allowing for “slice-selection” i.e. choosing a slice of a certain position and width (width given by the gradient strength and RF-bandwidth) wherein to excite protons. This gradient is applied at the same time as the excitation RF-pulse.

The application of the phase encoding gradient is applied right after the slice selecting gradient and by altering their precession speed relative to the strength of the gradient felt by the protons along it. After the application of this gradient protons are again precessing at the same frequency, but now in different phases relative to their position along the gradient.

Frequency encoding is the last step in spatial encoding and happens simultaneous to acquisition. A frequency encoding gradient is applied altering the frequencies of the protons precessions relative to their position along the gradient.

The raw-data from an MRI acquisition is a two dimensional time-domain signal, this representation is often referred to as k-space. The spatially encoded signal can be reconstructed into an image via a mathematical operation known as the Fourier Transform, which converts a time-domain signal into its frequency components. In order for a two dimensional image to be reconstructed, a 2D Fourier Transform must be used [65, 66].

The Fourier Transform (in 1 Dimension):

$$F(\omega) = F[f(t)] = \int_{-\infty}^{\infty} f(t)e^{-i\omega t} dt$$

There are many variations in RF-pulse sequences and gradient settings used in MRI acquisition, allowing for more rapid acquisitions, different contrasts and different geometries of acquisition, as well as different reconstructions from k-space data. The variations in and theories for these go far beyond the scope of this introduction.

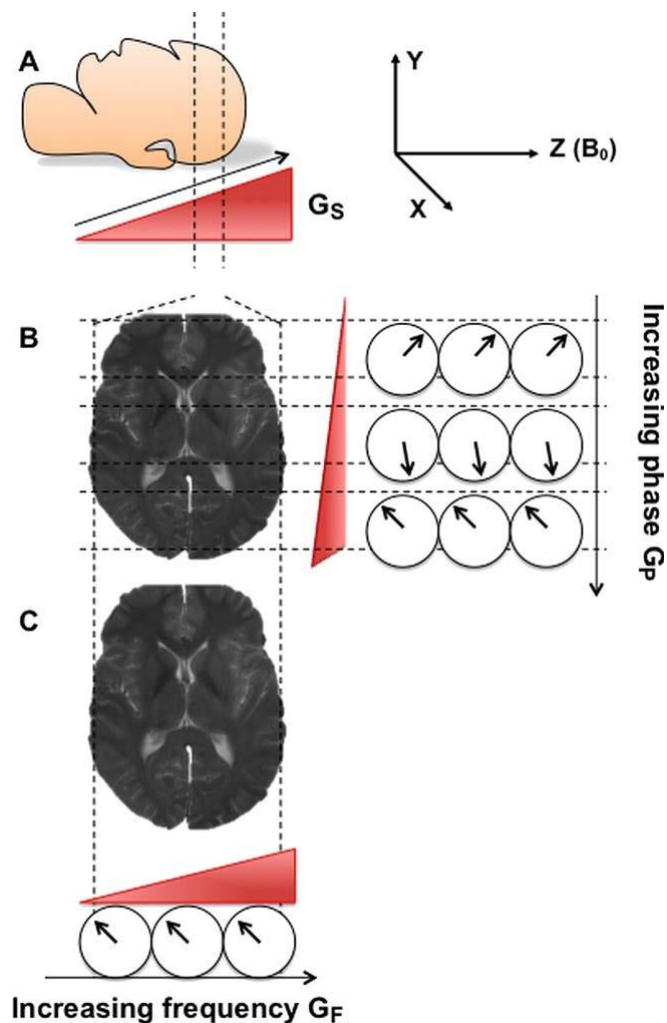


**Figure 1.16:** Illustration showing principles of the slice-selecting gradient, phase encoding gradient and frequency encoding gradient. **A** slice selection gradient, assures that different positions along it have different resonance frequencies, allowing to select a slice of a given width by choosing a bandwidth for the RF-pulse. **B** The phase encoding gradient alters the phase of protons such that their phase corresponds to their position along the phase encoding gradient. **C** The frequency encoding gradient applied at time of acquisition alters the frequencies of protons along it, thus encoding position along itself. [66] Adapted from Currie, S. et al. 2013.

### Contrast enhancement and DCE-MRI

Contrast enhancement in MRI is the use of several different compounds, called contrast agents, which affect the relaxation rates of their surroundings, leading to increase or decrease in signal.

The relaxation rates of tissues are the characteristic deterioration of signal characterized by the time-constants  $T_1$  and  $T_2$ . Relaxivity is the term used about the ability of a contrast agent to influence the relaxation rates of its surroundings which is governed by the following

expression:  $\frac{1}{T_i} = \frac{1}{T_i^0} + r_i[CA]$ ;  $i = 1 \text{ or } 2$  where  $r$  stands for relaxivity and  $[CA]$  for the concentration of contrast agent [68].

This allows one to more clearly differentiate anatomical structures, and detect pathology such as brain tumors, by the leakiness of blood vessels within tumor tissue.

Dynamic Contrast Enhanced – MRI or DCE-MRI is the use of a time series where images are sequentially taken of the exact same location over a set course of time whilst the contrast agent is administered. The measured change in  $T_1$  and  $T_2$  values is used as an indicator of the degree of perfusion of contrast agents within the region of interest.

To model this a simple two-compartment model is used where the compartments are commonly divided into extracellular extravascular space (EES) and capillary vascular plasma space ( $V_p$ ).

The general rate equation:

$$v_e \frac{dC_e(t)}{dt} = K_{1,2}[C_p(t) - C_e(t)]$$

This general differential rate equation describes the rate of accumulation and wash-out of contrast agents in the EES,  $C_e$  is the concentration of contrast agents in EES,  $C_p$  is the concentration of contrast agents in  $V_p$ .

Of particular use is the ability of this method to assess to what extent the BBB is open or leaking, with different kinetics observable in such a case [69, 70].

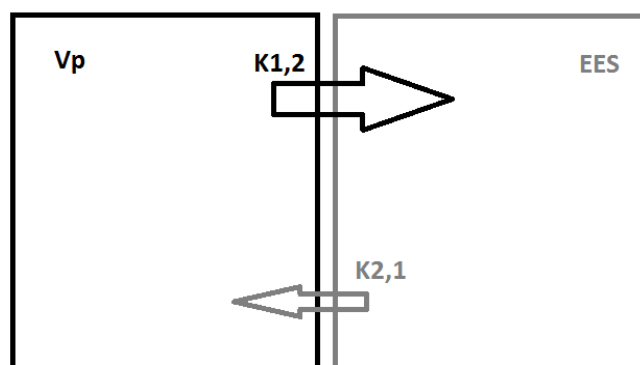


**Figure 1.17:** Tofts two compartment model for contrast agent behavior over time. The rate constant  $K_{1,2}$  or  $K^{\text{trans}}$  governs the movement of contrast into the extracellular extravascular space, and the rate constant  $K_{2,1}$  describes the transfer of contrast agents back into the vasculature. Figure based upon Tofts et al. 1999 [70].

#### 1.12.4 Bioluminescence Imaging (BLI)

There are several naturally occurring species that exhibit a phenomena called luminescence, wherein an enzymatic reaction of a special substrate produces visible light emissions. The most widely known such species is the firefly, the enzyme from which, amongst others, has also been adapted for the imaging technique known as bioluminescence imaging (BLI).

The substrate-enzyme pair (of which there are several) is called luciferin and luciferase.

This method allows for cells to be tracked *in vivo* (or *in vitro*) by adding the substrate or having the substrate produced in the cells themselves.

The reaction can be simplified as follows for understanding the basic principle:



In-vivo BLI is usually conducted by injecting anaesthetized animals containing tumor cells bearing luciferase genes, with the substrate luciferin and imaging the animal using a detection system or photon counter for visible light, within a light-proofed container.

The number of photons counted, corresponding to the number of reactions, by the detection system over a region of interest will be proportional to the number of cells expressing the luciferase enzyme in the region of interest (ROI). This indicates the presence of cells (above a certain threshold) and yields information on relatively how many cells are present in the ROI [71-73].

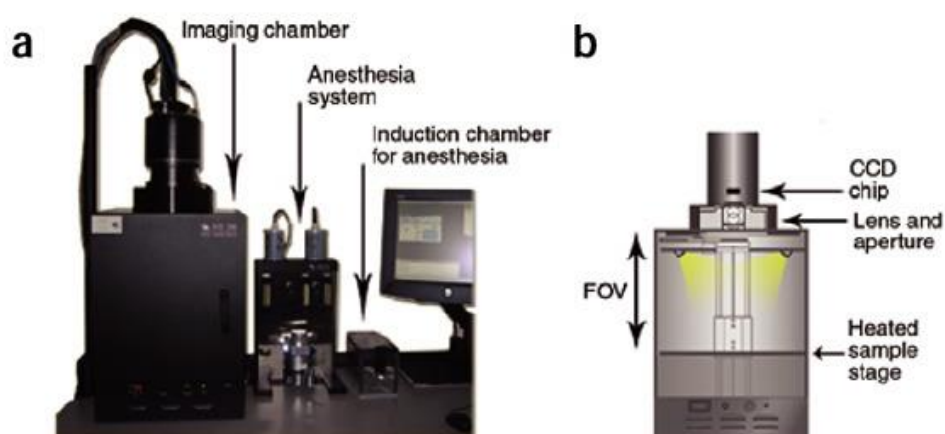


**Figure 1.18:** A typical setup of an optical imager used in Bioluminescence Imaging (BLI). The system has a light-proof imaging chamber containing the animal and a photon detecting system which feeds to an external computer, and gas anaesthesia required to keep the living animal immobilized. The system depicted is the Xenogen IVIS100. [74] Figure adapted from Franke-Fayard et al. 2006.

## 2 Aims of this Study

The main aim of this thesis was to study the *in vitro* and *in vivo* effects of a novel peptide K16ApoE, previously reported to open the blood-brain barrier. The sub-aims were:

- To demonstrate by DCE-MRI that K16ApoE opens the BBB.
- To study by DCE-MRI how long the BBB remains open after administration of K16ApoE.
- To study mechanisms of action of K16ApoE *in vitro*.
- To study treatment effects of vemurafenib on brain metastasis *in vivo*.
- To study treatment effects of vemurafenib on brain metastasis *in vivo* after opening the BBB with K16ApoE.

## 3 Materials and Methods

### 3.1 In Vitro

#### Cell lines used:

**H1\_DL2:** derived from secondary brain tumor (metastatic melanoma) from a 38 year old woman operated at Haukeland University Hospital. The cells have been transduced with GFP and firefly luciferase genes [54].

**SV80:** human lung fibroblast cell line, SV-40 transformed [from ATCC].

**RBE4:** Rat brain endothelial cell line, kindly provided by professor Aschner of Vanderbilt University.

**MDCKII:** Madin-Darby canine kidney epithelial cell line, kindly provided by professor Yliperttula of the University of Helsinki. A version of this cell line was created during this study: MDCKII mcherry, which was transduced with the mcherry fluorescent protein.

**HUVEC:** Human vascular endothelium cell line [from ATCC].

**Flow-cabinet:** All cell culture work, and preparations of injection solutions were done in a laminar flow cabinet (Heraeus; Hera Safe).

## Medium and solutions:

<b>ALT-DMEM</b>	<b>HUVEC medium</b>
450 mL Dulbeccos Modified Eagles medium (Sigma D5671)	F12-K medium (ATCC 30-2004)
50 mL inactivated Fetal Bovine Serum (Fisher Scientific A15-043)	50 mL Fetal Bovine Serum (Fischer Scientific)
10 mL 200mM L-Glutamine (Bio Whittaker BE17-605E)	50 mg Heparin Sodium Salt (Santa Cruz 203071)
10 mL Penicillin/Streptomycin (Bio Whittaker DE17-603)	15 mg Endothelial Cell Growth Supplement (Sigma 2759)
16 mL non-essential amino acids (100X) (Bio Whittaker BE-114E)	
100 µL Plasmocin 25 mg/mL (Invitrogen)	
100µL Puromycin (Invitrogen)	
<b>MDCKII medium</b>	<b>RBE4 medium</b>
465 mL Dulbeccos Modified Eagles medium (Sigma)	225 mL Hams F10 nutrient mix (Thermo Fisher Scientific)
5 mL Penicillin/Streptomycin (Bio Whittaker)	225 mL Minimum Essential Medium (MEM) (Thermo Fischer Scientific)
5 mL 200 mM L-Glutamine (Bio Whittaker)	5 µL Human recombinant Fibroblast Growth Factor ( )
25 mL Fetal Bovine Serum (Fischer Scientific)	50 mL Fetal Bovine Serum (Fisher Scientific)
	150 mg geneticin
<b>Trypsin</b>	<b>PBS</b>
Trypsin EDTA 0.25 % (Bio Whittaker)	Dulbeccos Phosphate Buffered Saline (Sigma-Aldrich)

**Vemurafenib (PLX4032):** BRAF(V600E) specific small molecule inhibitor. Purchased from Chemietek, Indianapolis, Indiana, USA.

**K16ApoE:** The BBB permeabilizing peptide used in this study, was first produced by Dr. Gobinda Sarkar (Dept. of Laboratory Medicine and Pathology, Mayo Clinic, Rochester, MI, USA) thereafter by Senior Researcher Dag Erlend Olberg (Norwegian Medical Cyclotron Centre, Oslo) and delivered as a desiccated powder. The complete sequence of the peptide is: NH<sub>2</sub>-KKKK KKKK KKKK KKKK LRVR LASH LRKL RKRL LRDA-NH<sub>2</sub> [52]. The molecular mass of the peptide is Mw=4521.79 the charge is 24 and the isoelectric point = 12.85.

### **Freezing solutions for cell lines:**

Freezing solution for H1\_DL2 & SV80:

Solution 1: 10 % FBS (Fetal Bovine Serum) in ALT-DMEM,

Solution 2: 20 % DMSO in PBS.

Freezing solution for H1\_DL2 and SV80 cell lines: 1:1 Solution 1 & Solution 2.

Freezing solution for RBE4 and MDCKII cell lines: Growth medium supplemented with 7.5 % DMSO.

Freezing solution for HUVEC cell line: Growth medium supplemented with 5 % DMSO.

### **3.1.1 General Cell Culture Work**

H1\_DL2 & SV80 cell lines maintenance:

The cells were cultured in monolayers in cell culture medium, in filter capped cell culture flasks (Nalge Nunc International, Rochester New York USA) of sizes 25 cm<sup>2</sup>, 75 cm<sup>2</sup> or 175 cm<sup>2</sup>. The cells were kept in an incubator with 5 % CO<sub>2</sub>, 100 % humidity and 37°C. The cells were passaged when confluent, for use, or maintenance (removal of superfluous cells).

Passage was done by washing the cells with PBS (2, 3 or 4 mL PBS according to the size of the flask), followed by trypsinization of the monolayer (2, 3, or 4 mL Trypsin-EDTA) for 5 min in the incubator. Then growth medium (3, 4, or 5 mL medium) was added to inactivate

the Trypsin. The resulting cell solution was then diluted to the appropriate concentration for in vitro experiments, or transferred (2-9 mL, as desired) to a new culture flask.

RBE4 & MDCKII cell line maintenance:

The cells were grown in collagen coated T75 culture flasks (Nunc) ( $7.5 \mu\text{g}/\text{cm}^2$  collagen; 10 mL of  $56.25 \mu\text{g}/\text{mL}$  type 1 rat tail collagen solution in PBS). The cells were grown to 80 % confluence before passage, with medium change every second day. Passage was done by washing the cells with PBS (3 mL PBS), trypsinization to dissolve monolayer (3 mL Trypsin-EDTA) for 5 min in the incubator, and 4 mL was added to inactivate the Trypsin. The resulting cell solution was then diluted to appropriate concentrations for in vitro experiments, or transferred (2-7 mL, as desired) to a new culture flask.

HUVEC cell line maintenance:

The cells were cultured in monolayers in filter capped cell culture flasks T25, T75, T175 (Nunc) in cell culture medium. The cells were kept in an incubator with 5 %  $\text{CO}_2$ , 100 % humidity and  $37^\circ\text{C}$ . The cells were passaged when confluent, for use, or maintenance (removal of superfluous cells). Passage was done by washing the cells with PBS (2, 3 or 4 mL PBS), followed by trypsinization of the monolayer (2, 3, or 4mL Trypsin-EDTA) for 5 min in the incubator. Then growth medium (3, 4, or 5 mL medium) was added to inactivate the Trypsin. The resulting cell solution was then diluted to the appropriate concentrations for in vitro experiments, or transferred (2-9 mL, as desired) to a new culture flask.

Freezing procedure H1\_DL2 & SV80:

The cells were grown to confluence in a large culture flask ( $175 \text{ cm}^2$ ). The cells were then washed with 4 mL PBS, trypsinized with 4 mL Trypsin for 5 min in the incubator, after which 5 mL medium was added to stop trypsinization. The cell solution was then transferred to a 10 mL tube and centrifuged at 900 rpm for 4 min, subsequently medium was removed and the pellet resuspended in freezing solution. The cells in freezing solution were then divided into 4 cryotubes (pr. large flask), placed in a  $-80^\circ\text{C}$  freezer for 24 hours, before being transferred to a liquid nitrogen tank for prolonged storage.

Freezing procedure for RBE4 and MDCKII:

The cells were grown to confluence in a large ( $175 \text{ mm}^2$ ) culture flask coated with collagen ( $7.5 \mu\text{g}/\text{cm}^2$ ). The cells were washed with 4 mL PBS, trypsinized for 15 min with 4mL Trypsin in the incubator, after which 5 mL medium was added to stop trypsinization. The cell

solution was then transferred to a 10 mL tube and centrifuged at 900 rpm for 4 min, the medium was removed and the pellet resuspended in freezing solution. The cells in freezing solution were then divided into 4 cryotubes (pr. large flask), placed in a -80°C freezer for 24 hours, before being transferred to a liquid nitrogen tank for prolonged storage.

Freezing procedure for HUVEC:

The cells were grown to confluence in large culture flasks (175 cm<sup>2</sup>). The cells were then washed with 4 mL PBS, trypsinized with 4 mL Trypsin for 5 min in the incubator, after which 5 mL medium was added to stop trypsinization. The cell solution was then transferred to a 10 mL tube and centrifuged at 900 rpm for 4 min, the medium was removed and the pellet resuspended in freezing solution. The cells in freezing solution were then divided into 4 cryotubes (pr. large flask), placed in a -80°C for 24 hours, before being transferred to a liquid nitrogen tank for prolonged storage.

Transfection of MDCKII with mcherry:

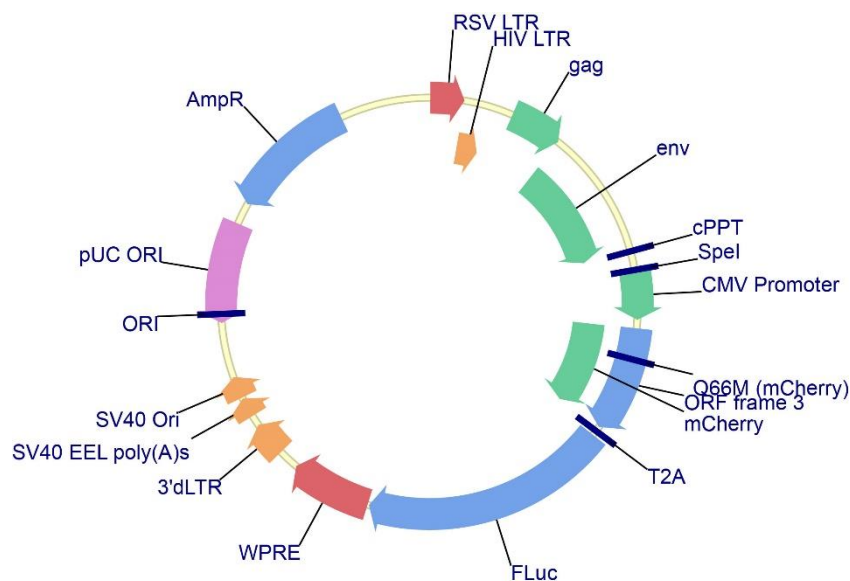


**Figure 3.1:** pGreenFire, HIV-based lentiviral vector, used for viral vector mcherry transduction. (System Biosciences, Paulo Alto, California, USA). Figure provided by supplier.

The cells were grown to partial confluence (ca. 40 %) in a small culture flask, before 2 mL medium containing pGreenFire lentiviruses containing mcherry was added. The manufacturing of the virus medium was performed by others in the lab, and was beyond the scope of this thesis. The cells were incubated in the virus medium for 24 hours at 37°C and 5 % CO<sub>2</sub>, before the virus medium was replaced with normal growth medium, and grown to

confluence before being passaged to a medium culture flask. Cells expressing red fluorescent protein mcherry were sorted by flow-cytometry (BD LSRFortessa, BD Biosciences, Franklin Lakes, NJ, USA).

### 3.1.2 Resazurin-resorfin Cell Viability Assay

A resazurin-resorfin viability assay was performed in order to assess the viability of cells post treatment with either vemurafenib, to establish its efficacy or K16ApoE to evaluate its cytotoxicity. The assay determines the percentage of a fluorescent metabolite converted (from resazurin to resorfin), as this metabolic activity is a measure of cell viability.

The cells were seeded (4000 cells/100  $\mu$ L per well) in 96 well-plates. 24 hours after seeding the cells, they were treated with different concentrations of vemurafenib (0.001  $\mu$ M, 0.01  $\mu$ M, 0.1  $\mu$ M, 0.5  $\mu$ M, 1  $\mu$ M, 5  $\mu$ M, 50  $\mu$ M or 100  $\mu$ M) or K16ApoE (0.1  $\mu$ g/mL, 1  $\mu$ g/mL, 20  $\mu$ g/mL, 40  $\mu$ g/mL, 60  $\mu$ g/mL, 80  $\mu$ g/mL, 100  $\mu$ g/mL or 150  $\mu$ g/mL). The following controls were also set up: DMSO-control at the same concentration as in highest vemurafenib dose, cells in only medium, and medium without cells (the vemurafenib experiments). Cells in medium alone and medium without cells (the K16ApoE experiments).

72 hours after adding vemurafenib cells were treated for 4 hours (in incubator) with resazurin 0.01 mg/mL (the vemurafenib experiments). 45 minutes after adding K16ApoE medium containing K16ApoE was replaced with fresh growth medium, and cells were then treated for 4 hours (in incubator) with resazurin 0.01 mg/mL (the K16ApoE experiments). Subsequently fluorescence at 560-590 nm was measured using a Wallack/Perkin Elmer 1420 VICTOR3 plate reader (Perkin Elmer, Waltham, MA, USA).

Statistics and plots were done using the Graphpad PRISM <sup>TM</sup> software (v7.00, GraphPad software, La Jolla, CA, USA).

### 3.1.3 Morphological light microscopy

To assess morphological differences in H1\_DL2 melanoma cell line cells treated with vemurafenib, light microscopy was performed.

H1\_DL2 cells were seeded at  $10^5$  cells per well in 2 mL medium in 6-well well-plates, thereafter allowed to attach and grow over 24 hours in incubator. After 24 hours medium was removed and 3 wells were treated with vemurafenib at a concentration of 50  $\mu$ M in growth medium, the other half served as an untreated control group.

The cells were imaged using a NIKON TE2000 (Nikon, Tokyo, Japan) microscope at 24, 48 and 96 hours post-treatment.

#### 3.1.4 Time-lapse fluorescence microscopy

In order to assess membrane stability of cells treated with K16ApoE, time-lapse fluorescence microscopy of MDCKII cells transduced with fluorescent protein mcherry, and H1\_DL2 which already expressed GFP, was performed.

The cells were seeded at 20-50,000 cells/500  $\mu$ L per well in ibidi®  $\mu$ slide 4-well well-plates (ibidi GmbH, Martinsried, Germany), coated with 7.5  $\mu$ g/cm<sup>2</sup> for MDCKII cells, and without collagen for H1\_DL2 cells, overnight to allow attachment.

The cells were treated with varying concentrations (0, 80, 100  $\mu$ g/mL) of K16ApoE diluted in growth medium and imaged using the appropriate color channel of the fluorescence microscope (NIKON TE2000), with one image taken every 30 seconds over the course of 1 hour.

The images were analyzed using the ImageJ software (National Institute for Health, Bethesda, Maryland, USA) with an ND2 (NIKON) file format plugin, converted to binary image using Otsu's method [75] (in group variance minimization = inter-group variance maximization) and the 'analyze particles' function was used to quantify the results.

#### 3.1.5 Electron Microscopy

Electron microscopy was used in order to ascertain morphological effects of K16ApoE on epithelial cell lines RBE4 and MDCKII. All EM proceedings were done with assistance by UiB Molecular Imaging Centre (MIC) staff, and all specialized reagents for EM were provided by MIC in conjuncture with EM-procedures.

For electron microscopy the cells were seeded in the wells of 24-well plates (Nunc), collagen coated 7.5  $\mu$ g/cm<sup>2</sup>, with 12mm  $\varnothing$  coverslips for SEM and without for TEM. Cells were seeded in 500  $\mu$ l of growth medium containing approximately  $4 \cdot 10^5$  cells. The cells were grown to complete confluence prior to treatment with the varying doses of K16ApoE (20, 40 & 80  $\mu$ g/ml). After 45 minutes the cells were fixed with 2.7 % Glutamic acid aldehyde (60  $\mu$ l 25 % solution added directly). The cells were subsequently washed 2 times with Sodium Cacodylate buffer 0.1 M, before being post fixated with OsO<sub>4</sub> 0.1 M in 0.1 M Sodium

Cacodylate buffer, then washed again 2X with Sodium Cacodylate buffer 0.1 M. The cells were dried for 15 minutes in 30, 50, 70, 96, & 2x100 % ethanol, prior to SEM or TEM specific procedures.

#### Scanning Electron Microscopy (SEM)

Critical point drying was done on the cover slips for SEM, and then coated with 5nm Cd-Au alloy, using a JEOL JFC-2300HR High Resolution Fine Coater (JEOL Ltd., Tokyo, Japan).

SEM was performed with a Scanning Electron Microscope JEOL JSM-7400F (JEOL Ltd., Tokyo, Japan).

#### Transmission Electron Microscopy (TEM)

Cells for TEM were cast into Agar100 (Agar Scientific Ltd. Essex, UK) resin, first 1:1 resin:100 % EtOH, hardened overnight at 37<sup>0</sup>C, then empty gelatin capsules were embedded in the resin, pure resin added and incubated at 60<sup>0</sup>C overnight, before capsules were filled with pure resin and solidified at 60<sup>0</sup>C. The TEM samples were then sliced to the desired thickness with the REICHERT ULTRACUT S microtome (Leica AG, Wien, Austria).

TEM was performed using a Jeol JEM-1230 transmission electron microscope (JEOL Ltd., Tokyo, Japan).

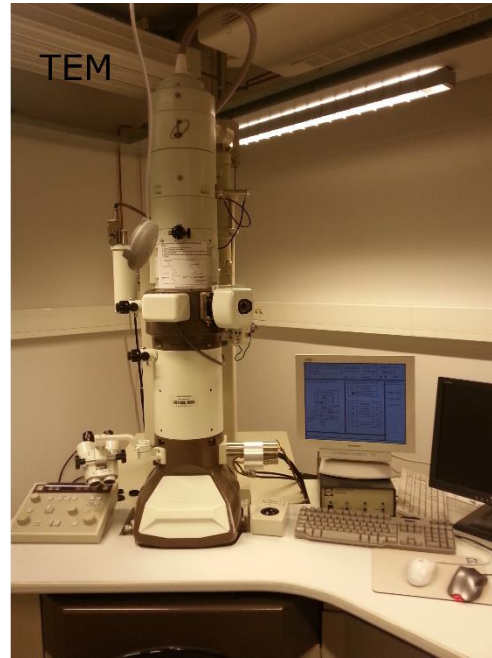


**Figure 3.2:** The electron microscopes used for this study. **SEM:** The Jeol JSM-7400F scanning electron microscope. **TEM:** The Jeol JEM-1230 transmission electron microscope. Both microscopes situated at the Molecular Imaging Centre core facility (University of Bergen).

## 3.2 In Vivo

### Mice and Housing Conditions

The mice used in the study were NOD/SCID Non-Obese Diabetic Severe Combined Immune Deficient mice, bred at the animal facility at Haukeland University Hospital.

Mice were kept in groups of 2-4 in cages with woodchip bedding and enrichments, feed-pellets and water provided ad libitum.

All procedures were approved by the National Animal Research Authority (application 8093).



**Figure 3.3:** The Bruker Pharmascan® 7T small-animal MRI used in this study. Connectors for animal bed water-heating and anesthesia (sevoflurane) visible. Animal bed and coils not mounted in picture.

### 3.2.1 K16ApoE kinetics studies, DCE-MRI

DCE-MRI was performed using the 7 Tesla Bruker Pharmascan 70/16 (Bruker Biospin AG, Ettlingen, Germany) small animal MRI (Figure 3.3), with a 72mm quadrature transmit coil and mouse brain array receive coil, in order to evaluate the quality and duration of BBB permeabilization.

K16ApoE was administered 200  $\mu\text{g}$  in 100  $\mu\text{l}$  PBS via tail-vein catheter (Figure 3.4A) over a duration of 60 seconds. Ominscan® contrast agent (Gd-diamide, GE Healthcare, Little Chalfont, UK) was administered at the time of scan, also by using a tail-vein catheter, connected to an automated syringe pump PHD2000 (Harvard Apparatus, Holliston, MA, USA). A bolus of 0.5  $\mu\text{mol/g}$  (solution 0.1mmol/ml volume adjusted to animal weight) was injected over 20 seconds. 2\*50cm catheters were used to reach animal inside scanner, dead-volume: 30 $\mu\text{l}$ /50cm tubing. All animals were anesthetized with sevoflurane for injections and scans (5 % for induction and 2.5 % for maintenance) (Figure 3.4B).

Control animals were administered 100  $\mu\text{L}$  saline instead of K16ApoE (9 mg/mL, Fresenius Kabi AG, Bad Homburg, Germany) prior to DCE-MRI.

For the first few scans a T1 weighted DCE sequence with: TR=15ms, TE=2.1ms, FA=17°, was used, obtaining 1500 images. Thereafter the DCE-sequence was shortened to obtaining 900 images. The scan was initiated 15 seconds prior to bolus-injection of Omnican contrast agent. The images were acquired with ParaVision v5.1 software, and DCE analysis was performed using the NordicIce v4.04 software (NordicNeuroLab, Bergen, Norway) on an offline workstation. Area under curve (AUC, the definite integral of the concentration time-curve of contrast agent) and volume transfer coefficient ( $K_{1,2}$ ) were determined for a region of interest (ROI) encompassing the brain. For older scans with 1500 images, only the first 900 were used in the analysis to be comparable to later scans.

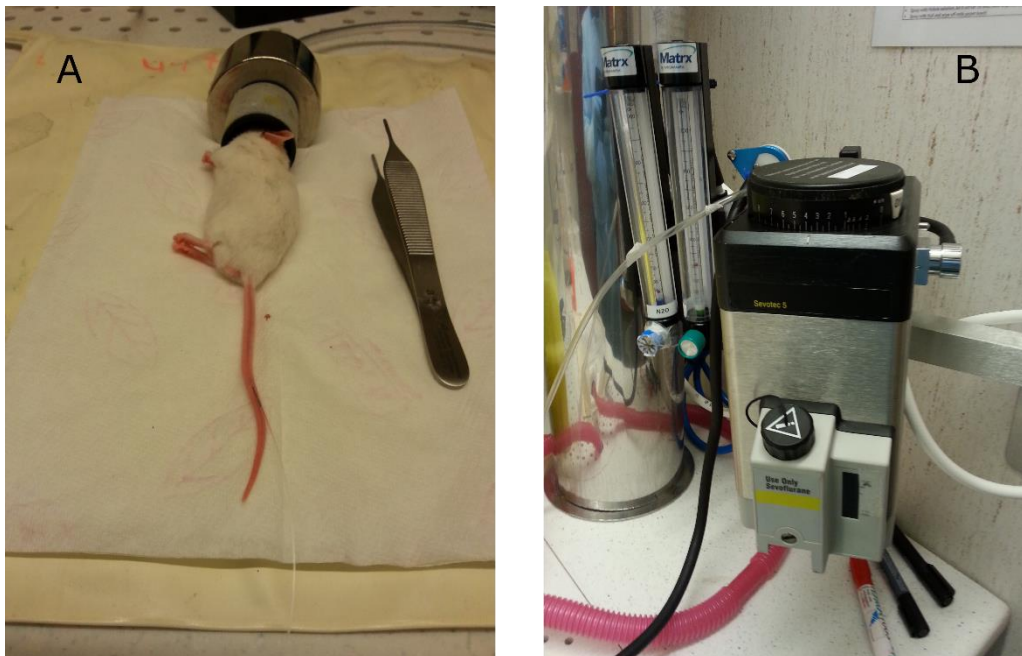


**Figure 3.4:** Tail vein injection setup and anesthesia vaporizer **A)** Mouse with tail-vein catheter inserted, lying on heating blanket. **B)** Sevotec 5 inhalation anesthetic vaporizer, (GE-Healthcare, Madison, Wisconsin, USA) sevoflurane inhalation system used for gas-anesthesia.

### 3.2.2 Mouse Xenograft Model

The mice were anaesthetized using 5 % isoflurane gas-anesthesia before cells were injected, ( $5 \times 10^5$  H1\_DL2 cells suspended in 0.1 ml PBS), into the left ventricle using a 30G insulin syringe (Omnican, B.Braun AG Melsungen, Germany) guided by ultrasound. The mice were given 0.05 ml Buprenorphine hydrochloride (Buprenex, Cardinal Health, Elk Grove, CA, USA) 0.05-0.1 mg/kg subcutaneously for post injection analgesia.

### 3.2.3 Pilot Treatment Experiment

In order to assess potential clinical efficacy when treating brain metastases, xenografted mice were treated with either K16ApoE and vemurafenib, or vemurafenib alone.

A group of 5 mice were injected intra-cardially with  $5 \times 10^5$  H1\_DL2 cells in 0.1ml PBS, and divided into two groups of treatment; three animals (2females, 1male) for combinatorial treatment with K16ApoE and vemurafenib, and two (1female, 1male) for treatment with vemurafenib alone. The treatment was started 9 days after tumor cell injection.

K16ApoE diluted to 2mg/ml in PBS was administered intravenously at a volume of 100 $\mu$ l, corresponding to 200 $\mu$ g per animal, twice a week to the relevant animals. Animals receiving K16ApoE were anesthetized with sevoflurane during injections (5 % for induction, and 2.5 % for maintenance). Vemurafenib (14.7 mg/ml in 60 % DMSO and 40 % PBS) was administered intraperitoneally at a dose of 50mg/kg every weekday of the study to all animals.

The animals were weighed twice a week through the entire pilot.



**Figure 3.5:** Timeline of Pilot Study.

#### 3.2.3.1 BLI

At week 4 the animals were imaged using BLI to confirm growth and presence of H1\_DL2 cells within the animals.

The animals were injected with 150 mg/kg D-luciferin intraperitoneally and imaged 10 min post-injection using the Optix SX-470 small animal Optical imager (Advanced Research Technologies Inc. Saint Laurent, Canada). Imaging was done with animals in prone and supine position. Image acquisition and analysis was done using the Optix Optiview software v2.001. The animals were anaesthetized with sevoflurane in an inhalation system for the duration of the scans (5 % for induction, 2.5 % for maintenance).

### 3.2.3.2 MRI (T1, T2, T1-contrast – anatomical scans)

Mice were anaesthetized and maintained with sevoflurane during all scans (5 % for induction and 2.5 % for maintenance).

T<sub>2</sub> weighted spin-echo scans were initially acquired (TR: 4000 ms, TE: 48 ms, FOV: 2 cm, matrix size 256 x 256, NEX: 6, slice thickness: 0.5mm, number of slices 15, coronal sectioning). T<sub>1</sub> weighted spin-echo scans prior to and 10 minutes after subcutaneous injection of 0.1 mL Omniscan contrast agent were then acquired (TR: 1000 ms, TE: 9 ms, FOV: 2 cm, matrix size: 256 x 256, NEX: 9, slice thickness: 0.5 mm, number of slices: 15, coronal sectioning).

### 3.2.3.3 Endpoints

Animals were sacrificed when their wellbeing was considered an issue (according to animal facility check-list), in this study all mice were sacrificed after the 2<sup>nd</sup> mouse had had to be euthanized. The first two mice to be sacrificed had developed tail necrosis, probably due to prolonged injection through the tail-vein.

Animals were sacrificed using a CO<sub>2</sub> gas inhalation system, and the brains of 4 of the mice were collected for histology.

### 3.2.3.4 Histology

In order to evaluate tumor burden for two representative animals (1 of each group) and to compare tumor burden after endpoint with BLI and MRI data, histological examination of two brains were carried out. The brains of the mice were harvested shortly exceeding time of death, and fixated in a solution of 2.5 % paraformaldehyde in PBS.

After fixation brains were dehydrated in 70 % EtOH, embedded in Gurr paraffin wax, and sliced in coronal orientation to a thickness of 5 µm slices, using a Leica RM2155 microtome, at 3 levels with 1 mm distance between, and placed upon microscopy slides.

Hematoxylin and Eosin (H&E) Staining:

The sections were treated in subsequent baths with xylene 2x4 minutes, 2x3 minutes in 100 % EtOH, 2x3 minutes in 96 % EtOH, 3minutes in 70 % EtOH, 3 minutes in distilled water, 45 seconds in Hematoxylin dye, 10 minutes in running tap water, 3minutes in 70 % EtOH,

3minutes in 96 % EtOH, 20 seconds in Eosin dye, dipped in 2x100 % EtOH baths, 2x5 minutes in xylene. After which cover slides were glued onto the stained samples.

H&E stained samples were imaged using the Leica DMLB and NIKON TE2000 light microscopes.

### 3.3 Software

**Inkscape™**v0.091, open-source vector graphics program, distributed by inkscape.org was used in assembling and labeling images into figures.

**ImageJ** v1.50b open-source image processing program, distributed by the National Institute for Health (Bethesda, Maryland, USA) was used to analyze time-lapse microscopy image series [76].

**ITK-SNAP** v3.4.0-rc1 open-source medical imaging analysis software, distributed by itknap.org, developed at University of Pennsylvania and University of Utah, USA, was used for viewing and analyzing MRI images.

**NIS-Elements** viewer v4.20.00 provided by NIKON (Tokyo, Japan) was used for microcopy image viewing, file-conversion, and adding scale-bars.

**GraphPad PRISM** v6.04 by GraphPad Inc. (San Diego, CA, USA) was used for making quantitative analyses and graphs thereof.

**NordicICE** v4.04 by NordicNeuroLab, Bergen, Norway, was used for DCE-MRI analysis, i.e. calculating A.U.C. and  $K_{trans}$  values.

**Excel 2013** by Microsoft® (Seattle, USA) as part of Office© suite was used for parts of data analyses.

**Word 2013** by Microsoft® (Seattle, USA) used as primary text editor.

**EndNote X7** by Thomson Reuters, was used for managing citations in this thesis.

## 4 Results

### 4.1 *In vitro*

#### 4.1.1 Vemurafenib cell culture experiments

##### 4.1.1.1 Cell Viability assay

Cell viability was assessed using a resazurin-resorfin viability assay, showing concentration dependent growth/proliferation inhibition of the H1\_DL2 melanoma derived cell line when treated with vemurafenib. Furthermore the  $IC_{50}$  values for H1\_DL2 cell line cells were on average an order of magnitude lower than for those of human fibroblast cell line SV80,  $6.47 \times 10^{-7}$  vs.  $1.74 \times 10^{-5}$  M vemurafenib (Figures 4.1 & 4.2).

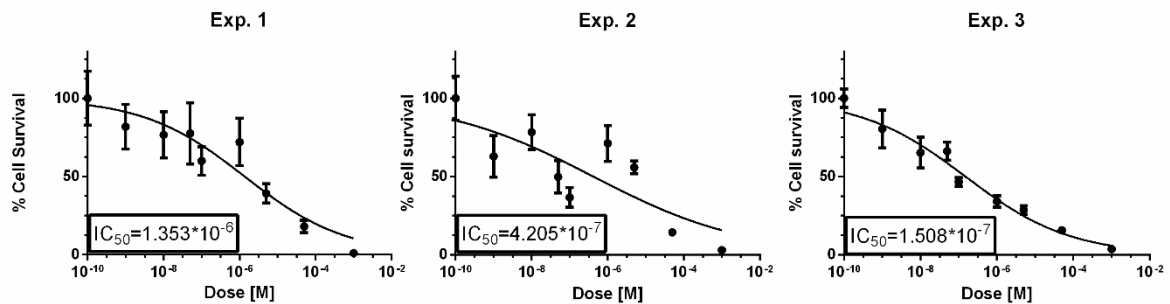


**Figure 4.1:** Cell Viability assay. Resazurin cell survival assay of H1\_DL2 melanoma cell line treated with varying concentrations of vemurafenib.

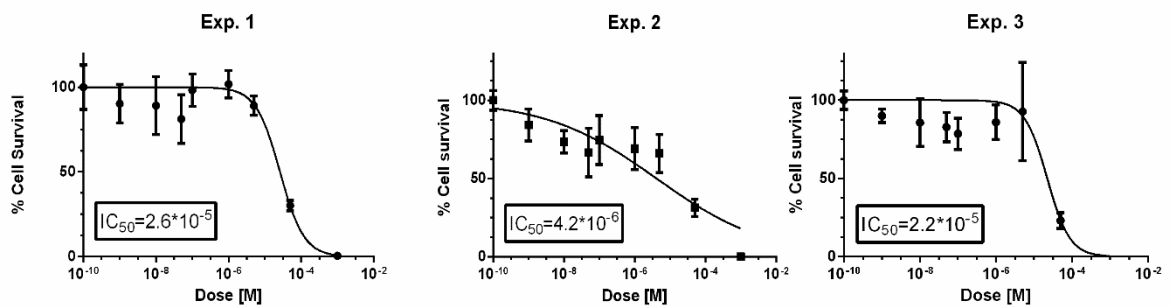


**Figure 4.2:** Cell viability assay SV80 human fibroblast (normal) cell line treated with varying concentrations of vemurafenib.

#### 4.1.1.2 Light microscopy

Conventional brightfield microscopy was performed on H1\_DL2 melanoma cell line cells treated with 50 $\mu$ M vemurafenib and untreated control cells, to assess morphological differences of cells treated with vemurafenib compared to untreated controls (Figure 4.3). The cells treated with vemurafenib showed visibly less growth, as also confirmed by resazurin-resorfin viability assay, as well as a more elongated spindle-like phenotype compared to the untreated controls. The effects of vemurafenib upon the cells were enduring (96 hours) showing inhibition of cell growth and proliferation.

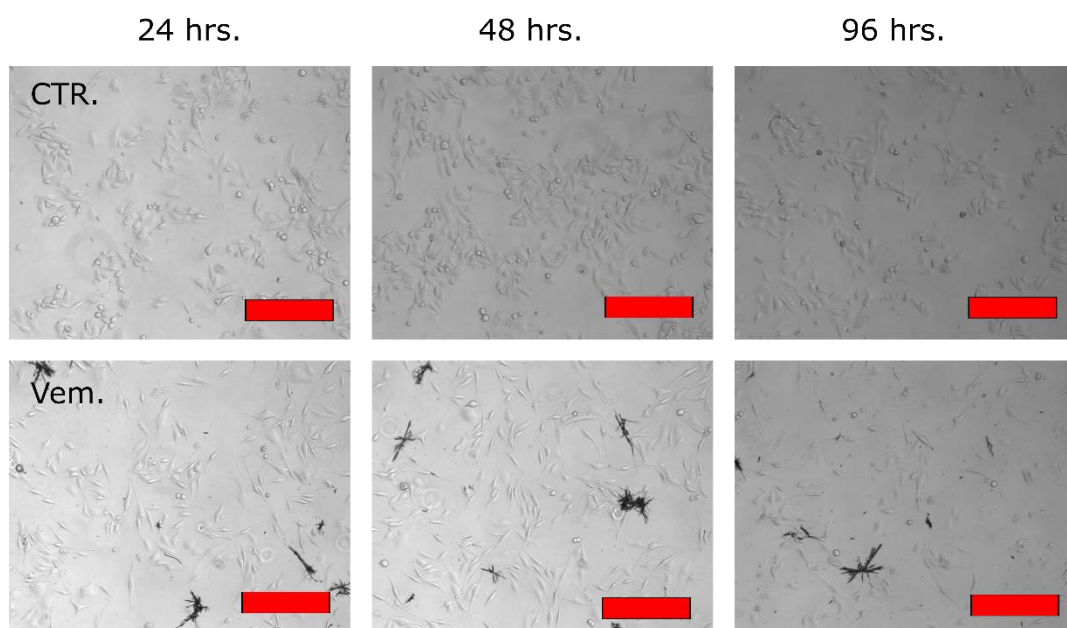


**Figure 4.3:** Cell morphology of H1\_DL2 cells treated with 50  $\mu$ M vemurafenib (bottom row) after 24 hours, 48 hours and 96 hours, compared to untreated cells (top row). A more spindly appearance was observed in the treated cells, as well as visibly fewer cells in each treated well. In images of cells treated with 50  $\mu$ M vemurafenib crystalline precipitations could be observed, which are vemurafenib precipitating in an aqueous solution. Microscopy images taken with Nikon TE2000, magnification X10. Scale bar = 125  $\mu$ m.

#### 4.1.2 K16ApoE cell culture experiments

##### 4.1.2.1 Survival assay

In order to assess the cytotoxicity of K16ApoE, resazurin-resorfin viability assays were performed on a selection of cell-lines, in which viability was measured after 45 minutes of incubation with the peptide.

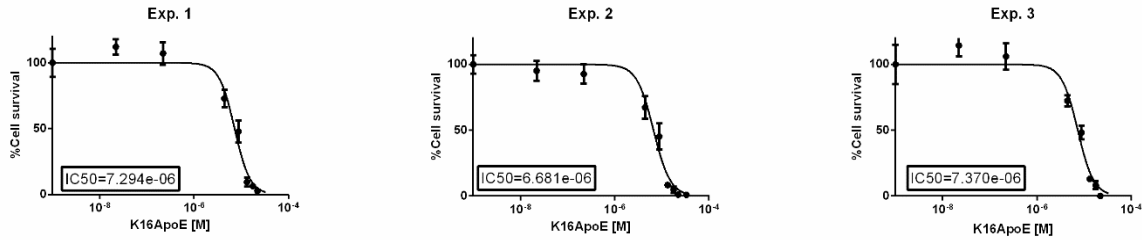


**Figure 4.4:** Relative survival of MDCKII canine kidney endothelial cell line treated with varying concentrations of K16ApoE (0.1 , 1 , 20 , 40 , 60 , 80 , 100 & 150  $\mu\text{g/ml}$ ) as determined by a resazurin viability assay. Concentrations in graph are in Molar.

MDCKII cells treated with K16ApoE showed a concentration dependent decrease in survival, with an averaged  $\text{IC}_{50}$  of  $7.115 \times 10^{-6} \text{M}$  K16ApoE (Figure 4.4). The peptide did not affect cell survival measurably at concentrations around  $4 \mu\text{M}$  or below.

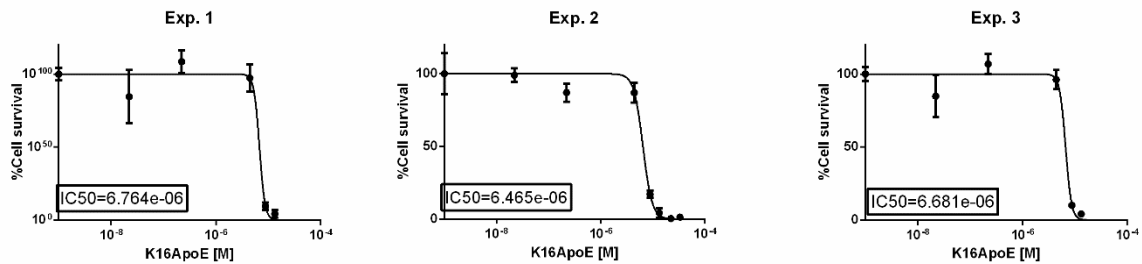


**Figure 4.5:** Relative survival of RBE4 rat brain endothelial cell line treated with varying concentrations of K16ApoE (0.1 , 1 , 20 , 40 , 60 , 80 , 100 & 150  $\mu\text{g/ml}$ ) as determined by a resazurin viability assay. Concentrations shown in Molar on graph.

RBE4 cells treated with K16ApoE showed a concentration dependent decrease in survival, with an averaged  $\text{IC}_{50}$  of  $6.637 \times 10^{-6} \text{M}$  K16ApoE (Figure 4.5). The peptide did not affect cell survival measurably at concentrations around  $4 \mu\text{M}$  or below.

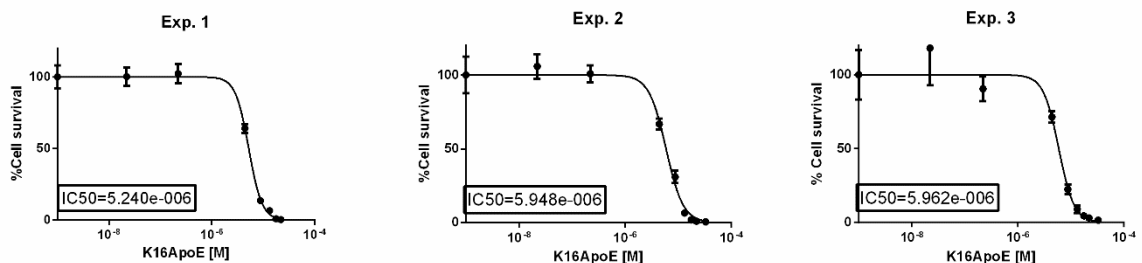


**Figure 4.6:** Relative survival of H1\_DL2 melanoma cell line treated with varying concentrations of K16ApoE (0.1 , 1 , 20 , 40 , 60 , 80 , 100 & 150  $\mu\text{g/ml}$ ) as determined by a resazurin viability assay. Concentrations in Molar on graph.

H1\_DL2 cells treated with K16ApoE showed a concentration dependent decrease in survival, with an averaged  $IC_{50}$  of  $5.714 \cdot 10^{-6} M$  K16ApoE (Figure 4.6). The peptide did not affect cell survival measurably at concentrations around  $4 \mu M$  or below.

In summary there were no obvious differences in cell viability between the three cell lines that were tested.

#### 4.1.2.2 Time-lapse Fluorescence Microscopy

The viability studies showed that K16ApoE doses of up to around  $4 \mu M$  did not affect cell viability. However, higher doses were shown to be toxic to the cells. Based on the previous viability studies, we picked peptide doses around the  $IC_{90}$  dose (80 and  $100 \mu g/mL$ ). In order to assess membrane stability, time-lapse fluorescent microscopy was performed on cells with cytoplasmic fluorophores, treated with K16ApoE (Figure 4.7).

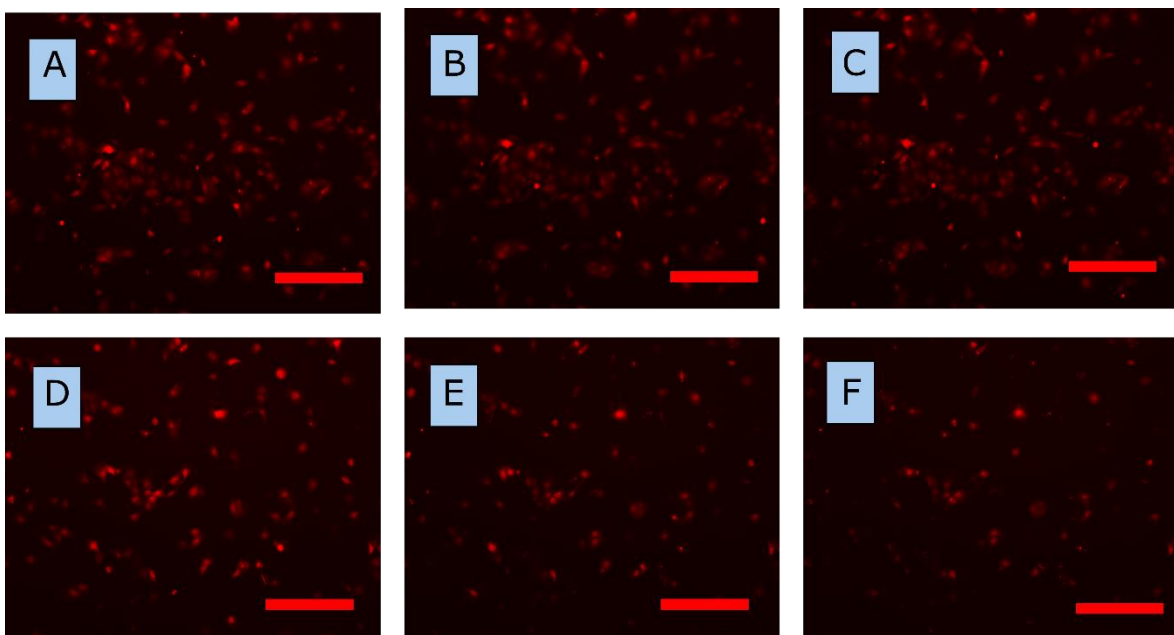


**Figure 4.7:** Frames from time-lapse microscopy of MDCKII transduced with mcherry and treated with K16ApoE. **A)** Untreated control cells 0 minutes. **B)** Untreated control cells 30 minutes. **C)** Untreated control cells 60 minutes, **D)** Cells treated with  $100 \mu g/mL$  K16ApoE 0 minutes. **E)** Cells treated with  $100 \mu g/mL$  K16ApoE 30 minutes. **F)** Cells treated with  $100 \mu g/mL$  K16ApoE 60 minutes. Images are taken in the red-channel, using the NIKON TE2000 microscope and the NIKON NIS elements acquisition software. Scale bar =  $250 \mu m$ .

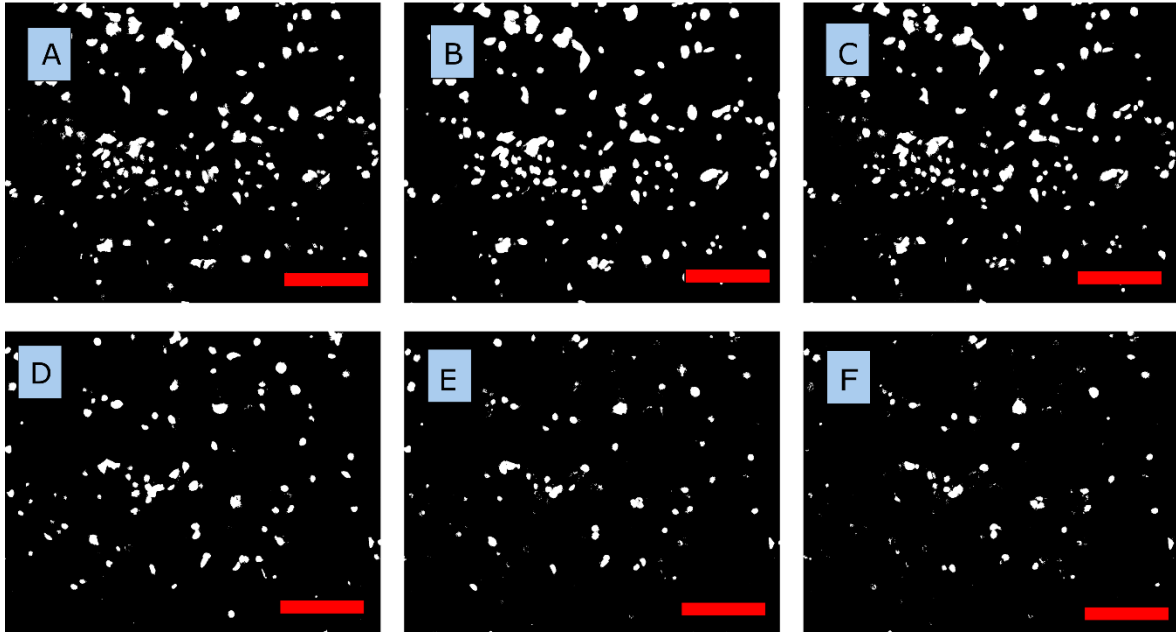


**Figure 4.8:** Binary images created from fluorescence timelapse acquisition images of MDCKII mcherry cells treated with K16ApoE. **A)** Untreated control cells at 0 minutes, **B)** Untreated control cells at 30 minutes, **C)** Untreated control cells at 60 minutes. **D)** Cells treated with 100 µg/mL K16ApoE at 0 minutes, **E)** Cells treated with 100 µg/mL K16ApoE at 30 minutes, **F)** Cells treated with 100 µg/mL K16ApoE at 60 minutes. Binary images created using Otsu's method, in ImageJ. Scale bar = 250 µm.

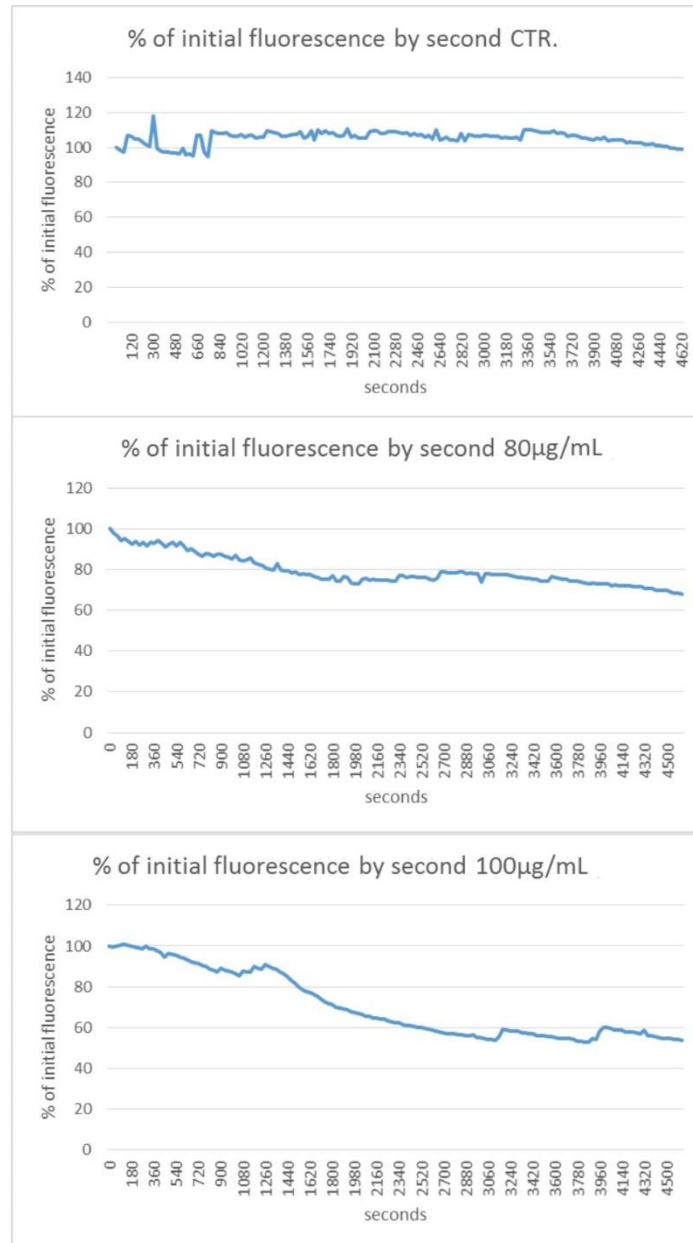


**Figure 4.9:** Time-lapse microscopy curves of mcherry intensity of MDCKII cells treated with varying concentrations of K16ApoE. Cells were either untreated (top curve) or treated with 80 µg/mL K16ApoE (middle curve) or 100 µg/mL K16ApoE (bottom curve). The curves show percentage of fluorescence relative to initial fluorescence (defined as 100 %). CTR denotes untreated controls. Microscopy was done on the NIKON TE2000 light, & fluorescence microscope. Change in fluorescence interpreted as area covered by fluorescing cells, the segmentation was done in ImageJ using Otsu’s method.

Time-lapse microscopy of MDCKII cells (Figures 4.7, 4.8 and 4.9) transduced with mcherry red fluorescent protein, and treated with K16ApoE, showed a decrease in fluorescence, compared to negative (untreated) control. The fluorescence intensity dropped to around 65 % after treatment with 80 µg/mL K16ApoE and to 55 % after treatment with 100 µg/mL K16ApoE. Control series remaining largely unchanged at the end of time-lapse relative to the beginning.

Time-lapse microscopy of H1\_DL2 cells, which are transduced with GFP, did not show clear changes in fluorescence when treated with 80 and 100  $\mu\text{g}/\text{mL}$ , relative to the negative controls (data not shown).

#### 4.1.2.3 Electron Microscopy

To assess detailed morphological differences and investigate cell-cell contacts at peptide concentrations around the  $\text{IC}_{90}$  doses, electron microscopy of epithelial cell lines treated with concentrations 20, 40, 80  $\mu\text{g}/\text{mL}$  relative to untreated controls of confluent cells in monolayer, was performed.

#### Scanning Electron Microscopy

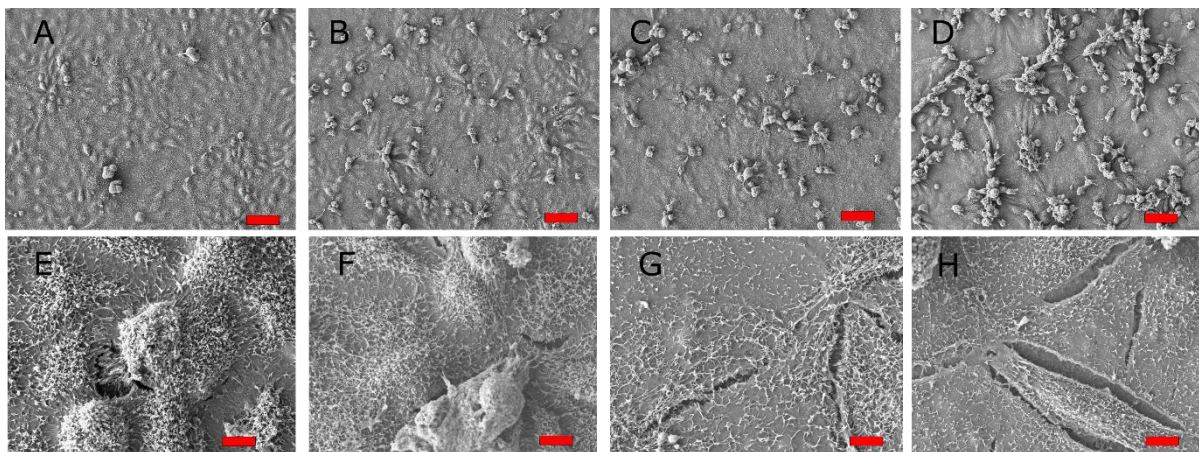


**Figure 4.10:** Scanning electron microscopy of MDCKII cell line monolayer cells treated with varying concentrations of K16ApoE. **A, E)** control series, **B, F)** 20 $\mu\text{g}/\text{mL}$  K16ApoE, **C, G)** 40 $\mu\text{g}/\text{mL}$  K16ApoE, **D, H)** 80 $\mu\text{g}/\text{mL}$  K16ApoE. A-D Scale bar = 30 $\mu\text{m}$ , E-H Scale bar = 4 $\mu\text{m}$ . Acquisitions were made using the Jeol JSM-7400F Scanning Electron Microscope.

MDCKII cells grown to confluence and treated with varying concentrations of K16ApoE (0, 20, 40, 80  $\mu\text{g}/\text{mL}$ ), showed a concentration dependent increase in aberrant and dying cells, dissociating from the monolayer. (Table 4.1 and Figure 4.10) The number of aberrant and dying cells were significantly higher in all treated groups ( $p < 3 \times 10^{-5}$ ). The difference in number of dying cells between those treated with 80  $\mu\text{g}/\text{mL}$  compared to those treated with 20  $\mu\text{g}/\text{mL}$  was significant ( $p < 0.05$ ), whilst the difference between 40 and 80  $\mu\text{g}/\text{mL}$  was not significant ( $p = 0.08$ ), nor was the difference between 20 and 40  $\mu\text{g}/\text{mL}$  significant at ( $p = 0.23$ ).

**Table 4.1:** Average number (from 5 parallels) of abnormal/ dying MDCKII cells visible in SEM images at 400X magnification, at different concentrations of K16ApoE treatment, relative to untreated control cells. SD=standard deviations. P-values <  $3.3 \cdot 10^{-5}$  all treated relative to control series. P-values: 80vs20  $\mu\text{g/ml}$ :  $p=0.016$ , 80vs40  $\mu\text{g/ml}$ :  $p=0.08$ , 40vs20  $\mu\text{g/ml}$ :  $p=0.23$ .

$\mu\text{g/mL}$	Average no.	
K16ApoE	Abnormal/Dying cells	SD
80	75	24,45
40	50	14,15
20	40	7,7
0	1	0,45

The differences in number of aberrant/dying cells quantified (Table 4.1, Figure 4.11) can readily be observed from SEM images of cells treated with varying concentrations (20, 40, 80  $\mu\text{g/mL}$ ) relative to untreated controls at magnification 400x (Figure 4.10: A-D). Differences in cell surfaces could clearly be seen on images of cells at 3000X magnification, with tears in the monolayer more apparent at higher concentrations of K16ApoE (Figure 4.10: E-H & Figure 4.11).

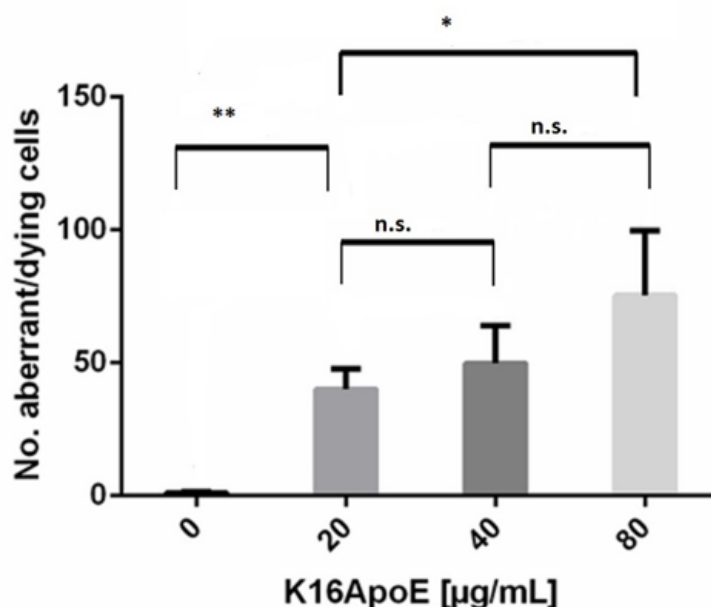


**Figure 4.11:** Number of aberrant and dying cells counted on SEM images of MDCKII cells treated with 0, 20, 40, 80  $\mu\text{g/mL}$  K16ApoE. p-values from two sided student t-test between concentrations. (\* =  $p < 0.05$ , \*\* =  $p < 0.01$ , n.s. = not significant.) Error bars show standard deviations.

## Transmission Electron Microscopy

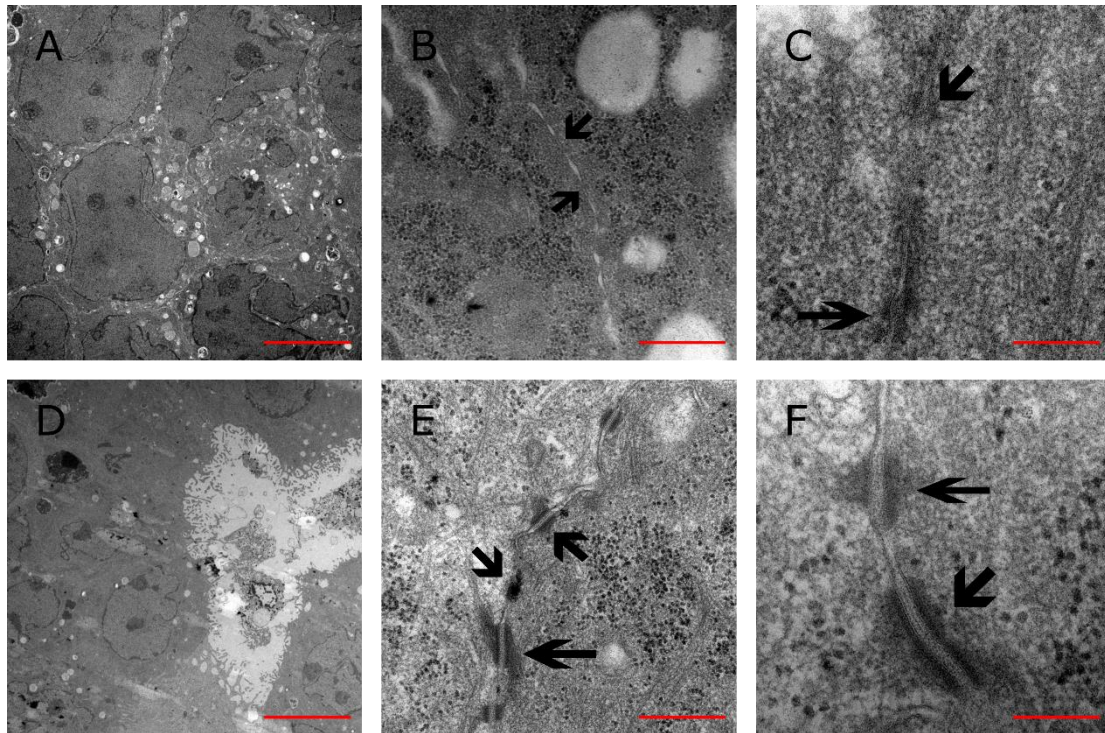


**Figure 4.12:** Transmission electron microscopy images of MDCKII cells treated with 0 and 80  $\mu\text{g/mL}$  K16ApoE for 45 minutes. **A)** Control cells, scalebar=7 $\mu\text{m}$ . **B)** Control cells, scalebar=500nm. **C)** Control cells, scalebar=200nm. **D)** Cells treated with 80  $\mu\text{g/mL}$  K16ApoE, scalebar=7 $\mu\text{m}$ . **E)** Cells treated with 80  $\mu\text{g/mL}$  K16ApoE, scalebar=500nm. **F)** Cells treated with 80  $\mu\text{g/mL}$  K16ApoE, scalebar=200nm. Arrows indicate cellular junctions, presumably desmosomes.

Transmission electron microscopy of MDCKII cells (Figure 4.12), showed no readily observable difference between controls or cells treated with the highest concentration (80  $\mu\text{g/mL}$ ) of K16ApoE. Cell-junctions were observable and intact for both treated and untreated cells at all concentrations (0-80  $\mu\text{g/mL}$ ).

## 4.2 In Vivo

### 4.2.1 K16ApoE Kinetics: DCE-MRI

DCE-MRI was performed on healthy NOD-SCID mice in order to independently verify previously published results [51, 52, 77, 78], and evaluate the duration of BBB opening in the model system. Gadodiamide (Omniscan®) having a MW of 573.66 did not cross over an intact BBB, and was therefore deemed effective in assessing BBB permeability to large molecules.

#### 4.2.1.1 K16ApoE effect on BBB 10 minutes post administration

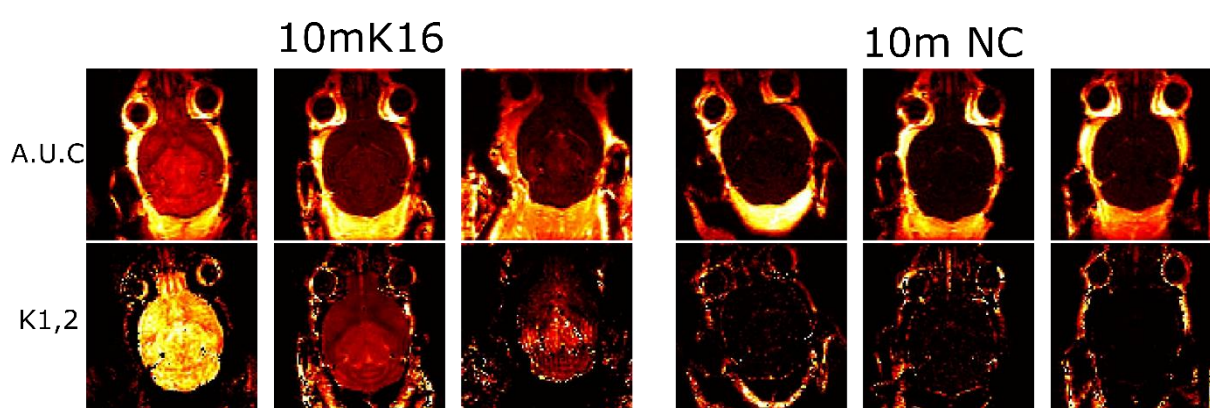


**Figure 4.13:** DCE-MRI 200 µg K16ApoE 10 minutes: Area under curve (AUC) and volume transfer coefficient  $K_{1,2}$  maps for mice treated with 200µg K16ApoE compared to negative controls (injected with saline). 10mK16=10 minutes post i.v. injection of K16ApoE, 10mNC=10 minutes post saline i.v. (Negative Control). Analyses performed with NordicIce v4.04.

DCE-MRI of animals performed 10 minutes after administration of 200 µg K16ApoE, showed an increased uptake of contrast fluid into the brain, relative to control animals given a saline infusion 10 minutes prior to DCE-MRI (Figure 4.13).

**Table 4.2:** Area under curve (AUC) and volume transfer coefficient ( $K_{1,2}$ ) values for animals injected with 200 µg K16ApoE 10 minutes post injection, and corresponding negative controls (NC). SD denotes standard deviations. Values from a region of interest encompassing most of the brain,  $A = 65.6 \pm 0.2 \text{ mm}^2$ .

K16ApoE				NC			
AUC	SD	K12	SD	AUC	SD	K12	SD
1680540	384321	0,07	0,025	202900	160057	0,008	0,02
3580780	599486	0,1384	0,0553	183117	164821	0,007	0,15
1098370	521996	0,096	0,089	173246	154263	0,019	0,035

Quantification of area under curve values and volume transfer coefficient  $K_{1,2}$  (Table 4.2) for a region of interest encompassing most of the brain, (area =  $65.6 \pm 0.2 \text{ mm}^2$ ), also confirmed this. P-values  $< 0.05$  for AUC relative to controls and  $K_{1,2}$  relative to controls.

#### 4.2.1.2 Evaluation of duration of BBB opening after injection of K16ApoE

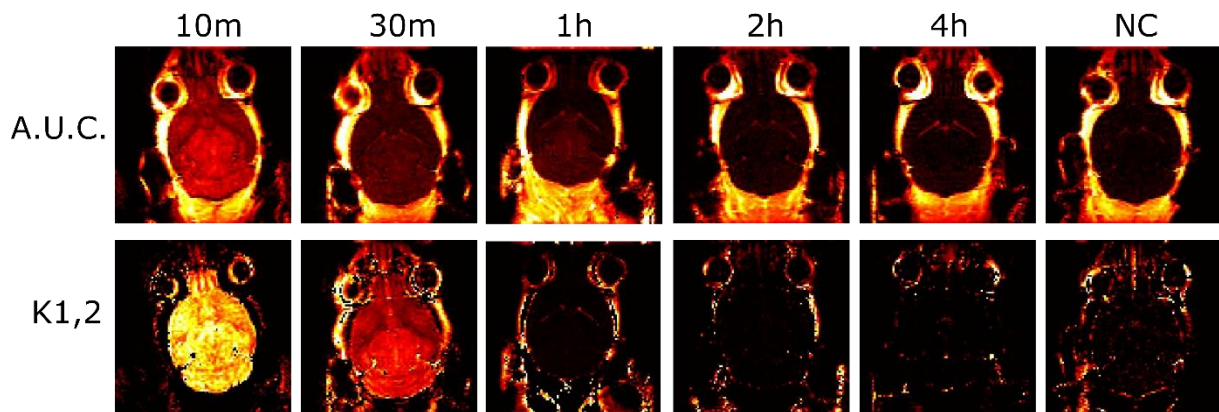


**Figure 4.14:** DCE-MRI 200  $\mu\text{g}$  K16ApoE 10 minutes – 4hours: Area under curve and volume transfer coefficient  $K_{1,2}$  maps for mice treated with 200  $\mu\text{g}$  of K16ApoE at time-points: 10 minutes, 30 minutes, 1 hour, 2 hours, 4 hours post i.v. injection. NC denotes negative control, shown for a mouse injected 10 minutes prior to DCE. Analyses performed with nordicIce v 4.04. Data for 1 hour K16ApoE from scans performed by; Olivier Keunen, Frits Thorsen and Heidi Espedal.

The uptake of contrast fluid decreased with time as can be seen from AUC and  $K_{1,2}$  maps of time-points 10 minutes – 4 hours post administration of K16ApoE (Figure 4.14).

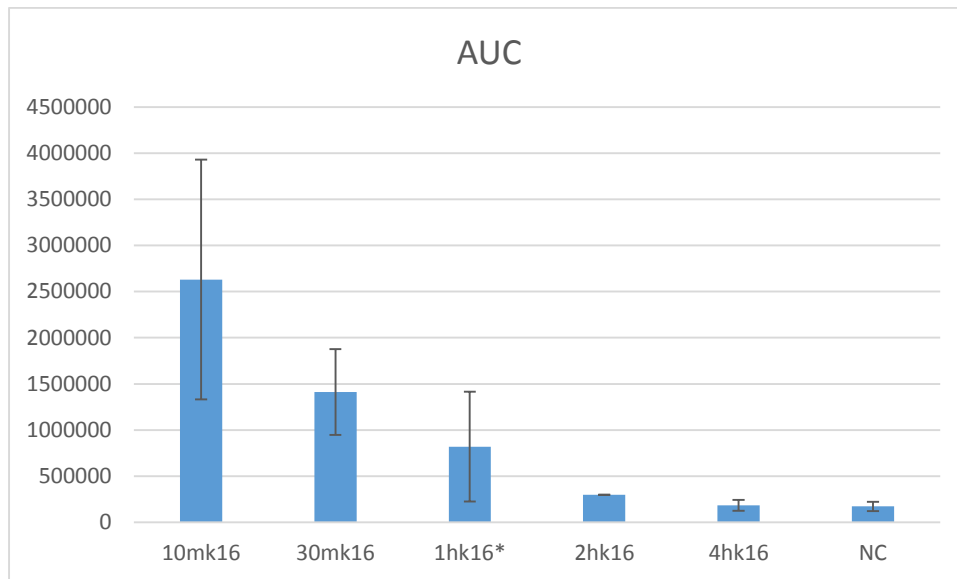


**Figure 4.15:** Area under curve (AUC) values for animals injected with 200  $\mu$ g K16ApoE, at varying time-points post injection; 10 minutes (10mk16), 30 minutes (30mk16), 1 hour (1hk16\*), 2 hours (2hk16), 4 hours (4hk16) and negative controls (NC).  $n = 3, 2, 4, 1, 5, 11$  respectively, error-bars show standard deviations. Values from a region of interest encompassing most of the brain, (area =  $65.6 \pm 0.2$  mm<sup>2</sup>). \*Data for 1 hour K16ApoE from scans performed by; Olivier Keunen, Frits Thorsen and Heidi Espedal.

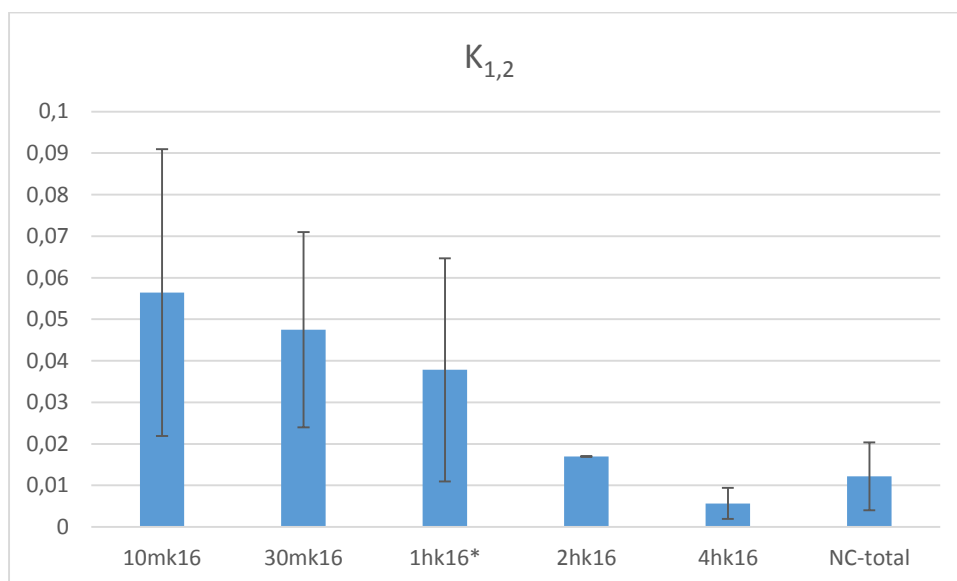


**Figure 4.16:**  $K_{1,2}$  (volume transfer coefficient) values for animals treated with 200  $\mu$ g K16ApoE at varying time-points post injection; 10 minutes (10mk16), 30 minutes (30mk16), 1 hour (1hk16\*), 2 hours (2hk16), 4 hours (4hk16) and negative controls (NC).  $n = 3, 2, 4, 1, 5, 11$  respectively, error-bars show standard deviations. Values from a region of interest encompassing most of the brain, (area =  $65.6 \pm 0.2$  mm<sup>2</sup>). \*Data for 1 hour K16ApoE from scans performed by; Olivier Keunen, Frits Thorsen and Heidi Espedal.

Negative controls were found not to be different, whether saline injection given at 10 minutes 4 hours, or any time-point in between, prior to scan, and thus combined to form a single group.

Quantification of AUC and  $K_{1,2}$  values (Figures 4.15 and 4.16) from a region of interest encompassing most of the brain, (area =  $65.6 \pm 0.2 \text{ mm}^2$ ) both showed a decrease towards baseline at 4 hours post administration. Differences in A.U.C values were significant to  $p < 0.05$  between (time after injection of K16ApoE): 10 minutes and controls, 10 minutes and 4 hours, 30 minutes and negative controls, 30 minutes and 4 hours, 1 hour and negative controls, 1 hour and 4 hours. Other p-values between A.U.C groups were: 10 minutes and 30 minutes;  $p = 0.53$ , 10 minutes and 1 hour;  $p = 0.13$ , 30 minutes and 1 hour;  $p = 0.29$ . Differences in  $K_{1,2}$  values were significant to  $p < 0.05$  between (time after injection of K16ApoE): 10 minutes and negative control, 10 minutes and 1 hour, 10 minutes and 4 hours, 30 minutes and negative control, 30 minutes and 4 hours, 1 hour and negative control, 1 hour and 4 hours. Other p-values between  $K_{1,2}$  values were: 10 minutes and 30 minutes;  $p = 0.12$ , 30 minutes and 1 hour;  $p = 0.66$ . P-values from two tailed student t-test. The 2 hour time-point, due to time-constraints, had only one animal, therefore a t-test could not be performed.

#### 4.2.1.3 Half-dose ( $100 \mu\text{g}$ K16ApoE) experiments

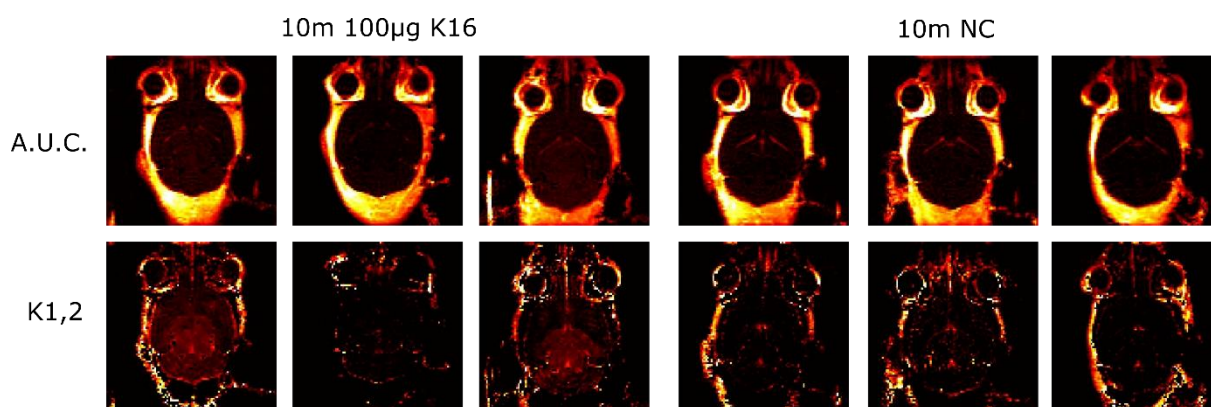


**Figure 4.17:** DCE-MRI  $100 \mu\text{g}$  K16ApoE 10 minutes: Area under curve and volume transfer coefficient  $K_{1,2}$  maps for mice treated with  $100 \mu\text{g}$  of K16ApoE 10 minutes post injection, compared to negative controls, mice injected with saline 10 minutes before DCE. Analyses performed with NordicIce v 4.04.

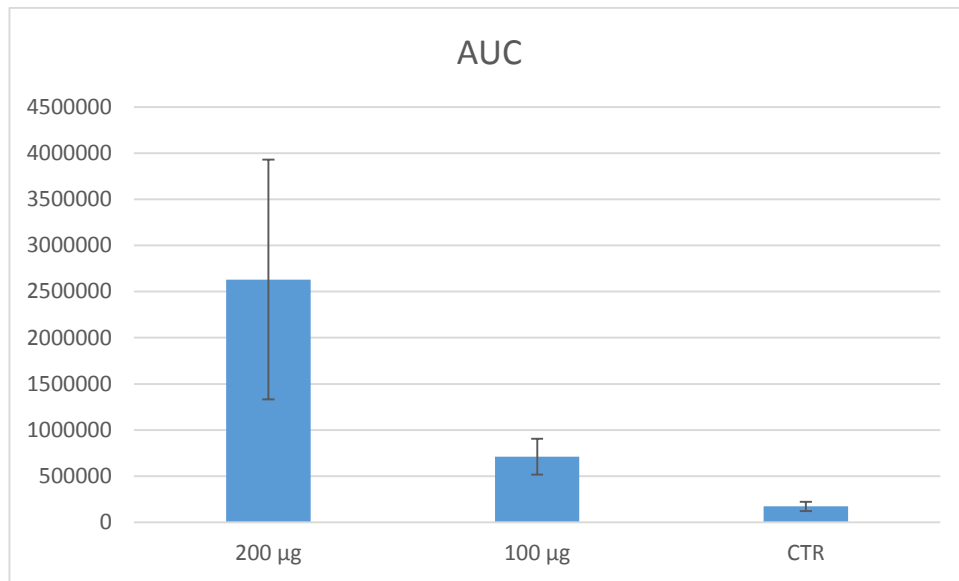


**Figure 4.18:** Area under curve values for 200 µg, 100 µg K16ApoE and control. AUC values from series 10 minutes after injection of peptide. Values from a region of interest encompassing most of the brain, (area =  $65.6 \pm 0.2 \text{ mm}^2$ ). Error bars show standard deviations. n=3, 3, 11 respectively.

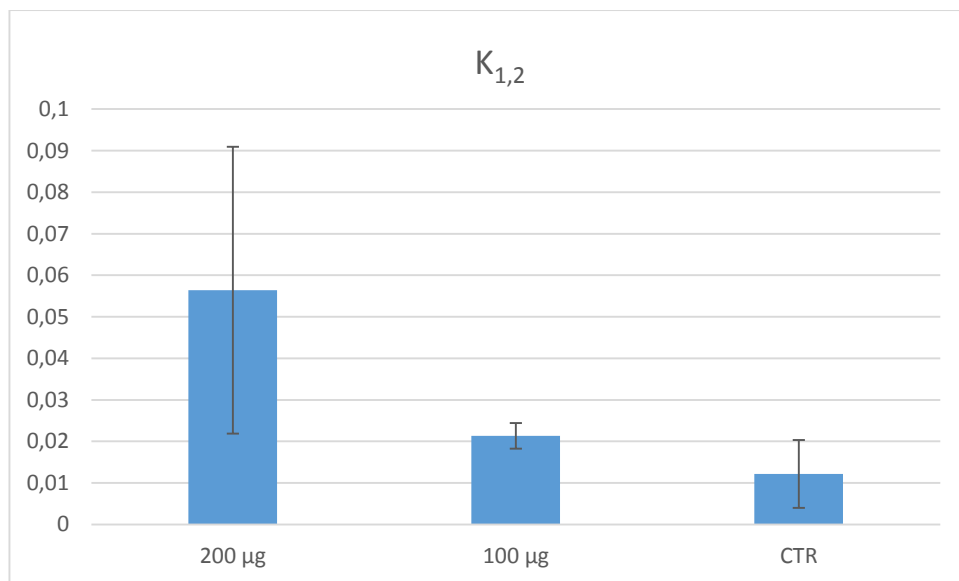


**Figure 4.19:** K<sub>1,2</sub> (volume transfer coefficient) values for 200 µg, 100 µg K16ApoE and control. K<sub>1,2</sub> values from series 10 minutes after injection of peptide. Values from a region of interest encompassing most of the brain, (area =  $65.6 \pm 0.2 \text{ mm}^2$ ). Error bars show standard deviations. n=3, 3, 11 respectively.

The average AUC value for animals administered 100 µg/ animal (AUC and K<sub>1,2</sub> maps seen in Figure 4.17) was 710880 with a standard deviation of 194597, and the K<sub>1,2</sub> value 0.021 with a standard deviation of 0.0031. A two tailed student t-test gave p-values of  $p < 2 \cdot 10^{-6}$  for AUC values relative to negative controls, and  $p = 0.12$  for K<sub>1,2</sub> values relative to negative controls. AUC and K<sub>1,2</sub> values of half-dose experiment negative controls, injections of 50 µL

saline 10 minutes prior to scan, were not significantly different from saline injections of 100  $\mu$ L 10 minutes prior to scan. P-values: 0.79 and 0.84 respectively.

Comparison between animals given 200  $\mu$ g of K16ApoE and those given 100  $\mu$ g K16ApoE (half-dose) for scans done 10 minutes after injections, showed halving the dose reduced average AUC values to 27 % of those for 200  $\mu$ g K16ApoE, and average  $K_{1,2}$  values to 38 % of those for 200  $\mu$ g K16ApoE (Figures 4.18 and 4.19).

#### 4.2.1.4 Intra peritoneal administration of K16ApoE

A scan was also done to evaluate IP administration of K16ApoE. A dose of 300  $\mu$ g of K16ApoE was administered intraperitoneally 30 minutes prior to DCE-MRI. AUC and  $K_{1,2}$  values were indistinguishable from negative controls (data not shown).

#### 4.2.2 Pilot Study: Combinatorial Treatment of xenografted melanoma with vemurafenib and K16ApoE

The pilot study was performed in order to assess the clinical relevance of K16ApoE to brain-metastatic melanoma. Vemurafenib which on its own is too large to bypass an intact BBB (MW 489.92 Da), was co-administered with the BBB-permeabilizing agent K16ApoE. This was done in order to determine if the combinatorial treatment approach could improve survival and affect tumor burden.

##### 4.2.2.1 Animal weight over time

Weight of the animals was measured continuously throughout the pilot, as an indicator of overall health-status.

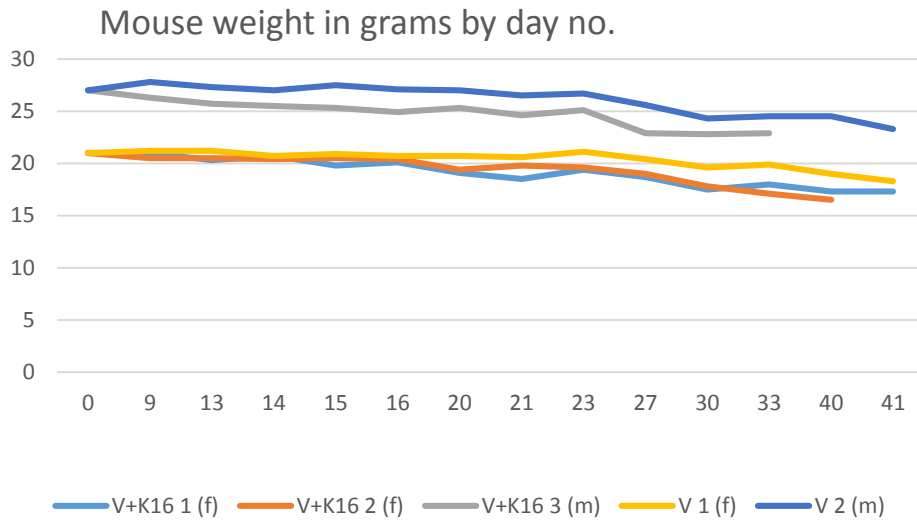


**Figure 4.20:** Weight of mice in pilot treatment study compared to days post intracardial injection of tumor cells. Treatment commenced at day 9 post intracardial injection. V+K16=vemurafenib+K16ApoE, V=vemurafenib alone.

The weights of the animals declined time, without showing any clear trend favoring either group, K16ApoE+vemurafenib or vemurafenib alone (Figure 4.20).

#### 4.2.2.2 BLI

BLI was performed to assess tumor burden of the animals at 4 weeks post-injection of tumor cells.

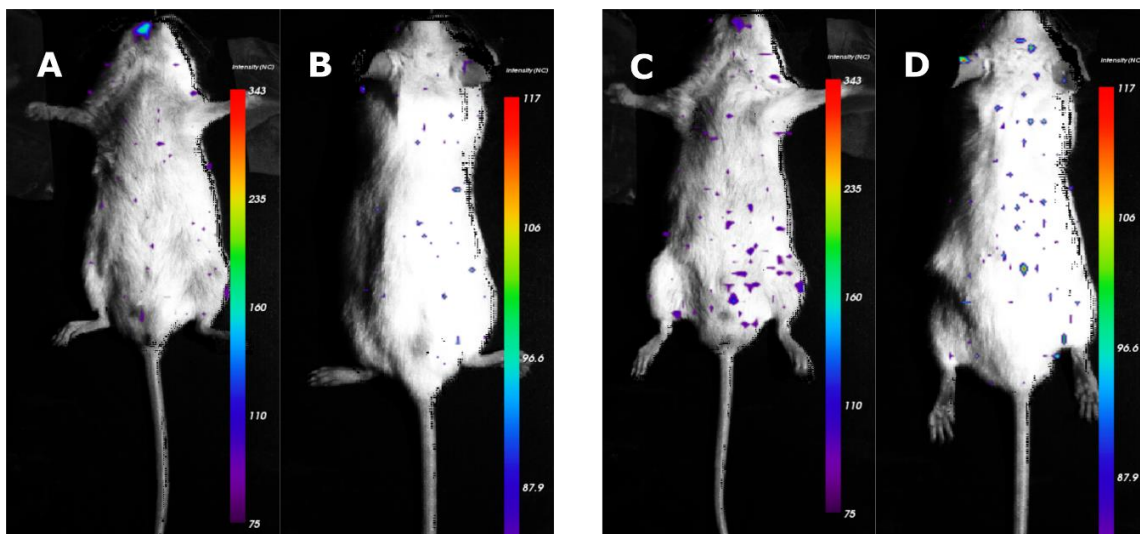


**Figure 4.21:** BLI images of two mice from the pilot study. **A)** Supine position of- mouse from the group treated with both K16ApoE and vemurafenib, **B)** prone position of- mouse from the group treated with both K16ApoE and vemurafenib. **C)** Supine position of- mouse from the group treated with only vemurafenib, **D)** prone position of- mouse from the group treated with only vemurafenib. Both of the animals were females.

There was a tendency that the BLI intensities were lower (or the same for supine brain) in the animals treated with both K16ApoE and vemurafenib, compared to those treated with vemurafenib alone. However the averaged BLI-values were not statistically significantly different from one another with all p-values>0.3 (supine body: p=0.3668, supine brain: p=0.9125, prone body: p=0.3625, prone brain: 0.4028) (Figures 4.21 & 4.22).

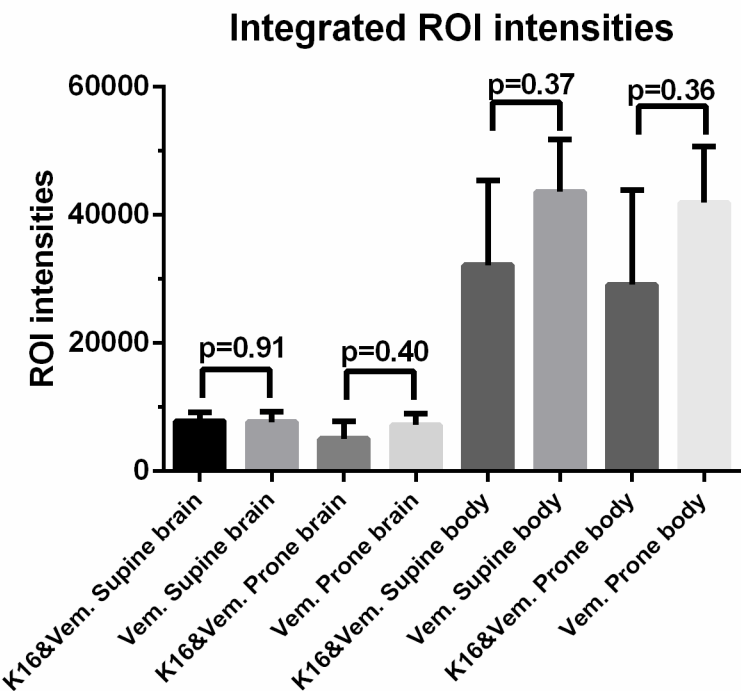


**Figure 4.22:** Integrated ROI intensities from BLI. K16&Vem.= the group treated with both K16ApoE and vemurafenib, Vem. = the group treated with only vemurafenib. p-values from two sided student t-test between the two groups shown. ROI areas ca 320 mm<sup>2</sup> for head and 1800 mm<sup>2</sup> for whole body.

### 4.2.2.3 Anatomical MRI

At week 5 post tumor-cell injection, anatomical MRI was performed to assess the number of brain-tumors and total tumor volumes for the animals. Three sequences were used: T<sub>1</sub>, T<sub>2</sub>, T<sub>1</sub> with contrast enhancement, contrast-enhancement here refers to contrast enhancement by subcutaneous injection of 0.1 mL of Omniscan® (Gd-diamide) contrast agent (Figure 4.23).

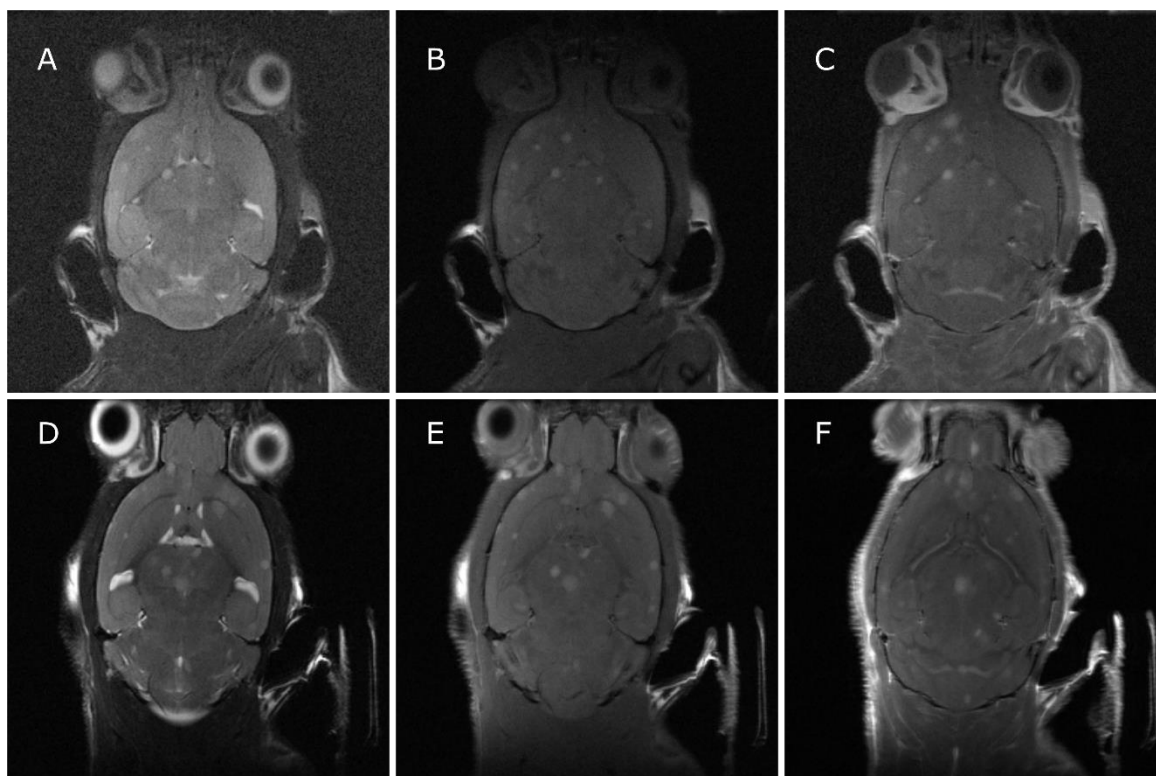


**Figure 4.23:** Anatomical MRI images taken at week five post injection of tumor cells. **A, B, C:** T<sub>1</sub>, T<sub>2</sub>, T<sub>1</sub> with contrast enhancement of female treated with both vemurafenib and k16ApoE. **D, E, F:** T<sub>1</sub>, T<sub>2</sub>, T<sub>1</sub> with contrast enhancement of female treated only with vemurafenib. Contrast enhancement refers to administration of 0.1ml subcutaneous Omniscan® contrast-fluid. Viewfield = 2 x 2 cm.

**Table 4.3:** Tumor count and estimated total tumor volumes from anatomical MRI images, mice treated with vemurafenib and K16ApoE are called “Vem.+K16”, mice treated with vemurafenib alone are called “Vem. only”. Treated and untreated groups are not significantly different, student t-test gives p-values: 0.293 for number of tumors 0.242 for tumor volumes. The analysis done in the ITK-SNAP Toolbox © segmentation software v3.4.

	TUMOR COUNT	TUMOR VOL. mm <sup>3</sup>
<b>Average Vem.+K16</b>	<b>71±13</b>	<b>2.17 ±0.22</b>
<b>Average Vem. Only</b>	<b>101.5±42</b>	<b>4.02±2.39</b>

In general, there was a trend towards reduced number of tumors as well as reduced total tumor volume after combined treatment with K16ApoE and vemurafenib. Mice treated with only vemurafenib had on average more tumors (number) and larger tumors than those that received vemurafenib and K16ApoE. (Table 4.3, Figures 4.23 and 4.24) The number of tumors in the vemurafenib only group were  $101 \pm 42$  tumors compared to the K16ApoE and vemurafenib group with  $71 \pm 13$  tumors. Total tumor volume in vemurafenib only group were on average  $4.02 \text{ mm}^3$  compared to  $2.17 \text{ mm}^3$  in the vemurafenib and K16ApoE group. However the differences were not statistically significant ( $p=0.293$  for the number of tumors and  $p=0.242$  for tumor volumes).

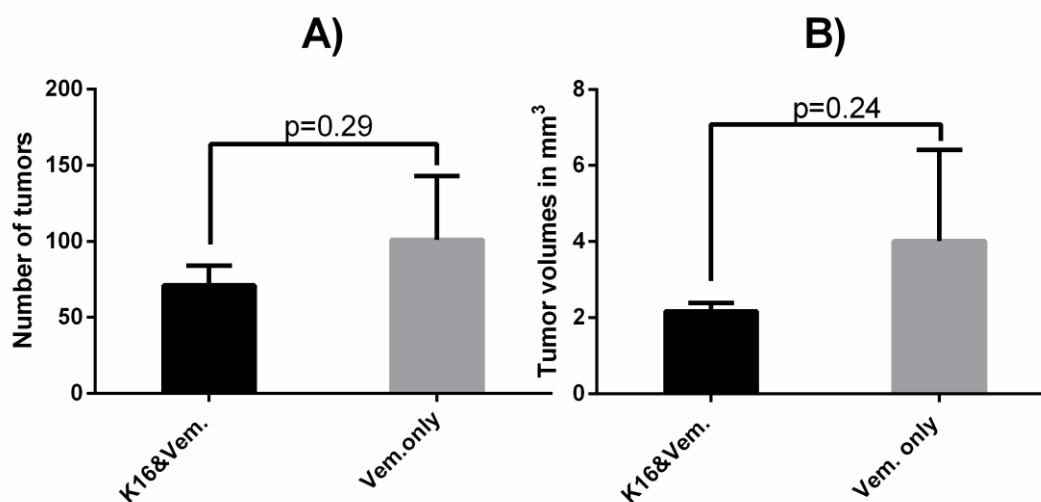


**Figure 4.24:** Tumor count and volumes averaged for group treated with both K16ApoE and vemurafenib (K16&Vem.) and the group treated with only vemurafenib (Vem. only). **A)** Average total number of intracranial tumors. **B)** Average total tumor-volume of observed tumors. p-values from two sided student t-test shown.

#### 4.2.2.4 Histology

To assess tumor burden after endpoint, and to compare to anatomical MRI data taken previously, histological slides were made for two of the animals' brains.

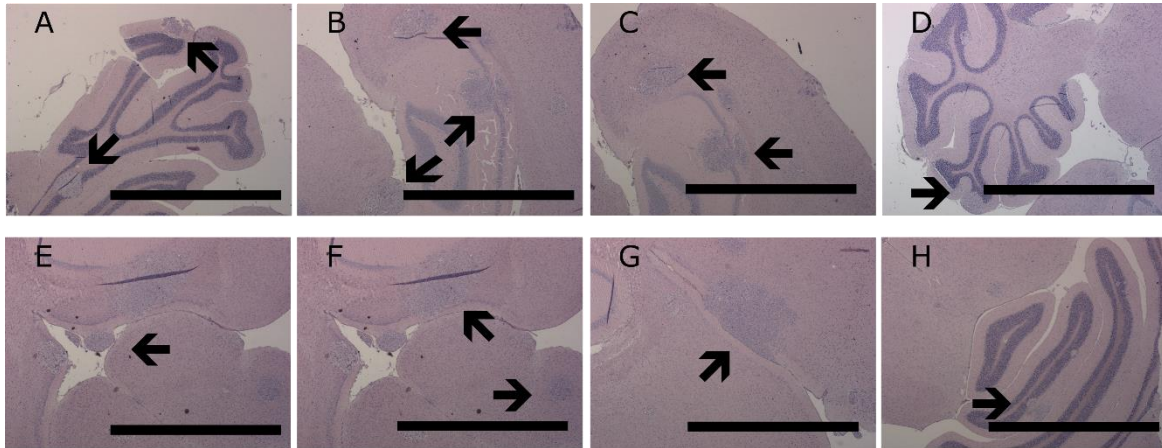


**Figure 4.25:** Tumors identified in histological slides, H&E stained 5  $\mu\text{m}$  thick slices of two mouse brains from pilot experiment, **A-D** are from a mouse treated with both vemurafenib and K16ApoE, **E-H** are from a mouse treated only with vemurafenib. Arrows indicate tumors. Images taken with the Leica DMLB microscope. Scalebar=2500 $\mu\text{m}$ .

As was seen in MRI data (Figure 4.21), tumors were readily observable in histological slides of the brains of the mice (Figures 4.25 and 4.26); done on one from each group. Tumors were both large and small, as well as numerous in both mice, with some being of a size likely below MRI detection limits. Visual inspection of slides indicates somewhat greater tumor-burden for the mouse treated with only vemurafenib, compared to the one treated with both K16ApoE and vemurafenib.

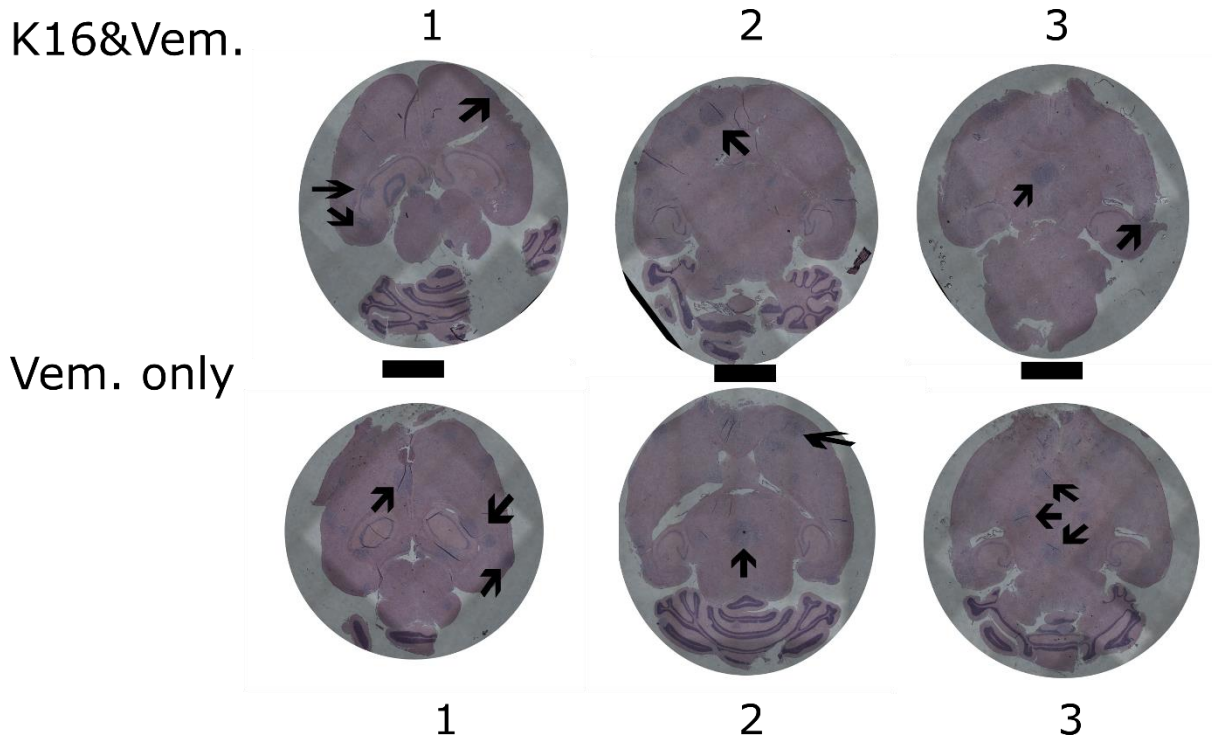


**Figure 4.26:** Histological sections of the brains of mice from pilot study, of one mouse from the group treated with K16ApoE and Vemurafenib (**K16&Vem.**) and one from the group treated with only Vemurafenib (**Vem. only**), both female mice. Arrows indicate tumors, (there are more tumors than indicated with arrows). Brains were sectioned 5  $\mu$ m thick, at three depths, 1 mm apart, slice level is indicated by numbers 1-3. Images taken using large image acquisition mode on the NIKON TE2000 microscope and NIS Elements acquisition software, images cropped and rotated in GNU Image Manipulation Program (GIMP) v2.8. Scale bars = 2.5 mm.

## 5 Discussion

Brain metastasis is a common and serious complication arising in up to 40 % of cancer patients [31]. The most common causes of brain metastasis are: lung cancer (50 %), breast cancer (20 %), melanoma (10 %) and colon cancer (5 %). As of today there are few treatment options, besides surgery, chemotherapy and radiotherapy [32]. Even improved treatment regimens such as those including stereotactic radiosurgery (SRS) only briefly extend survival. The prognosis of patients diagnosed with brain metastasis is extremely poor, with mean survival under treatment at only 9-10 months, despite extensive treatment [31].

Malignant melanomas, have commonly been treated with systemic chemotherapy in addition to surgery, but this has been of limited success [11]. Novel treatments have arisen in recent years, with targeting of signaling kinases with specifically tailored inhibitors (e.g. vemurafenib) [21], or using monoclonal antibodies [24, 25], for immune response mediated action (e.g. Ipilimumab, Pembrolizumab and Nivolumab) [26].

A major problem in treating brain metastases with chemotherapy is that for early stages and small tumors the blood brain barrier (BBB) remains closed, effectively protecting the tumors from many chemotherapeutic agents [33]. An intact BBB is largely impermeable to large and hydrophilic molecules greatly limiting which chemotherapeutics can be used in early brain metastatic development [40]. The problem of the intact BBB excluding treatments has been a field of interest for quite some time, and several strategies to disrupt or circumvent the BBB have been explored. The use of focused ultrasound guided by MRI for localized BBB permeabilization has shown promise and is currently under clinical safety evaluation [45, 79, 80]. Hypertonic solutions (e.g. urea, arabinose, mannitol, etc.) have been shown to induce cell shrinkage at the BBB, allowing penetration of compounds normally too large to cross into the brain parenchyma [49]. Certain solvents such as DMSO, ethanol and glycerol have also been shown to permeabilize the BBB, though when used at very high doses [43].

The existence of so few viable strategies lead to the development of a peptide at the center of this study, using the receptor binding domain of ApolipoproteinE with a 16 Lysine tail, and a BBB permeabilizing construct was thus made made [52]. K16ApoE was shown to affect the BBB in rats when co-administered with Evans blue dye, which normally does not cross the intact BBB. A significant increase in uptake of Evans blue was demonstrated, and this novel peptide showed promise in getting chemotherapeutics into the brain [51].

The aim of my thesis was thus to elucidate more on the biology of this newly developed peptide. My study was intended to examine by MRI if K16ApoE was capable of opening the BBB also in mice, how early this effect could be detected after administration and how long the BBB remained open. By using DCE-MRI, we were able to show that the BBB was permeabilized from 10 minutes up to at least 2 hours after intravenous administration of K16ApoE in mice. These results are promising as to allow for penetrance of therapeutics which would normally not enter the brain parenchyma (or only enter on a limited scale), and thereby increasing treatment efficacy of these drugs.

Prior to performing a pilot study of combined treatment with K16ApoE and vemurafenib (a drug targeting BRAF<sup>V600E</sup> mutated melanoma) *in vivo*, we needed to establish whether vemurafenib also was effective in treating human melanoma brain metastasis cell lines.

This was first studied in cell culture. Vemurafenib decreased cell-survival in a concentration dependent manner, with IC<sub>50</sub> far lower in BRAF<sup>V600E</sup> mutated melanoma cells, compared to wild type cells.

Vemurafenib has previously been shown to preferentially act upon BRAF mutated melanoma cells with the V600E mutation and also the V600K mutation. These mutations are activating mutations of the BRAF kinase, promoting growth and proliferation via the MAPK/ERK pathway [21]. This treatment effect is achieved by the design of this enzyme inhibitor, which gives it a higher degree of complementarity towards the V600E mutated kinase [81]. The prevalence of this mutation is high in melanomas, while also occurring in other cancers [82]. Thus vemurafenib is, as intended, a valid therapeutic agent for the treatment of metastatic melanoma. Our study also showed that the drug was effective in treating melanoma brain metastatic cells.

The light microscopy study of H1\_DL2 melanoma brain metastasis cells treated with vemurafenib showed a change in phenotype and decreased growth relative to untreated controls.

Cells treated with vemurafenib exhibited growth inhibition but little cell death, and not a complete inhibition of growth, meaning that vemurafenib only inhibited tumor cell development temporarily and incompletely. Previous clinical studies have shown that after an

initial treatment response melanomas develop resistance, by activating MAPK/ERK downstream of BRAF. The development of resistance thus limits the efficacy of vemurafenib. In the clinic combined treatment and specialized dosing regimens are used to try to forestall and avoid resistance [23]. Observations done in this study seem to coincide with what was already reported in the literature.

We next wanted to elucidate on the mechanisms of action of the peptide on endothelial cells, which are the first cells that circulating K16ApoE will meet in the bloodstream. Doses of up to around 4  $\mu$ M did not show reduced cell viabilities. The results showed that higher doses of peptide exerted its effect by direct cell cytotoxicity.

The high unspecific cytotoxicity of the peptide, demonstrated that caution has to be taken in a clinical setting, in order to avoid permanent damage to endothelial cells with subsequent organ damage.

It should be noted that viability assays such as the one used in this study do not directly measure cytotoxicity. Viability assays measure cell-viability, i.e. cell cycle or cell growth arrest would influence such an assay [83].

The group of Professor Catharina Davies at NTNU also concurrently working on K16ApoE, found that cells die at comparable doses as those in this study. Cell culture studies done by PhD student Synnøve Nymark Aasen in our lab, using the live-dead staining kit, also confirmed cytotoxicity in this concentration range. Of note is that in the *in vitro* experiments in this study, cells were kept in high doses of K16ApoE for prolonged periods of time (45 minutes and longer), which does not compare to the *in vivo* setting where the peptide will rapidly wash out of the system, in a matter of minutes. The *in vivo* situation might thus be better understood as a transient high dose. It is therefore likely that the cytotoxicity seen in the cell culture experiments would be largely diminished. A subacute toxicity study done by Sarkar et al. did not show any lasting effects in the animals, with histopathological examination not showing any organ damages [78].

Time-lapse fluorescence microscopy showed decrease in cytoplasmic fluorescence in cells treated with K16ApoE, indicating cell membrane disruption.

Time-lapse demonstrated that the cell membranes were damaged by the peptide at high concentrations, with leakage of internal components from the cells. The peptide is here indicated to act in a lytic fashion, rapidly killing cells through what may be induced membrane damage.

The peptide K16ApoE was designed to constitute the LDL-receptor binding domain of ApolipoproteinE [52], suggesting that the mode of action takes place at the cellular membrane. The peptide is basic, with a charge of 24 (calculated). The cell membranes are negatively charged, which may allow for this peptide to more readily attach to these, and inducing a lytic effect. Lower concentrations of the peptide are however expected to induce receptor-mediated endocytosis, with far less lysis. Unpublished results from Davies group at NTNU, have shown clathrin mediated cellular uptake by flow cytometry.

Whether K16ApoE only acts on the LDLR, or can bind to other targets is not currently known. The mode of action *in vivo* was found to coincide with higher tissue expression levels of the LDLR, which was taken as evidence of K16ApoE acting via the LDLR [52]. The specificity of the design suggests that a LDLR mediated mechanism may somehow be involved in the cytotoxicity of the peptide. The time-lapse experiment showed membrane leakage almost immediately, suggesting rapid onset of this (membrane disruptive) effect, and further suggesting this might also be the case *in vivo*, where there is a transient high dose of the peptide which is washed out rapidly compared to the *in vitro* experiments.

Scanning electron microscopy showed damaged and dying cells and disruption of a confluent monolayer of cells treated with high doses of K16ApoE.

The cytotoxicity of K16ApoE was confirmed again by SEM, strongly suggesting that K16ApoE BBB permeabilization at high doses is of a cytotoxic nature. This implies that damages to the otherwise confluent monolayer of brain vasculature endothelium, is a large part of the BBB permeabilizing effect of K16ApoE. The disruptive effect on a confluent cell monolayer was also found by Catharina Davies group at NTNU, who concluded that this leads to increased transport over the endothelial cell barrier (unpublished results). Given such a mode of action, finding ways to limit the dose, and exposure of unrelated organs to K16ApoE may be prudent. More localized administration and possibly targeted delivery via for example focused ultrasound and microbubbles [47] could be a possibility, which has already been proposed for harm reduction in chemotherapeutic agent delivery. The cells in the

*in vitro* experiments were kept for prolonged periods in solutions containing high doses of K16ApoE, which may not accurately describe the effects *in vivo*, where the peptide would also continuously be washed out.

Transmission electron microscopy showed no disruption of cell-cell junctions in cells treated with K16ApoE relative to untreated controls.

K16ApoE does not act on cell-cell adhesion molecules, altogether eliminating one possible mechanism of action. The cells did not lose adherence until dying, and cell-cell junctions remained intact. This is consistent with what was found by the group of Catherina Davies at NTNU, where apart from dead cells dissociating from the intact monolayers, the monolayers remained unchanged (unpublished results). The remaining candidates for mode of action are thus: cytotoxicity, wherein dying cells leave openings in a cell monolayer, such as the BBB, and receptor mediated endocytosis, for which there has been found some evidence by Catharina Davies et al. (clathrin mediated endocytosis was observed *in vitro*).

DCE-MRI of mice after intravenous administration of 200 µg K16ApoE showed opening of BBB already 10 minutes after injection. The administered dose in the animals was initially high, approximately 100-125 µg/mL peptide in the total blood volume (estimated to be around 1.5-2 mL in a mouse). However similar types of peptides have been noted to wash out rapidly *in vivo* (in mice) over the course of minutes [84]. The previously noted wash-out effect was likely also the case in our study, thought to quickly diminish the blood concentration of K16ApoE limiting the cytotoxic effects observed in the cell culture studies on high doses.

As found by Sarkar et al. [52, 77, 78, 85] K16ApoE opens the BBB, when given as a slow infusion at a dose of 200 µg per animal. Quantification of signal change in DCE-MRI confirmed what Sarkar et al. showed with Evans Blue Dye in mice, as well as various chemotherapeutic compounds [51, 78], that comparably large molecules can cross over the BBB if given in concert with K16ApoE.

DCE-MRI of mice treated with 200 µg K16ApoE showed a decrease in the degree of BBB permeabilization over time, with mice at 4 hours after injection of K16ApoE being indiscernible from control animals.

The BBB rapidly regenerated after injections of K16ApoE, as also found by Sarkar and colleagues [51], indicating K16ApoE may be given continuously for extended periods of time, without permanent damages to the BBB. Neither Sarkar et al. or our group noticed any impairment to animals given repeated administrations of K16ApoE. Subacute toxicity studies done by previously did not show damaging effects on mice given repeated doses of K16ApoE [78]. The regeneration of the BBB after injections of K16ApoE, even in mice that have previously been given the peptide, shows promise in that the peptide may be safely applied clinically. The regeneration of the BBB also places a time limit on co-administration of therapeutics, after 4 hours the BBB in mice did recover completely and large compounds can therefore no longer gain access to the brain parenchyma after this time point.

Due to the cytotoxic effect of high doses of K16ApoE observed *in vitro*, we wanted to see if lowered doses of K16ApoE could open the BBB as effectively. DCE-MRI of mice treated with 100 µg K16ApoE also showed opening of BBB 10 minutes after injection of K16ApoE.

The opening of the BBB by a dose of 100 µg per animal coincides with the findings of Sarkar and colleagues [51] who also noted a visible but decreased opening of the BBB. This shows that K16ApoE still mediates its effect on the BBB at this dosage, and the amount of contrast agent crossing over the BBB seemed to be reduced approximately by  $\frac{3}{4}$ . Being able to elicit an effect with a lower dose is of particular interest, given the non-specific and high toxicity of K16ApoE, yet a sufficient opening of the BBB would likely be achieved with a reduced dose. Taken into a clinical setting, cancer patients not tolerating the effects of K16ApoE well, or of initially poor health may thus still derive some benefit from the peptide when combined with chemotherapeutic drugs. This is particularly relevant as many cancer patients are elderly, and often in poor condition [86, 87].

The pilot treatment study showed lower BLI intensities (at week 4) for, and a decrease in tumor size and total tumor volume measured by anatomical MRI (at week 5) for animals treated with both K16ApoE and vemurafenib relative to animals treated with only vemurafenib, although the differences were not statistically significant.

Mice were treated from day 9 to week 5 after tumor cell injections. This time period is likely long enough for some of the tumors to develop treatment resistance [23]. The larger tumors

observed by MRI at week 5 also likely have a disrupted BBB, similar to what has been observed in previous studies [33]. Thus these tumors are not necessarily receiving a larger dose of drug due to opening of the BBB by the peptide, since the barrier is likely disrupted already. K16ApoE had previously been used in a treatment study of neurodegenerative lysosomal storage disease in a mouse model [78] where a therapeutic enzyme was delivered successfully over the BBB, and a treatment effect was observed. Also several other compounds have been found to move across the BBB after using the peptide [51, 52, 77]. Thus the results of our study suggest that K16ApoE can be applied to brain metastatic tumors, to open the BBB prior to administration of chemotherapeutic drugs which otherwise are not able to penetrate into the brain tissue. Based on the properties of the peptide, as described in our study there is reason to believe, that vemurafenib may cross over the BBB as our pilot study (with few animals) indicated a treatment effect when combining vemurafenib with the peptide. The dismal prognoses of brain metastatic cancer, and the current inability to treat early stages of brain metastases effectively [32], would make this strategy a welcome addition to therapeutic regimens.

#### Future perspectives

In parallel with this study, other *in vitro* experiments are currently being performed at NTNU in Trondheim, at the group of Catharina Davies, to elucidate more about the cellular mechanisms of K16ApoE (confocal studies to show membrane transport of K16ApoE). These studies are expected to elucidate more on the membrane action of K16ApoE.

An *in vivo* bio-distribution study in mice tagging K16ApoE with  $^{125}\text{I}$ , to elucidate more on the organ uptake of K16ApoE, is being planned. This would also enable us to evaluate organ toxicity and if K16ApoE accumulates noticeably in certain organs. These experiments would serve as comparison to what Sarkar and colleagues have done, i.e. subacute toxicity studies, in which they found nothing of notice.

Under work is a full-scale treatment study, wherein brain metastases are to be treated by combinatorial administration of K16ApoE and a chemotherapeutic agent, likely either vemurafenib or PLX4720, which is another BRAF inhibitor. Subsequent studies may also apply K16ApoE to the treatment of other brain metastatic cancers, such as lung, or breast cancer which commonly metastasize to the brain.

Depending on successes in full scale treatment studies, and preclinical safety evaluations, in time K16ApoE may move forward to clinical safety studies, and clinical studies. As of yet the peptide has only been evaluated in preclinical studies. K16ApoE is therefore still somewhat removed from clinical applications. The risk inherent in using K16ApoE, may conceivably lead it to only being applicable in terminal cases, which brain cancers often are.

## References

1. Diepgen, T.L. and V. Mahler, *The epidemiology of skin cancer*. Br J Dermatol, 2002. **146 Suppl 61**: p. 1-6.
2. Garbe, C., et al., *Diagnosis and treatment of melanoma. European consensus-based interdisciplinary guideline--Update 2012*. Eur J Cancer, 2012. **48**(15): p. 2375-90.
3. Kumar, V., et al., *Robbins basic pathology*. 9th ed. 2013, Philadelphia, PA: Elsevier/Saunders. xii, 910 p.
4. Institute, N.C. 2008; Available from: <http://www.cancer.gov/Common/PopUps/popDefinition.aspx?id=46292&version=Patient&language=English>.
5. Dunki-Jacobs, E.M., G.G. Callender, and K.M. McMasters, *Current management of melanoma*. Curr Probl Surg, 2013. **50**(8): p. 351-82.
6. Magro, C.M., A.N. Crowson, and M.C. Mihm, *Unusual variants of malignant melanoma*. Modern pathology : an official journal of the United States and Canadian Academy of Pathology, Inc, 2006. **19 Suppl 2**: p. S41-70.
7. Hikawa, R.S., et al., *Polypoid melanoma and superficial spreading melanoma different subtypes in the same lesion*. An Bras Dermatol, 2014. **89**(4): p. 666-8.
8. Institute, N.C. *SEER Stat Fact Sheets: Melanoma of the skin*. Available from: <http://seer.cancer.gov/statfacts/html/melan.html>.
9. Stewart, B.W., et al., *World cancer report 2014*. 2014, Lyon, France Geneva, Switzerland: International Agency for Research on Cancer WHO Press. xiv, 630 pages.
10. (W.H.O), I.A.R.C. *GLOBOCAN 2012: Estimated Cancer Incidence, Mortality and Prevalence Worldwide in 2012*. 2012; Available from: <http://globocan.iarc.fr/Pages/Map.aspx#>.
11. Geisler, J., et al., *Malignant melanoma--diagnosis, treatment and follow-up in Norway*. Tidsskr Nor Laegeforen, 2013. **133**(20): p. 2154-9.
12. Kauffmann, R.M. and S.L. Chen, *Workup and staging of malignant melanoma*. Surg Clin North Am, 2014. **94**(5): p. 963-72, vii.
13. Hodis, E., et al., *A landscape of driver mutations in melanoma*. Cell, 2012. **150**(2): p. 251-63.
14. Rubinstein, J.C., et al., *Incidence of the V600K mutation among melanoma patients with BRAF mutations, and potential therapeutic response to the specific BRAF inhibitor PLX4032*. J Transl Med, 2010. **8**: p. 67.
15. (NCBI), N.C.f.B.I. *BRAF B-Raf proto-oncogene, serine/threonine kinase [Homo sapiens (Human)]*. 08.11.2015 10.11.2015; Available from: <http://www.ncbi.nlm.nih.gov/gene?Db=gene&Cmd=ShowDetailView&TermToSearch=673>.
16. McArthur, G.A., et al., *Safety and efficacy of vemurafenib in BRAF(V600E) and BRAF(V600K) mutation-positive melanoma (BRIM-3): extended follow-up of a phase 3, randomised, open-label study*. Lancet Oncol, 2014. **15**(3): p. 323-32.
17. Balch, C.M., et al., *Final version of 2009 AJCC melanoma staging and classification*. Journal of clinical oncology : official journal of the American Society of Clinical Oncology, 2009. **27**(36): p. 6199-206.
18. Corrie, P.G., *Cytotoxic chemotherapy: clinical aspects*. MEDICINE (Elsevier), 2007. **37**(1): p. 24-28.
19. Habermalz, H.J. and J.J. Fischer, *Radiation therapy of malignant melanoma: experience with high individual treatment doses*. Cancer, 1976. **38**(6): p. 2258-62.
20. Renato G. Panizzon, J.S.C., *Radiation Therapy of Melanomas*, in *Radiation treatment and radiation reactions in dermatology*. 2004, Springer Berlin Heidelberg: New York, NY. p. 135-141.

21. Bollag, G., et al., *Vemurafenib: the first drug approved for BRAF-mutant cancer*. Nat Rev Drug Discov, 2012. **11**(11): p. 873-86.
22. Sala, E., et al., *BRAF silencing by short hairpin RNA or chemical blockade by PLX4032 leads to different responses in melanoma and thyroid carcinoma cells*. Molecular cancer research : MCR, 2008. **6**(5): p. 751-9.
23. Das Thakur, M., et al., *Modelling vemurafenib resistance in melanoma reveals a strategy to forestall drug resistance*. Nature, 2013. **494**(7436): p. 251-5.
24. Pardoll, D.M., *The blockade of immune checkpoints in cancer immunotherapy*. Nat Rev Cancer, 2012. **12**(4): p. 252-64.
25. Hamid, O., et al., *Safety and tumor responses with lambrolizumab (anti-PD-1) in melanoma*. The New England journal of medicine, 2013. **369**(2): p. 134-44.
26. Ribas, A., *Tumor immunotherapy directed at PD-1*. The New England journal of medicine, 2012. **366**(26): p. 2517-9.
27. Lisa M. DeAngelis, M.a.J.B.P., MD, *Pathophysiology of the Metastatic Process*, in *Holland-Frei Cancer Medicine 6th edition*, M. Editors: Donald W Kufe, Raphael E Pollock, MD, PhD, Ralph R Weichselbaum, MD, Robert C Bast, Jr, MD, Ted S Gansler, MD, MBA, James F Holland, MD, ScD (hc), and Emil Frei, III, MD., Editor. 2003.
28. Pecorino, L., *Molecular biology of cancer : mechanisms, targets, and therapeutics*. 2nd ed. 2008, Oxford ; New York: Oxford University Press. xviii, 316 p.
29. Kalluri, R. and R.A. Weinberg, *The basics of epithelial-mesenchymal transition*. J Clin Invest, 2009. **119**(6): p. 1420-8.
30. Eichler, A.F., et al., *The biology of brain metastases-translation to new therapies*. Nature reviews Clinical oncology, 2011. **8**(6): p. 344-56.
31. Bollig-Fischer, A., et al., *The molecular genomics of metastatic brain tumours*. OA Mol Oncol, 2013. **1**(1).
32. Nguyen, T. and L.M. Deangelis, *Treatment of brain metastases*. The journal of supportive oncology, 2004. **2**(5): p. 405-10; discussion 411-6.
33. Thorsen, F., et al., *Multimodal imaging enables early detection and characterization of changes in tumor permeability of brain metastases*. J Control Release, 2013. **172**(3): p. 812-22.
34. Patil, C.G., et al., *Whole brain radiation therapy (WBRT) alone versus WBRT and radiosurgery for the treatment of brain metastases*. Cochrane Database Syst Rev, 2012. **9**: p. CD006121.
35. Lwu, S., et al., *Stereotactic radiosurgery for the treatment of melanoma and renal cell carcinoma brain metastases*. Oncology reports, 2013. **29**(2): p. 407-12.
36. Ballabh, P., A. Braun, and M. Nedergaard, *The blood-brain barrier: an overview: structure, regulation, and clinical implications*. Neurobiology of disease, 2004. **16**(1): p. 1-13.
37. Abbott, N.J., L. Ronnback, and E. Hansson, *Astrocyte-endothelial interactions at the blood-brain barrier*. Nat Rev Neurosci, 2006. **7**(1): p. 41-53.
38. Hawkins, B.T. and T.P. Davis, *The blood-brain barrier/neurovascular unit in health and disease*. Pharmacol Rev, 2005. **57**(2): p. 173-85.
39. Pardridge, W.M., *Drug transport across the blood-brain barrier*. J Cereb Blood Flow Metab, 2012. **32**(11): p. 1959-72.
40. Pardridge, W.M., *Blood-brain barrier delivery*. Drug Discov Today, 2007. **12**(1-2): p. 54-61.
41. Connell, J.J., et al., *Selective permeabilization of the blood-brain barrier at sites of metastasis*. Journal of the National Cancer Institute, 2013. **105**(21): p. 1634-43.
42. Quinn, M., et al., *Bile acids permeabilize the blood brain barrier after bile duct ligation in rats via Rac1-dependent mechanisms*. Digestive and liver disease : official journal of the Italian Society of Gastroenterology and the Italian Association for the Study of the Liver, 2014. **46**(6): p. 527-34.
43. Raposo, C., et al., *Acute blood-brain barrier permeabilization in rats after systemic *Phoneutria nigriventer* venom*. Brain Res, 2007. **1149**: p. 18-29.

44. Health, U.S.N.I.o. [cited 2016; Available from: <https://clinicaltrials.gov/ct2/show/NCT02343991>].
45. Hosseinkhah, N., D.E. Goertz, and K. Hynynen, *Microbubbles and blood-brain barrier opening: a numerical study on acoustic emissions and wall stress predictions*. IEEE Trans Biomed Eng, 2015. **62**(5): p. 1293-304.
46. Kahn, T. and H. Busse, *Interventional magnetic resonance imaging*. Medical radiology, diagnostic imaging,. 2012, Heidelberg: Springer. xvii, 496 p.
47. Escoffre, A.B.a.J.M., *Targeted drug delivery with ultrasound and microbubbles: Mechanisms, applications and progress to clinics*. IEEE Newsletter, 2013.
48. Kullervo Hynynen, A.B., Yuexi Huang, William Querbes, & Dinah Sah, *Gene Therapy for Huntington's Disease: The future of focuse ultrasound*, in *Acoustical Society of America; Lay Language Papers*. 2013, Acoustical Society of America.
49. Bellavance, M.A., M. Blanchette, and D. Fortin, *Recent advances in blood-brain barrier disruption as a CNS delivery strategy*. Aaps Journal, 2008. **10**(1): p. 166-177.
50. Dehouck, B., et al., *A new function for the LDL receptor: transcytosis of LDL across the blood-brain barrier*. The Journal of cell biology, 1997. **138**(4): p. 877-89.
51. Sarkar, G., et al., *Peptide carrier-mediated non-covalent delivery of unmodified cisplatin, methotrexate and other agents via intravenous route to the brain*. PLoS One, 2014. **9**(5): p. e97655.
52. Sarkar, G., et al., *A carrier for non-covalent delivery of functional beta-galactosidase and antibodies against amyloid plaques and IgM to the brain*. PLoS One, 2011. **6**(12): p. e28881.
53. Daphu, I., et al., *In vivo animal models for studying brain metastasis: value and limitations*. Clinical & Experimental Metastasis, 2013. **30**(5): p. 695-710.
54. Wang, J., et al., *A novel brain metastases model developed in immunodeficient rats closely mimics the growth of metastatic brain tumours in patients*. Neuropathol Appl Neurobiol, 2011. **37**(2): p. 189-205.
55. Morton, C.L. and P.J. Houghton, *Establishment of human tumor xenografts in immunodeficient mice*. Nat Protoc, 2007. **2**(2): p. 247-50.
56. Ishikawa-Ankerhold, H.C., R. Ankerhold, and G.P.C. Drummen, *Advanced fluorescence microscopy techniques--FRAP, FLIP, FLAP, FRET and FLIM*. Molecules (Basel, Switzerland), 2012. **17**(4): p. 4047-132.
57. Shimomura, O., F.H. Johnson, and Y. Saiga, *Extraction, Purification and Properties of Aequorin, a Bioluminescent Protein from Luminous Hydromedusan, Aequorea*. Journal of Cellular and Comparative Physiology, 1962. **59**(3): p. 223-&.
58. Shimomura, O., *Structure of the Chromophore of Aequorea Green Fluorescent Protein*. Febs Letters, 1979. **104**(2): p. 220-222.
59. UT Astrophysics Lectures [Physics course supplementary material] [cited 2016; Available from: <http://csep10.phys.utk.edu/astr162/lect/light/bohrframe/excitation.html>].
60. Bozzola, J.J. and L.D. Russell, *Electron microscopy : principles and techniques for biologists*. 2nd ed. 1999, Sudbury, Mass.: Jones and Bartlett. xxiii, 670 p.
61. Ganga, H. *ELECTRONMICROSCOPY*. [cited 2015 14.12.2015]; Available from: <http://www.slideshare.net/gangahuvin/electron-microscopy-16995175>.
62. Puddephat, M. *The Principles of Magnetic Resonance Imaging*. [Webpage / Medical Imaging cloud storage site] [cited 2015; Available from: <http://www.voxelcube.com/articles/1/the-principles-of-magnetic-resonance-imaging>].
63. Purcell, E.M., *Research in Nuclear Magnetism*. Science (New York, N Y ), 1953. **118**(3068): p. 431-6.
64. I. I. Rabi, J.R.Z., S. Millman, P. Kush, *A New Method of Measuring Nuclear Magnetic Moment\**. Physical Review, 1938. **53**(4): p. 318-327.
65. Gunnar Myhr, K.N., Atle Bjørnerud, Elin Galtung Lihuag, *Fokus på MRI og bruk av kontrastmidler*. 4th ed. 2002: Amersham plc. 145.
66. Currie, S., et al., *Understanding MRI: basic MR physics for physicians*. Postgrad Med J, 2013. **89**(1050): p. 209-23.

67. Lauterbur, P.C. and P.C. Lauterbur, *Image formation by induced local interactions. Examples employing nuclear magnetic resonance*. 1973. Clinical orthopaedics and related research, 1989(244): p. 3-6.
68. Werner, E.J., et al., *High-relaxivity MRI contrast agents: where coordination chemistry meets medical imaging*. Angewandte Chemie (International ed in English), 2008. **47**(45): p. 8568-80.
69. Tofts, P., *Quantitative MRI of the brain : measuring changes caused by disease*. 2003, Chichester, West Sussex ; Hoboken, NJ: Wiley. xvi, 633 p.
70. Tofts, P.S., et al., *Estimating kinetic parameters from dynamic contrast-enhanced T(1)-weighted MRI of a diffusable tracer: standardized quantities and symbols*. J Magn Reson Imaging, 1999. **10**(3): p. 223-32.
71. Close, D.M., et al., *Autonomous bioluminescent expression of the bacterial luciferase gene cassette (lux) in a mammalian cell line*. PLoS One, 2010. **5**(8): p. e12441.
72. Sato, A., B. Klaunberg, and R. Tolwani, *In vivo bioluminescence imaging*. Comp Med, 2004. **54**(6): p. 631-4.
73. Di Rocco, G., et al., *Analysis of biodistribution and engraftment into the liver of genetically modified mesenchymal stromal cells derived from adipose tissue*. Cell Transplant, 2012. **21**(9): p. 1997-2008.
74. Franke-Fayard, B., A.P. Waters, and C.J. Janse, *Real-time in vivo imaging of transgenic bioluminescent blood stages of rodent malaria parasites in mice*. Nat Protoc, 2006. **1**(1): p. 476-85.
75. Otsu, N., *Threshold Selection Method from Gray-Level Histograms*. IEEE Transactions on Systems Man and Cybernetics, 1979. **9**(1): p. 62-66.
76. Yushkevich, P.A., et al., *User-guided 3D active contour segmentation of anatomical structures: significantly improved efficiency and reliability*. Neuroimage, 2006. **31**(3): p. 1116-28.
77. Sarkar, G., G.L. Curran, and R.B. Jenkins, *Peptide-mediated delivery of active agents across the blood-brain barrier*. 2013, Google Patents.
78. Meng, Y., et al., *Effective intravenous therapy for neurodegenerative disease with a therapeutic enzyme and a peptide that mediates delivery to the brain*. Mol Ther, 2014. **22**(3): p. 547-53.
79. Aryal, M., et al., *Ultrasound-mediated blood-brain barrier disruption for targeted drug delivery in the central nervous system*. Adv Drug Deliv Rev, 2014. **72**: p. 94-109.
80. Chen, C.C., et al., *Targeted drug delivery with focused ultrasound-induced blood-brain barrier opening using acoustically-activated nanodroplets*. J Control Release, 2013. **172**(3): p. 795-804.
81. Yang, H., et al., *RG7204 (PLX4032), a selective BRAFV600E inhibitor, displays potent antitumor activity in preclinical melanoma models*. Cancer Res, 2010. **70**(13): p. 5518-27.
82. Yang, H., et al., *Antitumor activity of BRAF inhibitor vemurafenib in preclinical models of BRAF-mutant colorectal cancer*. Cancer Res, 2012. **72**(3): p. 779-89.
83. Niles, A.L., R.A. Moravec, and T.L. Riss, *Update on in vitro cytotoxicity assays for drug development*. Expert Opin Drug Discov, 2008. **3**(6): p. 655-69.
84. Szczepanski, C., et al., *Identification of a novel lytic peptide for the treatment of solid tumours*. Genes Cancer, 2014. **5**(5-6): p. 186-200.
85. Gobinda Sarkar, G.C., Anne Christiansen, Rizwana Islam, Robert Jenkins, *EVIDENCE THE TRANSPORTER PEPTIDE K16ApoE, TRANSIENTLY OPENS THE BLOOD BRAIN BARRIER TO ALLOW PASSAGE OF MOLECULES TO THE BRIAN*. Neuro Oncol, 2015. **17**(suppl. 5).
86. Bhatnagar, B., et al., *Chemotherapy dose reduction due to chemotherapy induced peripheral neuropathy in breast cancer patients receiving chemotherapy in the neoadjuvant or adjuvant settings: a single-center experience*. Springerplus, 2014. **3**: p. 366.
87. Wildiers, H., *Mastering chemotherapy dose reduction in elderly cancer patients*. Eur J Cancer, 2007. **43**(15): p. 2235-41.

